DEPARTMENT OF PHYSICS

TECHNICAL UNIVERSITY MUNICH

Master of Science (M.Sc.)

Pacific Ocean Neutrino Experiment: Optical Case Studies for the Multi-PMT Module

Author:	Christopher Fink
Professor:	Prof. Elisa Resconi
Supervisor:	Christian Spannfellner
Submission Date:	February 28, 2022

ABSTRACT

Multi-messenger astronomy aims to combine the results from observations of cosmic rays, γ-rays, neutrinos, and recently gravitational waves to gain insight into astrophysical phenomena and mechanisms, some of which accelerate particles to the highest energies ever observed. Significant advancements have been made in the field of neutrino astronomy with the IceCube neutrino observatory in recent years. More and larger installations are however necessary for deeper neutrino observations in the future. Therefore new sites for neutrino telescopes are currently being explored or under construction.

This thesis will present the result of an optical simulation, studying various Photomultiplier Tube reflector cones distributed in an optical module suited for the deep-sea neutrino telescope Pacific Ocean Neutrino Experiment (P-ONE). In this course, the novel approach of using a transparent material is compared to the established solution of a solid metallic reflector used in the optical modules of the KM3NeT detector. Furthermore, we present a first feasibility study to produce a transparent reflector, called a *gel pad*. The gel pad consists of a cured optical gel with a refractive index similar to glass to decrease reflection losses between the pressure vessel and the PMT. It uses total internal reflection on the air-gel boundary to redirect photons to the PMT, which otherwise would have missed it. The focus of this study is the investigation of different optical gels and different techniques to integrate the gel pad into an optical module.

The third chapter of this thesis will cover a two-axis rotation stage developed for precise scans of the photocathode of PMTs in a controlled calibration station. The thesis will close with a chapter on the LiDAR; an instrument developed for the STRAW-b experiment to measure the attenuation and backscattering length of the seawater at the Cascadia Basin site. This chapter will present an algorithm to remotely and automatically adjust the direction of the laser relative to the field of view of the detection unit. Additionally, it will conclude with a comparison of the first measured signals to the simulation.

CONTENTS

I PHYSICAL INTRODUCTION 1
1 INTRODUCTION TO ASTROPARTICLE PHYSICS 3
1.1 Cosmic Rays . . . 3
1.2 Gamma Rays . . . 7
1.3 Neutrinos . . . 8
2 LARGE VOLUME NEUTRINO DETECTORS 9
2.1 Detection Principles . . . 9
2.1.1 Neutrino Interactions . . . 10
2.1.2 The Cherenkov Effect . . . 10
2.1.3 Absorption- and Scattering Length . . . 11
2.1.4 Neutrino Signatures . . . 12
2.1.5 Background . . . 14
2.2 Current and Future Detectors . . . 15
2.2.1 IceCube . . . 16
2.2.2 KM3NeT . . . 16
2.2.3 Baikal GVD . . . 17
2.2.4 P-ONE . . . 18
II THE OPTICAL MODULE OF P-ONE: GEL PADS 19
3 SIMULATION IN GEANT4 21
3.1 General geometry . . . 21
3.1.1 Glass sphere . . . 22
3.1.2 PMT . . . 23
3.1.3 The Reflective Component . . . 25
3.1.4 The Multi-PMT Module . . . 27
3.1.5 Physics and Primary Particles . . . 28
3.2 Results . . . 33
3.2.1 Reflector Angle Study of a Single PMT . . . 33
3.2.2 Simulation of the Multi-PMT Module . . . 37
3.3 Conclusion . . . 44
4 PROTOTYPE-PRODUCTION 47
4.1 Gels . . . 47
4.2 Molds . . . 49
4.3 Coatings . . . 52
4.4 Standalone Gel Pads . . . 52
4.4.1 Procedure . . . 53
4.4.2 Conducted Tests and Results . . . 54
4.4.3 Integration into the Module . . . 57
4.5 In-Situ Pouring . . . 60
4.5.1 Procedure . . . 61
4.5.2 Results and Outlook . . . 62

4.6 Long-Term Delamination Test 63
4.7 Conclusion 64
5 CALIBRATION STATION 65
5.1 Components 65
5.2 The Rotation Stage 67
5.3 Simulation of Gel pads in the Calibration Station 68
III THE SECOND PATHFINDER OF P-ONE: THE LIDAR 71
6 LIDAR 73
6.1 Introduction 76
6.2 Laser Direction Scan 77
6.3 Geant4 Simulation 79
6.4 Data 81
6.5 Conclusion 83
7 SUMMARY & OUTLOOK 85
BIBLIOGRAPHY 87

LIST OF FIGURES

Figure 1.1 Combined spectrum of high energy cosmic particles from various experiments. The full spectrum shown in the upper plot and enhanced views off the *knee* (left) and the *ankle* (right) in the lower plot. Details explained in the text. Figure courtesy of F. Henningsen with data from T. Gaisser, R. Engel, E. Resconi [6] and K. Krings. . 5

Figure 2.1 High-energy neutrino signatures as seen with the IceCube detector. Dots represent indivdual DOMs, their size the amount of detected light and the color the time when the light was detected (red early and green late). Figure taken from [25] 12

Figure 2.2 Size comparison of the ARCA and ORCA detectors [45]. 17

Figure 3.1 The refractive indices used in the simulation. Data for borosilicate glass is taken from [52], for water [53] and the optical gel [54] at 589 nm. 22

Figure 3.2 The left figure (a) shows a technical drawing of the PMT and on the right (b) a sectional sketch of the implementation of it is given. 25

Figure 3.3 Image of the PMT with the gel pad inside a glass sphere in the geant4 simulation. 26

Figure 3.4 Preliminary render of the optical module which we used fo modeling in geant4. Courtesy of L. Papp and C. Spannfellner. 28

Figure 3.5 Detection efficiency for 2.1×10^9 emitted photons for a spherical emitter with homogeneous emission and non-linear bins in theta. 31

Figure 3.6 The relative statistical uncertainty of the detection efficiency resulting from $\sqrt{N}$ uncertainties for a different number of injected photons assuming a Poissonian distribution when averaging over the azimuth angle. The result was derived from a transparent reflector with an opening angle of $40°$. 34

Figure 3.7 Angular acceptance as a function of the angle of incidence and the opening angle for a solid and a transparent reflector. For a detailed discussion refer to the text. 35

Figure 3.8 Detection efficiency for photons with an angle of incidence of $0°$. Errors indicate statistical 1σ uncertainties. 2.1×10^9 were simulated. 36

Figure 3.9 Mean detection efficiency for a solid and a transparent reflector. Errors indicate statistical uncertainties. 37
Figure 3.10 Detection efficiencies of a single PMT with a transparent reflector and an opening angle of 40°. (a) shows the result for the upward facing PMT which is used as a baseline for the rotated response, (b) the difference between the rotation of a upwards facing PMT and a simulated rotated PMT, (c) shows the result from a rotation of a upwards facing PMT and (d) shows the result of the simulation of a rotated PMT. 39
Figure 3.11 The standard deviation of the minimum number of required photons averaged over all directions. 40
Figure 3.12 The required minimum number of photons, which are needed for the optical module to have at least two PMTs detecting one or more photons with a probability of 95 %. (a) shows the result for the calculated angular acceptances, (b) the relative error calculated from this configuration, and (c) and (d) the result with $\pm 1\sigma$ uncertainties. 41
Figure 3.13 The ratio of the mean minimum number of photons. Baseline for the transparent reflector is 40° and for the solid reflector 50°. Errors are derived from the $\pm 1\sigma$ uncertainties of the angular acceptances. 42
Figure 3.14 The minimum number of photons for different opening angles averaged over the azimuth angle. The y-axis shows the cosine of the zenith angle. 43
Figure 3.15 The minimum number of photons for different opening angles averaged over the zenith angle. Results are discussed in the text. 44
Figure 4.1 Images of the manufactured first version of the molds. . 50
Figure 4.2 Illustration of the working principle and images of the parts of the second version of the mold 51
Figure 4.3 Sectional view of the mold assembled with the PMT and the holding frame in SolidWorks. The mold is colored light grey the mold, the 3d printed spacer in grey, and the holding frame in dark grey. The PMT is colored orange. The necessary O-rings and fittings are not depicted. 52
Figure 4.4 Images of the production of the reference gel pad. 54
Figure 4.5 Images of the separation of different gel pads with different treatments. Refer to the text for additional information. 55
Figure 4.6 Images of gel pads produced with the SilGel 612 and the Elastosil RT 601 as a coating. 57

Figure 4.7 Gel pads in a glass sphere with a PMT inserted. No coatings were applied on the *glass sphere - gel pad* and *gel pad - PMT* interfaces. On the cone side facing towards the camera the total internal reflection can be seen (brownish/orange color due to reflection of photons from the photocathode) 58
Figure 4.8 Images of assembled gel pads using the 'blob' technique and optical grease as thin layered coating. 59
Figure 4.9 Images of assembled gel pads using SilGel 612 as a coating. 60
Figure 4.10 Sketch of the procedure of the in situ pouring. The gel is drawn into the assembled mold and exits through an outlet into a reservoir in an overflow container. This container is connected to an air pump generating the vacuum. 61
Figure 4.11 Image of a gel pad produced with the in-situ pouring. A large air bubble resulting from a leaking joint in an O-ring is visible on the left side. 62
Figure 4.12 Sectional sketch (left) and result after six month (right) of the long-term delamination test 63
Figure 5.1 Sketch of the structure of the calibration station. The individual components are explained in the text. Courtesy of L. Winter 66
Figure 5.2 Drawing of the rotation stage in SolidWorks. A detailed description of the individual components is provided in the text. 68
Figure 5.3 Relative detection efficiency from a simulated PMT with a gel pad with an opening angle of 50° and a bare PMT without a reflective component. 5×10^8 photons were simulated. 69
Figure 5.4 Result from a simulated PMT with a gel pad with 50°. With the photocathode as the sensitive volume and the glass housing as the sensitive area. 5×10^8 photons were simulated. Details are provided in the text. 70
Figure 5.5 Sketch depicting the process causing the drop when simulating with the photocathode as the sensitive volume. 70
Figure 6.1 (a) Sketch of the STRAW-b experiment, (b) - (d) images of the deployment of STRAW-b. 75
Figure 6.2 Images of an assembled lidars in the 13 " glass hemisphere. 77
Figure 6.3 Plots of the scan of lidar1 and lidar2. The angular coordinate is the azimuth and the radial coordinate is the inclination. The differences in the color scale are important to note, suggesting a significant difference in the light output of the two lasers although they are operating with the same settings. 78

Figure 6.4 Result from the Monte Carlo simulation for the LiDAR , assuming an attenuation length of 26 m and a backscattering length of 90 m[70]. Errors result $\sqrt{N}$ uncertainties assuming a Poissonian distribution. 80
Figure 6.5 Result from the geant4 simulation with a reduced scattering length of 20 m. Bin width is 5 ns. Errors result $\sqrt{N}$ uncertainties assuming a poissonian distribution. . . 81
Figure 6.6 Result of measurements from both LiDARs. (a) shows the result when the lasers are both in good alignment with the FoV, (b) shows in comparison the result when they are not well aligned, and (c) shows the result of an average of 200 individual measurements. 82

LIST OF TABLES

Table 3.1 Summary of the processes of the primary particle taken into account in this simulation [59]. 29

Table 3.2 Summary of important results of the study of a single PMT. 45

Table 3.3 Summary of important results of the study of a multi-PMT module 45

Table 4.1 Results from the trials with different surface coatings. Result denotes how easy the separation of the gel pad from the mold was relative to the reference gel pad with no treatment and a mixing ratio of 1.5:1 or if any special occurrences happened. 55

Table 4.2 Results from the second round of trials with different optical gels and coatings. Result denotes how easy the separation of the gel pad from the mold was relative to the reference gel pad with no treatment and a mixing ratio of 1.5:1. 57

Part I

PHYSICAL INTRODUCTION

The first part will give an introduction to astroparticle physics and introduce the concept of large scale neutrino detectors followed by examples of current and envisioned neutrino telescopes.

1 INTRODUCTION TO ASTROPARTICLE PHYSICS

Astroparticle physics is an interdisciplinary field of particle physics, astrophysics, and cosmology. It attempts to reveal the nature of cosmic objects and the structure of matter in the universe by studying extraterrestrial particles. The particles are composed of high-energy electromagnetic radiation (γ-rays), cosmic rays, and neutrinos. Thanks to recent advancements, gravitational waves can be added to the collection of messengers [1]. The origin of the field dates back to the discovery of cosmic radiation by Victor Hess with a balloon experiment in 1912 [2]. Today, cosmic rays provide the particles with the highest detected energy of up to 10^{20} eV [3] many orders of magnitude higher than any man-made accelerator can hope to achieve. A multitude of discoveries in the last century in particle physics were performed using cosmic rays. They were the only source of high energetic particles for decades, like the positron and some of the lightest hadrons [4].
In the present day, the major scientific interest extended to the astrophysical information of the particles which revolves around the origin of the particles and the processes accelerating particles to such extreme energies.
However, directional reconstruction proves to be a difficult task with cosmic particles due to their inherent charge, which causes the particles to be subject to deflections through magnetic fields (galactic and extragalactic) on their way to earth.
Combining the information of cosmic rays with the knowledge of additional messengers like γ-rays, neutrinos, and gravitational waves has the potential to provide new insights. This approach is called *Multi-Messenger astronomy*. The following sections introduce the different messengers used for Multi-Messenger astronomy observations starting with the one that triggered this field of physics, the cosmic rays.

1.1 COSMIC RAYS

The primary cosmic rays are charged nuclei, of which protons are the dominant species with ($\approx 85\,\%$), followed by alpha particles ($\approx 12\,\%$). The elements with charge $Z \geqslant 3$ are represented in the remaining $3\,\%$[5]. They hit the earth's upper atmosphere with a rate of about 1000 particles per square meter per second isotropically (due to the deflection in magnetic fields) [6]. This deflection is caused by a Lorentz force F_L applied by the external magnetic fields B, which has the general form of

$$F_L = \frac{Ze}{c}\vec{v} \times \vec{B} \tag{1.1.1}$$

Whereby Ze describes the particle's charge and c is the speed of light. This force causes the particle to spiral along the direction of the magnetic field lines [4]. The radius of this motion is defined by the Larmor radius, r_L, approximated as:

$$r_L \approx \frac{E}{ZeB} \tag{1.1.2}$$

When entering the Earth's atmosphere, the density of ambient particles increases. Thus, the cosmic ray will eventually collide with nucleons of the atmosphere's particles (which mainly consist of nitrogen and oxygen). This interaction initializes a cascade of secondary particles, which in return produce more particles. A so-called *air shower* evolves. The basic reactions possible for a cosmic ray proton are part of the following[4, p.8]:

$$p + N \longrightarrow \pi^{\pm}, \pi^0, K^{\pm}, K^0, p, n, ... \tag{1.1.3}$$

Many of the secondary particles are generally not stable and decay into other particles. The neutral π^0 decays via the electromagnetic force into two highly energetic photons, which start an electromagnetic shower, producing further photons, electrons, and positrons. The charged pions and kaons eventually decay, producing relativistic muons and muon-neutrinos via the weak force. The muons can reach the Earth's surface and are mainly responsible for the muon flux observed on Earth [4].

Cosmic rays can be measured with two types of experiments. *Direct* measurements are performed with space experiments located on satellites that make use of high-altitude balloons, like the AMS, (ISS-)CREAM or BESS experiments [4, p.8]. The energy range of CRs measured with direct detection is limited to 10^{15} eV, as the particle flux quickly declines to less than ten events per m^2 per year [4, p.97]. Due to the limited payload capabilities of space missions, these experiments are limited in their spatial extension and target mass. The highest energetic cosmic rays are measured using *indirect* ground-based detectors. In contrast to space experiments, they have sensitive areas orders of magnitude larger. They measure the secondary particles of extensive air showers with a combination of large arrays of surface detectors (*SD array*) and the ultraviolet fluorescence detectors (*FD system*) [7] [8, p.168]. The detectors of the SD arrays consist of a water tank equipped with Photomultiplier Tubes (PMTs) to detect Cherenkov light emitted by the secondary particles. The FD system detects the fluorescence light emitted by the de-excitation of nitrogen molecules in the atmosphere, which had been excited by low-energy electrons of the shower. The Pierre-Auger-Observatory is the largest of the ground-based telescopes [7].

Due to the different types of detectors, the observed spectrum of cosmic rays covers many orders of energies, from 10^9 eV to 10^{20} EeV. Remarkably, the spectrum can be described with a power law:

$$\frac{d\Phi}{dE} = A \cdot E^{-\alpha} \tag{1.1.4}$$

Power-law spectra are commonly observed for non-thermal processes [4, p. 9] α denotes the spectral index of the function. IN a double-logarithmic plot, the spectrum is depicted in a line with the slope α. Many of the observed power-law spectra are very steep, with spectral indices between -2 and -4. To flatten the spectrum and to make out slight deviations from a given spectral index, the spectrum is frequently multiplied with a weighting factor of the form of E^{β}. For the majority of the spectrum of cosmic rays, the spectral index is ≈ -2.7 (up to 10^{15} eV). Above this energy range, the spectral index transitions to a stepper value of ≈ -3.1. This transition is commonly known as the *knee*. It is considered that this change in the spectral index marks a transition between different classes of galactic accelerators [4, p. 10] or indicates the approaching end of the spectrum of galactic accelerators [6, p.12]. The spectral index stays constant until an energy of 10^{19} eV, where the spectrum flattens to ≈ -2.6. The second transition is known as the *ankle*. This transition is often associated with the emergence of particles of extragalactic origin [6, p.12]. However, acceleration processes and origins of high-energy particles are still not fully understood and are the subject of current scientific research.

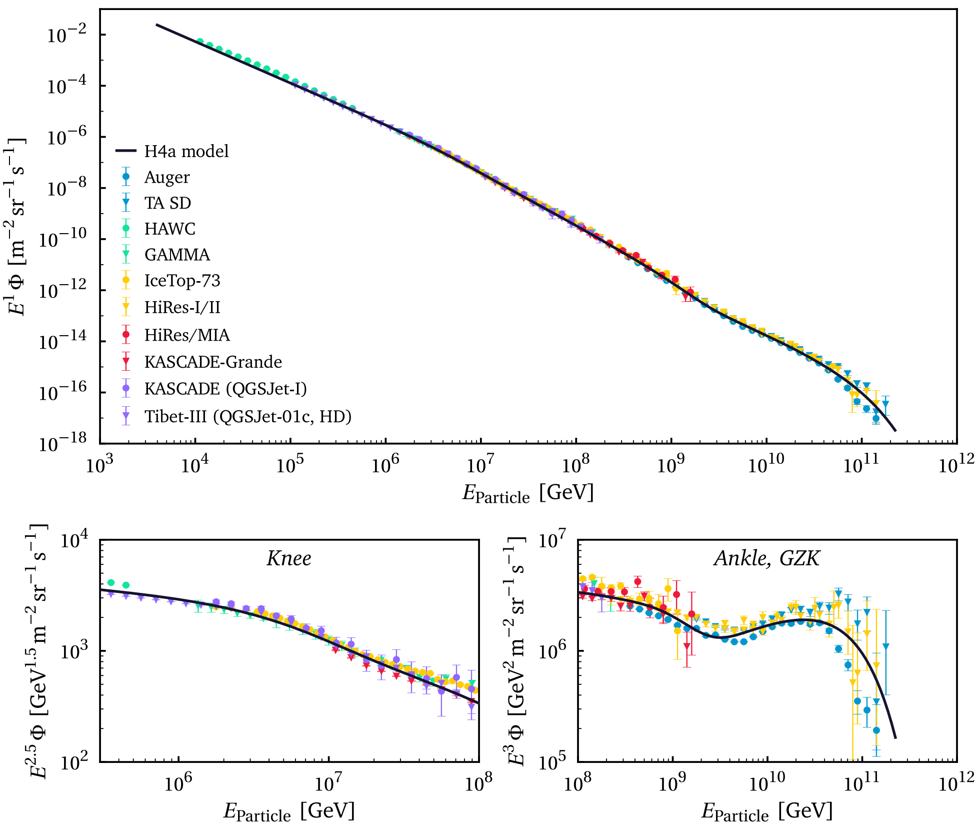

Figure 1.1: Combined spectrum of high energy cosmic particles from various experiments. The full spectrum shown in the upper plot and enhanced views off the *knee* (left) and the *ankle* (right) in the lower plot. Details explained in the text. Figure courtesy of F. Henningsen with data from T. Gaisser, R. Engel, E. Resconi [6] and K. Krings.

Finally, the spectrum cuts of at around 10^{20} eV. This is commonly referred to the *GZK-cutoff* after K. Greisen, V. Kuzmin, and G. Zatsepin, who predicted it in 1966. It is the result of protons interacting with the cosmic microwave background to produce the first Δ^+ resonance, which decays in two channels [4, p. 219].

$$p + \gamma_{\mathrm{CMB}} \rightarrow \Delta^+ \rightarrow \begin{cases} p + \pi^0 \\ n + \pi^+ \end{cases} \tag{1.1.5}$$

The pion and neutrino decay channels produce protons with energies below the cut-off threshold and additionally, γ-rays and neutrinos are produced. Figure 1.1 shows the combined high energy cosmic ray spectrum of multiple experiments.

GALACTIC ACCELERATORS Although high energetic CRs are detected, it is still an open question of how the acceleration mechanisms of these particles work. However, only a few known types of astrophysical objects can accelerate cosmic particles. The bulk of the cosmic particles up to the knee is expected to originate from the galaxy. Today, the shock acceleration in supernova remnants (SNRs), the result of violent explosions at the end of the evolution of stars, is considered a dominant mechanism for cosmic acceleration rays. The CRs diffuse back and forth across the supernova shock front in this process. At each crossing, the energy of the magnetized plasma is transferred to the charged particle; thus increasing its energy. The transfer happens several times until the particle escapes the shock front. This process results in a spectrum with a spectral index of -2. Subsequent propagations and further energy losses can alter the spectrum to the on-earth observed spectral index of -2.7. The observed energy density of cosmic rays of galactic origin could be supplied if $\approx 10\,\%$ of the energy from supernovae could be harnessed. [9] [8, p.582-585].
Additional candidates are pulsar wind nebulae (PWN). The powerful outflow of charged particles, driven by the rotation and magnetic field of the pulsar. The magnetic fields are the strongest observed in the universe [8, p.596].

EXTRAGALACTIC ACCELERATORS The current assumption for CRs with extremely large energies (UHECRs) is that they originate from outside of our galaxy. When the energy of the particle exceeds 10^{18} eV, the above mentioned Larmor radius equals approximately the diameter of the galactic disk (300 pc) for a magnetic field strength of $B \approx 3\,\mu\mathrm{G}$ as it is measured for our galaxy [6]. Meaning particles with such high energies would correlate with the source's position should they originate from within our galaxy. Thus extragalactic sources need to be considered [4, p.203].

The first candidates are active galactic nuclei (AGN). Supermassive black holes in the order of 10^6 - 10^{10} solar masses form the center of galaxies. In about $1\,\%$ of all cases, the black hole is active, i. e. strong emission can be observed. In this case, it is called an AGN. They are powered by the accretion of matter falling into the supermassive black holes. In about $10\,\%$ the matter turns into collimated relativistic particle jets ejected opposite to each other

and perpendicular to the accretion disk [8]. If the jets point towards the earth, the AGN is called *blazar* [10]. Despite the considerable interest in AGN over many decades and observations in many different wavebands, the underlying principles of the relativistic jets and the emission characteristics necessary for understanding the extreme particle accelerators for the highest energies are still not entirely understood [8, 11].
Additional candidates are gamma ray bursts (GRB), producing suitable environments to accelerate CRs to the highest energies. GRBs can result from the core collapse of a massive neutron star or black hole, or the merger of a binary system (e. g. two neutron stars) and are the most energetic transient objects in the universe, lasting from a few seconds to sometimes several thousand of seconds. GRBs are widely described by the fireball model [6, 8].

1.2 GAMMA RAYS

Due to the deflection of charged particles in galactic magnetic fields, it is impossible to localize the origins of cosmic rays. In contrast, neutral particles like γ-rays and neutrinos can point directly to their origin. Though the generation processes for γ-rays are similar to Cosmic Rays, it is not fully understood which process is dominant for a source. It is expected that the cosmic sources are the same as for cosmic rays [5].
Current theories divide the production mechanisms into two categories: The first one involves production in *leptonic processes*. Possible production mechanisms in this category are synchrotron radiation, Bremsstrahlung, and Inverse Compton Scattering for higher energies.

The second kind of production mechanism is summarized under *hadronic processes*. In the hadronic model, the accelerated cosmic rays interact with other protons or nuclei, subsequently producing various mesons and baryons (comparable to the result of Equation 1.1.3), including neutral pions. The neutral pions decay into two high energetic photons via

$$\pi^0 \rightarrow \gamma + \gamma \tag{1.2.1}$$

Due to similarities with fixed-target accelerators, this process is often referred to as *astrophysical beam dump* [4]. An additional process is called *photoproduction* in which high-energy CRs interact with low-energy photons similar to the mechanism of the GZK cut-off using ambient photons in the vicinity of astrophysical sources [4].
Similar to the detection of CRs, γ-ray telescopes can be divided into space- and ground-based telescopes. Space telescopes like the Fermi satellite detect γ-rays directly via a combination of a tracker to obtain directional information of the incoming γ-ray and a calorimeter to measure its energy [12]. Over a period of 10 years, the Fermi satellite identified over 5700 different γ-ray sources, published in the 4FGL-DR2 catalog [13].
However, similar to CRs, the flux of high energy γ-rays drops quickly. Satellite detectors can only be used efficiently until an energy of a few hundred

GeV, due to their limited detector area. To measure larger energies up to a few hundred TeV, ground-based telescopes need to be used like Imaging Air Cherenkov Telescopes (IACT). They consist of arrays of large optical mirror telescopes with reflector diameters of up to 23 m [14], which measure Cherenkov light.
γ-rays interact with nuclei in the upper hemisphere producing an extensive air shower. In contrast to cosmic ray-induced air showers, air showers from γ-rays have only the electromagnetic channel available. After an interaction, γ-rays produce an electron-positron pair which yields more γ-rays through Bremsstrahlung, starting the cascade. If the secondary charged particles are faster than the speed of light in air, they emit Cherenkov light, collected by the individual telescopes in an IACT array. From the arrival time and the amount of light, one can reconstruct the direction and energy of the γ-ray. The Cherenkov effect is also of great importance for deep-sea neutrino telescopes. It is highlighted in more detail in Section 2.1.2).

1.3 NEUTRINOS

Neutrinos are electrically neutral leptonic particles predicted in the last century to solve the mystery of the continuous beta decay spectrum. In contrast to all other fundamental particles, neutrino interact solely via the weak interaction with the exchange of Z or W bosons. The weak interaction has the lowest interaction cross sections making interactions with matter very unlikely. As a consequence, neutrinos traverse the universe largely unhindered making them a good candidate for identifying sources. In addition, the observable universe is transparent to almost any energy of neutrinos. In contrast to this, the universe becomes opaque for CRs with energies above $\approx 10^{19}$ eV (GZK-cutoff). The horizon for γ-rays is limited by interaction with ambient matter and CMB. Although the low cross-section is very beneficial for propagation, it poses significant challenges for their detection. Detectors like the IceCube Neutrino Observatory instrument huge volumes, $\mathcal{O}(1\,\text{km}^3)$, to increase the detection probability for neutrinos. In the last two decades, several other collaborations set out to develop large-scale neutrino telescopes, including the P-ONE collaboration for which this work has been conducted. The following chapter will cover the detection principles of large-scale neutrino detectors and give an introduction to existing and planned detectors in more detail.

2 LARGE VOLUME NEUTRINO DETECTORS

As outlined in the previous section, neutrinos interact only weakly and are thus very challenging to detect. To detect high-energy cosmic neutrinos and pinpoint their origin, sensitive volumes in the order of cubic kilometers are required. First ideas for such a large detector date back to proposals by M. Markov [15]. After first conceptual studies to realize the idea, like the DUMAND experiment, several neutrino telescopes have been built, are currently under construction, or in development. In 2013 IceCube detected the first extraterrestrial neutrinos [16] and in 2017, a neutrino which was in coincidence with the γ-ray blazar TXS 0506+056 [17]. The latter event triggered several follow-up observations through different messengers [18]. This chapter will summarize the main physical principles involved in observing high-energy neutrinos and cover existing and potential future neutrino telescopes.

2.1 DETECTION PRINCIPLES

The idea to use a large optically transparent medium instrumented with an optical sensor was proposed in 1960. The optical sensor would detect the Cherenkov light produced by charged particles stemming from e. g. neutrino interactions. This idea developed in two ways: The first idea led to the development of massive, densely instrumented tanks of pure water deep underground to shield off as much background as possible. In this category belong the (Super-) Kamiokande or SNO experiments. These experiments focused on the low-energy atmospheric and solar neutrinos to investigate the stability of the proton and perform precise measurements on the neutrino oscillation [19]. The second path was motivated by finding the origins of cosmic rays. To do this, high-energy neutrinos significantly above the GeV regime are targeted. Combining a tiny interaction cross-section and a small flux of high-energy cosmic neutrinos resulted in the need for even larger sensitive volumes than provided by the low-energy experiments or feasible to build. Therefore, natural sources of a transparent medium, like the deep sea or glacial ice, are instrumented with photosensors encapsulated in a pressure vessel to protect against the hazardous environment present at these sites. Inside the sensitive volume, secondary charged particles produce optical photons due to their high energies detected by the photosensors. From the total light yield and time distribution of the detected Cherenkov photons, one can gain information about the direction and energy of the primary neutrino.

2.1.1 NEUTRINO INTERACTIONS

In the standard model of particle physics, only the weak interaction is allowed for neutrinos. For highly energetic neutrinos (above several GeV), the interaction is dominated by deep inelastic scattering with the quarks of a nucleon N of the ambient medium [20]. This interaction can be carried out either by the neutral Z^0 or the charged $W^{\pm}$ bosons. The interactions involving a Z^0 boson belong to the *neutral current*, whereas interactions involving the charged bosons belong to the *charged current* events. In the most general form, the two currents can be formulated as:

$$\nu_l + N \rightarrow l + X \qquad \text{(CC)} \tag{2.1.1}$$

$$\nu_l + N \rightarrow \nu_l + X \qquad \text{(NC)} \tag{2.1.2}$$

N denotes the nucleus, while $l = e, \mu, \tau$ covers the possible neutrino flavors, and X one or more hadronic particles, producing a subsequent hadronic shower. In NC events, the scattered neutrino keeps most of its energy while the rest is deposited in the induced hadronic shower. In CC events, most of the neutrino energy is transferred to the produced lepton [6]. The produced hadronic particles can carry away a significant portion of the neutrino's energy, thus opening the field for various interactions in which photons can be created, resulting in a hadronic cascade. At higher energies, the photons produced from the Cherenkov effect are dominant, which can be utilized by a neutrino detector.

2.1.2 THE CHERENKOV EFFECT

A charged particle traversing a dielectric medium causes local polarisations in the medium. If the particle's speed is below the local phase velocity of light in the medium c_n, the dipoles will annihilate in destructive interference without a radiation output. The phase velocity of light in a dielectric medium with a refractive index n can be defined as

$$c_n = \frac{c_0}{n} \tag{2.1.3}$$

However, if the speed exceeds the speed of light in the medium, i. e. $v > c_n$, the local polarisations do not have time to relax back to equilibrium. Thus the particle leaves back polarized matter, which can no longer annihilate but instead result in the emission of electromagnetic radiation. This effect is called the Cherenkov effect, after the Soviet physicist P.A. Cherenkov who discovered this effect in 1934.
The photons are emitted in a cone with a characteristic opening angle θ relative to the trajectory of the particle defined as

$$\cos(\theta) = \frac{1}{\beta \cdot n} \tag{2.1.4}$$

with $\beta = v/c$ the velocity ratio of the particle. For highly relativistic particles, $\beta \simeq 1$ and $n \simeq 1.36$ are appropriate assumptions for water, resulting in a Cherenkov opening angle of $\theta \simeq 43°$ [4, p.324].

The number of emitted Cherenkov photons N_C per unit wavelength interval $d\lambda$ and per unit distance traveled dx by a charged particle with a charge $q = z \cdot c$ can be analytically approximated by the Franck-Tamm formula [21]:

$$\frac{dN_C}{d\lambda dx} = \frac{2\pi e^2}{hc\lambda^2} \cdot \left(1 - \frac{1}{\beta^2 n(\lambda)^2}\right) \tag{2.1.5}$$

A typical number of emitted Cherenkov photons per meter is in the order of 3×10^4 photons [4]. This formula shows that Cherenkov photons are produced with a wavelength dependency of $1/\lambda^2$. After initial emission, the photons propagate through the medium and are therefore subject to absorption and scattering processes which are wavelength dependent. Due to this, the spectrum of the observable Cherenkov photons is limited to the range of 300 nm to 600 nm which matches well with the quantum efficiency of PMTs with alkali-metal photocathodes [4].

2.1.3 ABSORPTION- AND SCATTERING LENGTH

The emitted Cherenkov photons propagating through the medium are subject to two physical processes which can alter their path: absorption and scattering. During absorption, the electrons bound in an atom of the molecules of the medium absorb the energy, get in an excited state, and subsequently release the energy in the form of thermal energy. Scattering can be further divided into scattering by molecules or particles the size of the wavelength of the photon (*Rayleigh scattering*) and into scattering by particles significantly larger than the wavelength of the photon (*Mie scattering*).

For an initial intensity of light I_0 of an isotropic emitter, the intensity after the light has propagated a distance of r in the medium is defined by the Lambert-Beer-law as

$$I(r) = \frac{I_0}{4\pi r^2} \cdot \exp\left[-\frac{1}{l_{att}} \cdot r\right] \tag{2.1.6}$$

with l_{att} the attenuation length after which the initial intensity dropped to $1/e$. Is is composed of the absorption length l_{abs} and the *effective scattering length* l_{scat}^{eff} and is defined as

$$l_{att} = \left(\frac{1}{l_{abs}} + \frac{1}{l_{scat}^{eff}}\right)^{-1} \tag{2.1.7}$$

The use of the effective scattering length is empirically driven, as it reduces the number of parameters needed to characterize the intensity profile after a distance r. Generally, one needs to consider the *volume scattering function* $\beta(\theta) = \tilde{\beta}(\theta)/l_{scat}$ which relates the scattering length to the normalized scattering angle distribution $\tilde{\beta}(\theta)$. This can be roughly described by the scattering length to the average cosine of the scattering angle distribution $\langle\cos\theta\rangle$. If the scattering is dominated by small angles the effective scattering length can be related to the scattering length by the following relation [22]

$$l_{scat}^{eff} = \frac{l_{scat}}{1 - \langle\cos\theta\rangle} \tag{2.1.8}$$

The scattering and absorption length can vary significantly between different media. In the deep glacial ice, the absorption length is relatively high with values in the order of 100 m while the effective scattering length is significantly smaller [23]. In the deep sea absorption is the dominant factor. The high effective scattering length of water makes water-based neutrino telescopes an excellent candidate for point-source searches as the light produced by high-energy neutrino-induced muons propagate without significant scattering until it is detected (average distances between modules are in the order of 50 m to 100 m and the measured effective scattering length of seawater is in the order of 200 m to 300 m [24]). On the contrary, the energy resolution is worse due to the lower absorption length in seawater absorbing more photons before they are detected.

2.1.4 NEUTRINO SIGNATURES

Depending on the type of interaction, neutrinos of different flavors can be seen with different types of signatures within the sensitive volume. In general, one can distinguish between two basic event topologies: *cascade events*, which are the outcome of all NC interactions and some CC interactions, and *track events*, which is the outcome of a CC involving a muon-neutrino. The third class of event types, called *double bang events* exists. It involves the CC outcome of a tau-neutrino. However, to this date, no detected neutrino has been identified with the last type of event. Figure 2.1 depicts a visualization of all three categories of events.

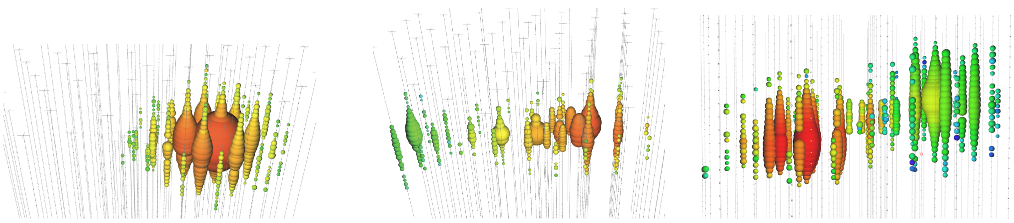

(a) cascade (b) track (c) double bang

Figure 2.1: High-energy neutrino signatures as seen with the IceCube detector. Dots represent indivdual DOMs, their size the amount of detected light and the color the time when the light was detected (red early and green late). Figure taken from [25]

CASCADE-LIKE EVENTS This category can be induced by either CC interactions involving an electron or tau neutrino or by NC interactions of all three neutrino flavors. The CC interaction of an electron neutrino produces a high-energy electron which radiates its energy through bremsstrahlung leading to

an electromagnetic cascade. Due to the high interaction cross-section of the electron that carries most of the energy of the initial neutrino, the extension of the shower is in the order of a few meters, much smaller than the spacing of the optical modules from the detector [4]. Additionally, the remaining nuclei fragment induces a hadronic cascade at the initial interaction vertex (accounting for ~ 20 % of the primary energy at the point of the interaction [6, p.363]). The CC interaction of a ν_τ results in a τ-lepton carrying most of the initial energy. The τ has a large branching ratio to hadrons [6, p.363] meaning that it initiates a second hadronic cascade when decaying. The second cascade is for most energies contained in the initial cascade because it cannot be resolved by the detector.
The NC channel gives the same signature for all different neutrino flavors. A fraction of the energy is always carried away by the outgoing neutrino in this channel. Hence, increasing the error on the reconstructed energy. The remaining energy is transferred to the remaining nucleus, which initiates the hadronic cascade. In all cases, light emission is very local; therefore, the directional reconstruction is very difficult and comes with large uncertainties. On the other hand, most of the emitted light is contained within the detector, allowing a good energy resolution. Figure 2.1a shows a visualisation of a cascade-like event.

TRACK-LIKE EVENTS In the CC interaction of a muon neutrino, a μ is produced which propagates in the medium. In the energy range covered by large-scale neutrino telescopes, the produced muon's track largely coincides with the direction of the primary muon neutrino [4]. While propagating, the muon emits Cherenkov radiation with a characteristic angle (see Section 2.1.2). Thus the information of the elongated track can be used to reconstruct the track, i. e. the direction of the muon. However, the emitted photons are subject to scattering and absorption processes on their path to the optical module. Consequently, good knowledge of the scattering and absorption length of the medium is vital. In IceCube, the angular resolution is below 1° for high energy track-like events [26]. While the directional reconstruction for tracks is very good, the energy resolution can only give a lower limit because only a fraction of the track might be contained in the detector. The central image of Figure 2.1 depicts a visualization of a track-like event.

DOUBLE-BANG EVENTS A special case of events are very high energy τ-neutrinos interacting via the CC channel with the medium. As covered before, the τ produces a second hadronic cascade when decaying, provided that the energy of the τ is sufficient. In that case, it covers a greater distance so that the detector can resolve the two hadronic cascades (the first initiated by the fragmented hadron and the second from the τ decay). This process is expected for energys in the region of $E_\tau \sim$ PeV [6].

2.1.5 BACKGROUND

Different background sources can influence the measurement of the astrophysical neutrinos and shall be introduced in this section. The background sources can be sorted into two categories: related to the neutrino signal or to the ambient medium. Additional hardware-induced noise originating from the inherent dark rate of the PMT or the data acquisition will not be covered in this section.

ATMOSPHERIC NEUTRINOS AND MUONS The main background source is atmospheric neutrinos. Various secondary particles are produced when CRs interact with nuclei in the upper atmosphere. Among them are the pion and kaon mesons which eventually decay into muons and muon-neutrinos. Lower energy muons will also decay before reaching the ground, thus producing electrons and electron-neutrinos via the following interactions:

$$\pi^+ \rightarrow \mu^+ + \nu_\mu \qquad \pi^- \rightarrow \mu^- + \overline{\nu}_\mu \tag{2.1.9}$$

$$\hookrightarrow e^+ + \nu_e + \overline{\nu}_\mu \qquad \hookrightarrow e^- + \overline{\nu}_e + \nu_\mu \tag{2.1.10}$$

From this result, a muon flavor ratio of

$$\nu_e : \nu_\mu : \nu_\tau = 1 : 2 : 0 \tag{2.1.11}$$

was expected, but was not observed which led to the discovery of neutrino oscillations in the Super-Kamiokande [19]. Today the atmospheric neutrino flux can be used to perform measurements on the neutrino mass hierarchy with e. g. the ORCA detector from KM3NeT [27].
The flux of atmospheric neutrinos resulting from pion and muon decays is called *conventional neutrino flux* and has been observed by all major neutrino detectors (e. g. in [28–30]). The results suggest that the observed energy spectrum peaks in the range of GeV and follows a power law for higher energies with a spectral index similar to the one of the initial CR. However, this spectrum softens with increasing energy caused by muons not decaying before reaching the Earth's surface [31]. Additionally, a yet unobserved component resulting from the decay of heavier charmed or bottom mesons is called *promt neutrino flux* which is expected to dominate the atmospheric neutrino spectrum for energies above $\sim$ PeV [32].

The aforementioned high-energy muons pose an additional source of background. When their energy is large enough, they do not decay on their way to the Earth but penetrate its surface. The signal of the penetrating atmospheric muon in a neutrino detector can not be distinguished from a neutrino-induced muon. Additionally, the event rate can be several orders of magnitude higher [33]. A simple rejection mechanism performed by IceCube is to restrict the signal to only upgoing muons, i. e. IceCube uses the earth as a shielding.

K-40 For water-based neutrino detectors, some more background sources not directly related to the neutrino signatures but to the environmental background need to be considered. The first one is the decay of potassium isotopes

(^{40}K) which are dissolved in the seawater. Potassium decays via two channels. In the β-decay channel an electron with an energy of up to 1.3 MeV is produced, which emits Cherenkov radiation. In the electron capture channel, excited Argon is produced, releasing a photon. The photon generates electrons through Compton scattering, which produces Cherenkov radiation as well. Additionally, if the decay occurs in the vicinity of an optical module, multiple modules can detect a Cherenkov photon in a short time frame (local coincidence). When only accounting for local coincidences (time window of 25 ns), this rate is reduced to less than 1 Hz in the KM3NeT modules for adjacent PMTs [34]. The STRAW modules detected a coincidence rate of less than 0.1 Hz [35]. However, apart from the salinity comparable for the Mediterranean Sea and the Pacific Ocean, this rate largely depends on the optical module configuration and effective area, which significantly varies between the STRAW and the KM3NeT modules.

BIOLUMINESCENCE The second significant contribution to the background unique to water is bioluminescence light emitted by living organisms in the deep sea. This light is either produced in flashes or diffuse and the spectrum peaks in the range of 440 nm to 500 nm [36, 37], which superimposes with the peak in the Cherenkov spectrum making disentanglement difficult. The light emission is expected to be caused by either contact forces, i. e. organism colliding with objects, or by shear forces, e. g. caused by turbulences of the sea current behind the optical modules [37]. The bioluminescence has been continuously monitored over two years at the Cascadia Basin Site with STRAW. Substantial variations in the rate were found ranging from ≈10 kHz up to MHz in short time frames with a variational circle corresponding to the 12.5 hours of the tidal circle [35]. Furthermore, no significant seasonal variation was observed in the two years [35]. Two different kinds of specialized instruments, the PMT spectrometer, and the CCD spectrometer, were deployed in the STRAW-b experiment to investigate this background further [38, 39].

2.2 CURRENT AND FUTURE DETECTORS

Neutrino telescopes rely on the principles discussed in the previous sections, which is the instrumentation of large volumes of a transparent medium with light sensors to detect Cherenkov light produced by neutrino interactions. In this approach, the light sensors consist of a pressure vessel housing either a single large photomultiplier tube or multiple smaller ones distributed in the pressure vessel. The modules are connected with strings providing data connection and power. The data is then sent on-shore for storage and analysis.
The amount and distribution of the modules depend on the scientific hypothesis of interest but are also limited by the accessible infrastructure, i. e. available power, data rate, and ultimately on the available funding. Since the DUMAND experiment in the 1970s, several smaller pioneer experiments have been built. To this day, only the IceCube detector has been finished and is taking data.

Additionally, the Baikal GVD and KM3Net detectors are currently in their construction phase, while P-ONE is currently in development. All four will be outlined in the following, starting with IceCube.

2.2.1 ICECUBE

The IceCube neutrino observatory is located 2450 m below the surface at the South Pole Station in Antarctica. It is the successor of the pioneer experiment AMANDA and was fully finished by 2010 with data taking starting from 2005. The instrumented volume encompasses roughly one cubic kilometer with 86 vertical strings of 1 km length. In total, 5160 optical modules called DOMs (Digital Optical Modules) are distributed on the strings. An individual DOM consists of a 13" spherical pressure vessel with a downward-facing 10" photomultiplier tube and the read-out electronics. The modules are 17 m separated on each line, and the inter-string spacing is 125 m. With this configuration, IceCube is sensible for neutrinos in the range of 100 GeV to several PeV [40].
Eight additional more densely equipped strings have been installed in the central region of IceCube, which is called *DeepCore*. It is optimized for energies as low as 10 GeV and aims for the investigation of neutrinos produced from WIMP dark matter annihilations, atmospheric neutrino oscillations, and galactic supernova neutrinos. The detector is complemented with an array of 81 ice tanks at the surface, each equipped with two optical modules, called *IceTop*. IceTop is an independent air shower detector for cosmic rays in the range of 100 TeV to 1 EeV providing IceCube a veto mechanism against atmospheric muons [41].
Over more than a decade, IceCube has contributed to major scientific discoveries, including the first detection of neutrinos of cosmic origin in 2013 [16], the first potential neutrino source [17, 18] and detected the highest energetic neutrino with an energy of at least 1 PeV [42].
Currently, the IceCube Upgrade is a planned extension of the existing detector to extend the energy range down to $\sim$ 10 GeV. Enabling measurements of the tau neutrino appearance and thus neutrino oscillations. It is planned to consist of seven strings with $\sim$ 700 next-generation modules investigating a multi-PMT approach and new calibration devices.

2.2.2 KM3NET

KM3NeT is a neutrino telescope currently under construction at three sites in the Mediterranean Sea, namely, at Toulon in France, Portopalo di Capo Passero (Sicily, Italy), and Pylos in Greece, resulting in a network of several neutrino detectors. The experiment continues the work achieved by their predecessor ANTARES [43] and NEMO [44]. KM3NeT will host two different detectors called ORCA and ARCA, each built for different scientific goals. ARCA (Astroparticle Research with Cosmics in the Abyss) will be used to study the high-energy cosmic neutrino flux and provide complementary data about the origin and energy spectrum of neutrinos. Due to the positioning in the northern hemisphere, ARCA will observe most of the Galaxy, including the Galactic Center. It will feature two detector blocks of 115 mooring lines (called *detection unit*) equipped with optical modules with a length of 700 m and will be deployed at the Italian site in phases. In October 2021, the first phase with eight detection units was successfully deployed [46].

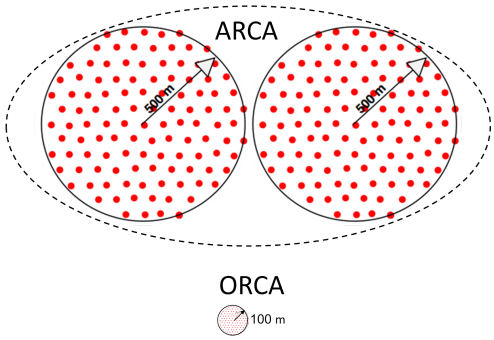

Figure 2.2: Size comparison of the ARCA and ORCA detectors [45].

ORCA (Oscillation Research with Cosmics in the Abyss) will focus on the low-energy fundamental properties of the neutrinos e. g. relative mass ordering of the neutrino masses. Hence, ORCA is optimized for the abundant neutrino flux produced by cosmic rays in the Earth's Atmosphere. Like the ARCA detector, ORCA will feature one detector block comprising 115 detection units. However, the spacing between detection units and between individual optical modules is much smaller to achieve the different scientific goals. The first phase of the deployment at the french site with six vertical lines has been finished [27].

In contrast to the IceCube detector and the GVD, KM3NeT uses multiple smaller PMTs (up to 31) in their optical module instead of a single large downward-facing PMT. Compared to IceCube, some other differences to the medium are evident. The optical modules in the water are subject to movement due to the changing currents of the seawater. Thus additional position calibration is required for water-based detectors. To do this, KM3NeT uses continuous acoustic calibration. Several acoustic transmitters are placed on the seabed at known positions, and each optical module bears an acoustic receiver [47].

2.2.3 BAIKAL GVD

The Baikal Neutrino Telescope was one of the first neutrino detectors to start construction in 1980. It is built in Lake Baikal at a depth of 1.1 km. After several small-sized stages, NT200 started data taking in 1998 with a configuration of 192 modules distributed over eight strings. The stage was completed in 1998 and further upgraded until 2005. Since 2016 the Gigaton Volume Detector (GVD) has been under construction. GVD follows a clustered approach, each of the clusters will contain eight strings with 288 optical modules each.

In 2021, the first phase of the entire telescope, GVD-I, was completed, with eight individual clusters and an effective volume of about 0.5 km^3. Two more stages are planned, resulting in an effective volume of 1.5 km [48].

2.2.4 P-ONE

The Pacific Ocean Neutrino Experiment (P-ONE) is a proposed third water-based neutrino telescope in the northern hemisphere. It will be located at the Cascadia Basin west of Vancouver Island, Canada. The Cascadia Basin is a plane located in the North Pacific Ocean at a depth of around 2.7 km. This site was specifically chosen because it has the unique opportunity of an already existing deep-sea infrastructure in which the detector can be integrated. This infrastructure is hosted by Ocean Networks Canada (ONC), an initiative of the University of Victoria. It includes various instruments to provide scientific data from the ocean environment. P-ONE is planned to be hosted on one of the five nodes of the NEPTUNE (North East Pacific Time-series Underwater Experiments) observatory. Two pathfinder missions have been deployed to perform optical site characterization measurements and investigate deployment strategies. The first pathfinder, STRAW (STRings for Absorption length in Water), was deployed in 2018. It consists of two 120 m long moorings equipped with two kinds of modules. One is hosting light flashers of several different wavelengths in the optical band and the other hosting PMTs to detect the emitted light. The goal was to measure the attenuation length of the seawater. In 2021, analysis results of two years of data have been published [35]. Motivated by the success of STRAW, a second pathfinder mission, STRAW-b, was deployed in 2020. It consists of a single 450 m long mooring line with ten modules, of which six were equipped with specialized instruments. Two LiDARs to verify the attenuation length and perform measurements on the backscattering length (details in 6), two PMT-based and one CCD-based spectrometer to perform in-depth measurements of the bioluminescence background, a muon tracker, and the wavelength shifting optical module (WOM). Additionally, to the scientific goals, STRAW-b was used to investigate a deployment strategy for future P-ONE mooring lines [39].

Part II

THE OPTICAL MODULE OF P-ONE: GEL PADS

The second part focuses on the optical gel pad. A component that couples the PMT to the glass sphere and helps to increase the detection efficiency of the PMT. The first half will focus on the simulation where we compare a transparent reflector (i. e. a gel pad) to a solid reflector. The second half will discuss the first case studies to produce gel pads. In the last section, we will detail an automated calibration station for PMTs, which can be used to compare simulation results of the gel pads with the first measurements.

3 SIMULATION IN GEANT4

Th geant4 software package has been actively developed and is maintained by the international Geant4 Collaboration [49]. The object-oriented code written in C++ is available under the GPL license. It aims to simulate individual interactions for particle cascades in any material using Monte-Carlo methods. The toolkit has applications in various fields, including high energy, nuclear, accelerator physics, and medical and space science. The software was designed to cover all relevant aspects the user needs for a particle physics simulation, such as

- geometric layout of the experiment
- injection and tracking of particles
- definition of physical properties of the materials and particles
- extraction of the results
- visualization of the detector setup and particle trajectories

The core software package includes an extensive set of physical models covering a large range of particle energies and interactions. This allows the user to focus on detector design. The user is required to define multiple aspects of the simulation: the geometric details of the experiment, the tracked particles and interactions, material properties, the desired observables, and the injected particles. This is done either by using high-level commands in a macro file or hard-coded in C++. While the first option is easier to use, hard-coding the implementation in C++ allows for greater flexibility. Therefore, the latter was the choice in this simulation.

3.1 GENERAL GEOMETRY

The general workflow for defining the geometry of a detector element has three steps: in the first step, the user defines a solid object from provided so-called "primitive volumes" such as spheres, boxes, cylinders, and cones. Many primitive volumes can be combined to form more complex volumes using "boolean operations" like union, intersection, and subtraction.
In the second step, this solid volume is linked to a material defining the solid's physical properties, creating a logical volume. Physical properties include but are not limited to the refractive index, the chemical composition or absorption, and scattering length.
In a final step, this logical volume is placed inside the simulated "world" by

defining the position and orientation relative to a "mother volume" coordinate system. It is possible to place one logical volume multiple times, creating identical objects at different positions. In the terminology of geant4, a "mother volume" is defined by a volume that fully contains the "daughter volume" (the volume that will be placed). As a result, a hierarchical order of volumes placed in each other is created, with the outermost volume being the "world volume". Since P-ONE is still in its developing phase, the geometry and the components for the optical module are still being investigated. This means that none of the listed components are finalized and are subject to change in the course of the development of the optical module.

3.1.1 GLASS SPHERE

The first component of the geometry is a model of the glass sphere. In geant4, it is modeled as a whole sphere with an inner radius of 201 mm and an outer radius of 216 mm. This is according to the specification of a VITROVEX® 17" glass sphere produced by Nautilus GmbH [50]. The sphere is the standard (borosilicate) glass from Nautilus. Different sized versions in the range of 13" to 17" of this spherical pressure vessel have been proven successful and reliable in the modules for the pathfinder mission STRAW-b [38] and in the DOMs (Digital Optical Modules) of KM3NeT [51].
We modeled a 17" sphere, as its advantages (additional room for PMTs and electronics, easier heat dissipation) will likely outweigh the disadvantages (larger and heavier modules which are more difficult to maneuver).

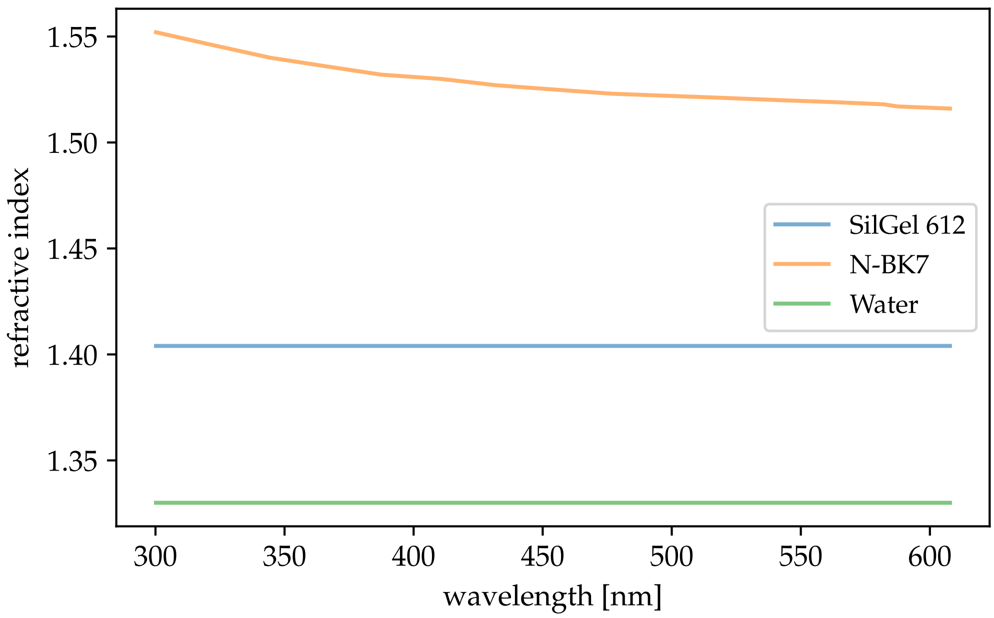

Figure 3.1: The refractive indices used in the simulation. Data for borosilicate glass is taken from [52], for water [53] and the optical gel [54] at 589 nm.

For the material of the glass sphere, we used publicly available data of borosilicate glass, as there is no data published for the refractive index of the VITROVEX® glass sphere [52]. Figure 3.1 shows the refractive indices of the relevant materials used in this simulation.

3.1.2 PMT

The PMT is one of the most vital components of the optical module. Differences in the PMT characteristics can significantly affect the module's overall performance. In this simulation, we modeled the PMT as close as possible to one of the possible PMT counterparts, also taking care of its internal structure. To do so, the following components need to be taken into account:

AN OUTER HOUSING produced, in most cases, out of borosilicate glass. Although other materials like Sapphire, Synthetic silica, or MgF2 crystals are also used, albeit less common. The outer housing gives the PMT its characteristic shape and houses the amplification stages (dynode system) and the photocathode's photon collection area.

PHOTOCATHODE: A thin coating on the inside of the curved upper part of the glass housing. For the PMTs relevant for the prototype line, this is either Bialkali or Super-Bialkal, similar to Bialkali but with a slightly higher QE. This surface converts photons into electrons using the photoelectric effect

REFLECTOR: A curved surface mirroring the shape of the photocathode made out of highly polished metal with an open region in the center to allow electrons emitted on the photocathode to reach the first stage of the dynode system. Due to the finite depth of the photocathode layer, not all photons reaching the photocathode will emit a photo-electron. This surface reflects photons to the photocathode, increasing the chance of emission of an electron and thus effectively increasing the quantum efficiency.

Due to the nature of the development phase, the final model of the PMT is still under investigation and yet to be fixed. We used the R14689 from Hamamatsu as a baseline for the model in the geant4 simulation. We decided to model this one because of the slightly larger photocathode area with an effective diameter of min. 81 mm [55] compared to other candidates, which have a diameter of min. 72 mm.
Modeling the PMT accurately in geant4 proves to be challenging as it is the most complex component in this simulation. Therefore, a few simplifications needed to be made. First of all, the upper curved surface is modeled as a spherical object with a constant radius and a maximum value for θ which can be calculated using trigonometry and the values defined in the data sheet. The material is standard borosilicate glass using publicly available data for the refractive index [52].

The reflector surface is modeled by mirroring the glass surface and giving it reflective properties. In geant4, the user has different options when implementing optical boundary processes. This is usually achieved by "wrapping" a given logic volume with a so-called "G4OpticalSurface". If a particle's position changes volumes (the starting point of this step is still in the old volume, but the endpoint is the new one), a 'forced' condition is calculated and applied, e.g. a reflection. When choosing to implement a G4OpticalSurface, the user must define several things. First, defining which simulation model shall be used for the boundary process. Here, the GLISUR - model has been chosen. Secondly, the type of interaction needs to be defined. In this case, it is an interaction between a dielectric and a metallic medium, this means that geant4 limits the available processes at this boundary to only absorption and reflection. In a final step, the surface properties needed to be defined. To model a very, but not perfectly, polished surface, we chose the GROUND - finish with a high polish value set to 0.9. This finish creates a rough surface with 'micro-facets', whose normals are added to the average surface normal to calculate reflection. The polish value adjusts how large the added normals are. The inner volume of the PMT, enclosed by the glass and the reflector, is filled with a volume with the material and refractive index of vacuum, and a detection volume is added below the glass.

There are two approaches when one wants to detect photons in geant4. As seen in other similar studies [31], the first approach is to define a detection volume that registers particles as soon as they enter it, marks them as detected, and terminates them. In this case, the QE is simulated by applying an efficiency factor afterward in the analysis. This is reasonable in many cases, as it reduces the complexity of the model. However, a different approach is taken by modeling the PMT in more detail and to cover cases that would otherwise be neglected. In this simulation, we assign an artificial material to the detector volume, with the refractive index of borosilicate glass (to exclude refraction between the glass and the detector volume) and an absorption length. The value for the absorption length has been chosen such that the mean absorption probability of the detector volume, which has a thickness of 1 mm, is roughly 25 %. This is an optimistic, but not unreasonable, estimate of the quantum efficiency of a PMT suitable for the prototype line.

The last component of the PMT is the complete lower body. Its primary purpose is to block photons hitting the detector volume from the lower hemisphere, as this is an unrealistic process due to the geometry of the real PMT. Although its shape plays a subdominant role, the volume was nevertheless modeled to resemble a real PMT. As a consequence, also the material for it was irrelevant because photons are immediately terminated upon impact on the lower body.

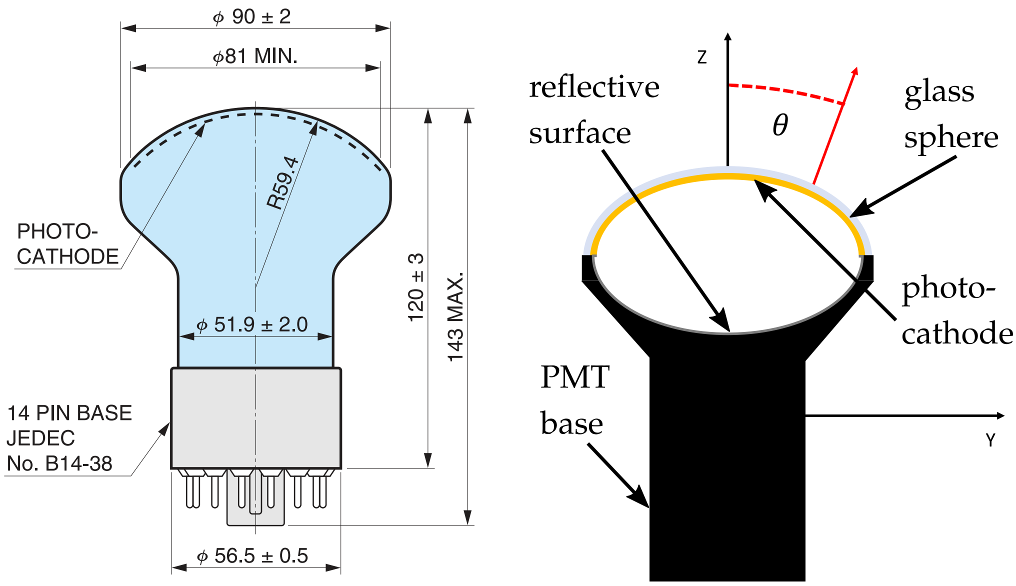

(a) Technical drawing taken from the data sheet of the R14689 from Hamamatsu [55]. The modeled PMT is based on these dimensions.

(b) Sectional drawing of the PMT as it was implemented in the simulation.

Figure 3.2: The left figure (a) shows a technical drawing of the PMT and on the right (b) a sectional sketch of the implementation of it is given.

Figure 3.2a shows the dimensions used for modeling the PMT in the simulation. The image is taken from the datasheet of the R14689 from Hamamatsu [55]. Figure 3.2b shows a sectional drawing of the PMT as it is implemented in geant4. The photocathode (yellow) and the reflective surface inside the PMT (grey) are marked. Additionally, the angle θ is defined relative to the rotational axis of the PMT and φ as the angle in the plane perpendicular to the rotational axis. The definitions are the same for the angles describing the incoming direction of the detected photons and the orientation of the rotated PMTs in the optical module.

3.1.3 THE REFLECTIVE COMPONENT

The last individual part is the reflective component. As explained in the section 3.1.3, the primary purpose of a reflective component around the PMT is to increase the effective area of a single PMT. This is achieved by reflecting photons towards it, which would otherwise miss the PMT. A common approach, as seen in the designs of the DOM of KM3NeT [56] and the mDOM for IceCube Gen2 [31], is to use a conical reflector made out of polished metal around each PMT incorporated in the entire holding structure, which keeps the PMTs in place. Although this has proven itself successful, it does have some drawbacks.

First, having metallic components near a PMT can result in a disturbance of the electric field of the PMT, which can lead to a worse transit time spread

(TTS), reducing the overall resolution of the PMT.
Furthermore, the integration of the reflector into the holding structure makes the whole optical module very non-modular. Because the whole holding structure is then glued to the glass sphere with cured optical gel. Meaning that if there should occur failure during testing of the optical module, it can be challenging to exchange the broken part.
These challenges were the reason why we decided to test a different approach for the optical module in P-ONE: using gel pads as a reflector. In this approach, the metal reflector is essentially removed and only the gel is left (see the image of the module with a gel pad in figure 3.3 for reference). This uses the total internal reflection between the optical gel (with a refractive index of ≈ 1.4) and the air in the module for the reflection.
The gel pad is the most complex part to model in geant4. It is not comprised of an individual predefined solid. Still, it is instead defined by the surrounding solids, namely the glass sphere, the PMT, and a conical volume resembling the reflector-side. To implement this, multiple boolean solids needed to be combined. We chose the material for the gel to be similar to the material used for the glass, with the main difference that the refractive index was replaced with 1.404 [54]. This is the refractive index of the SilGel® 612 from WACKER for the sodium D-line (589 nm) at 25 °C, which is one of the gels tested in the course of this thesis. Figure 3.3 shows the complete module inside the glass sphere.

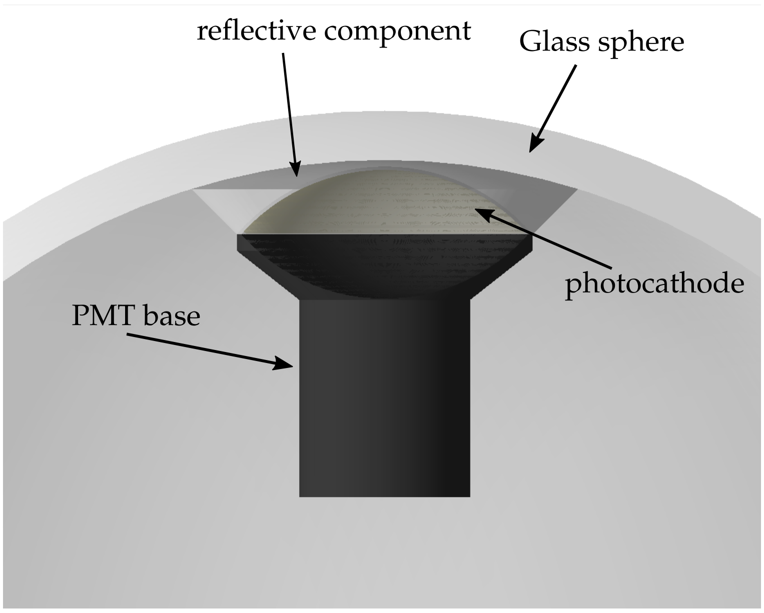

Figure 3.3: Image of the PMT with the gel pad inside a glass sphere in the geant4 simulation.

3.1.4 THE MULTI-PMT MODULE

The final step is to combine the components introduced in the previous sections in a so-called multi-PMT module. In contrast to the optical module from IceCube, which consists of one large 10-inch PMT facing downwards, this approach aims to combine several small PMTs in the range of 3" to 3.5" in a single module. A similar approach is already used for the optical module of KM3NeT [56] and is also considered for the IceCube Upgrade and IceCube-Gen2 [57] optical module. This has several advantages:

PHOTOCATHODE AREA: Combining multiple smaller PMTs results in a larger photocathode area compared to just a single large PMT.

BACKGROUND REDUCTION: Compared to the low ambient background of the antarctic ice, deep sea-water has two large sources of background contributing to a background baseline rate in the order of 10 kHz with spikes as high as several MHz per PMT [35] radioactive decay of ^{40}K potassium isotope and marine bioluminescence [35]. These processes are not correlated on the time scale of a few nanoseconds. By requiring coincidence hits in two or more PMTs of a single optical module on this time scale, the mainly uncorrelated background can be efficiently suppressed [58].

Due to the PMT configuration still being in development, we made some assumptions:

1. We assumed a total quantity of 14 PMTs per optical module. One hemisphere houses one PMT facing upwards, two rows of three PMTs each with an inclination of 45°, and 60° respectively, relative to the axis defined by the upwards facing PMT and evenly distributed in a row with the second row rotated by 60° relative to the first one. A rendering of the version of the optical module on which this simulation is based is presented in Figure 3.4.

2. To reduce the computational load, we utilize the spherical symmetry of the system. We create a full simulation by modeling a single PMT and then rotating it. Details on the performance of this approach are presented in Figure 3.10.

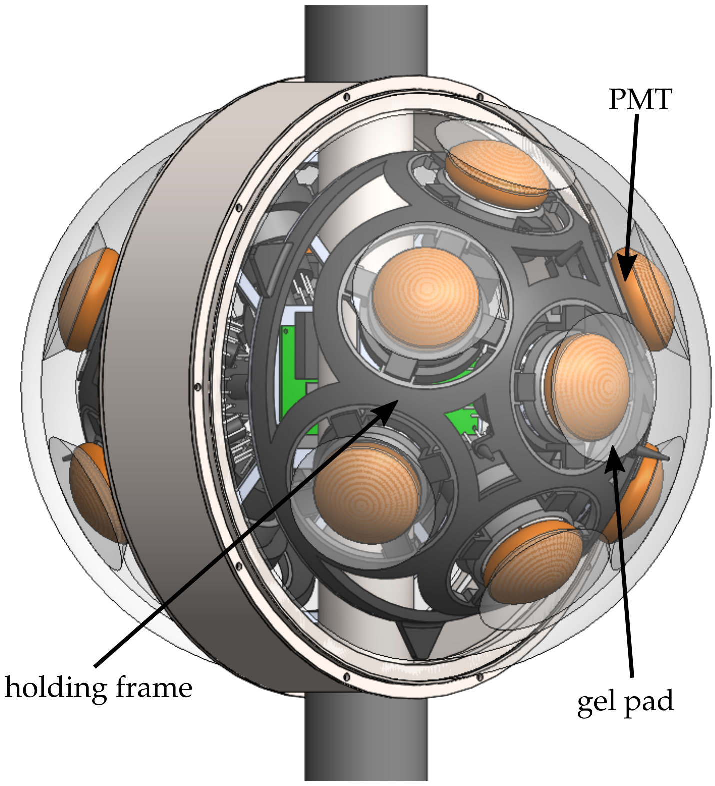

Figure 3.4: Preliminary render of the optical module which we used fo modeling in geant4. Courtesy of L. Papp and C. Spannfellner.

3.1.5 PHYSICS AND PRIMARY PARTICLES

Besides implementing the geometry, as discussed in the previous sections, the physical processes need to be defined and/or implemented. Fortunately, geant4 provides various physics models, and the user is only required to compile a so-called *physics list* in which the relevant processes and interactions are defined.
Section 2.2 covered the physical processes relevant for deep-sea neutrino telescopes. Simulating all processes is computationally not feasible. Hence, this simulation focuses only on optimizing the detection of low energetic photons (as they are expected by Cherenkov processes) and ignoring all production mechanisms of such photons. Therefore, this simulation represents one step out of the many needed for a full detector simulation. Such a simulation chain would involve neutrino and secondary particle propagations and interactions, calculation of Cherenkov light yield of the secondary particles, photon propagation, and detection (the latter is performed with a simulation like this), simulation of the hardware (DAQ, PMT, electronics) and event classification and reconstruction. Therefore, this simulation wants to answer the question: if an optical photon produced in an arbitrary physical process) from a given direction hits the optical module, what is the probability of detecting this photon? This is known as angular acceptances.
Consequently, this simulation does not need to implement more than photon

propagation of optical photons. Additionally, no scattering and absorption processes have been taken into account. This is because attenuation processes are intentionally not desired when producing angular acceptances. And since borosilicate glass and optical gel generally have much larger scattering and absorption lengths than their thickness, which a direct consequence of the inherent transparency, these processes play such a minor role that they can safely be neglected. Only for the detection of the photons, the absorption does play a role, and therefore it is implemented (see section 3.1.2 for details on the implementation of the PMT). This means that the only other physical processes simulated are refraction and reflection.
When one wants to simulate photons in geant4, there are two primary particles to choose from:

g4gamma This particle class is usually used to simulate secondary particles from radioactive decays and other high-energy processes with much larger energies than photons in the optical spectrum.

g4opticalphoton Is used when simulating photons with lower energy (e. g. in the optical range) where the wavelength is much larger than the atomic spacing. This means, that their wavelike nature can be applied [59]. Available processes for these particles are bulk absorption, scattering (both Rayleigh and Mie-scattering), and refraction and reflection at medium boundaries (which is needed in this simulation).

Generally, those two particle classes are not interchangeable and as the Cherenkov process produces light in the optical range, we decided to use G4OpticalPhoton as the primary particle in this simulation. Table 3.1 summarizes all the processes in this simulation.

process	geant4 class	description
refraction	G4OpBoundaryProcess	Boundary process of optical photons when they change the medium. A refractive index needs to be supplied.
reflection	G4OpBoundaryProcess	Boundary process of optical photons when they change the medium. Either through total internal reflection or when medium is defined as reflective.
absorption	G4OpAbsorption	Only applicable when absorption length is supplied. Used for detecting photons.

Table 3.1: Summary of the processes of the primary particle taken into account in this simulation [59].

The generation of primary particles in geant4 follows a hierarchical order. On the highest level, the particle generation consists of a *run*. A run is es-

sentially a collection of events that share the same detector conditions. As a consequence, the user cannot alter the detector geometry or the physical processes which are simulated within a single run. A single *event* consists of the primary particles together with their respective information on trajectories, energy losses, and so on. Additionally, also the user-defined observables are initiated for every particle in this instance. The observable which we are extracting from the simulation are the initial and final position and direction, and the energy of the particle. The current snapshot of a particle, called a *track*, contains the most recent values of the observables. If it fulfills the criteria for detection, the particle is removed from the simulation and the observables are written to an output file. This can happen due to several reasons like the particle leaving the world volume, decay, kinetic energy reaching zero, or if the user terminates it. The last one is used to prevent particles from traversing the absorbing base of the PMT.
The smallest individual unit is the *step*. All physical processes are calculated on the step level. It consists of two points in space and the delta information of the particle such as energy loss, time of flight spent per step, and more depending on the implemented physics of the simulation. Additionally, each endpoint of the step knows the volume and material it belongs to. The step size is drawn of the possible interaction lengths, weighted with their probability. In the case of the endpoint, there is one exception to this: if the endpoint of the step should result in another volume than the start point, the boundary between those two volumes defines the endpoint. This ensures that processes like refraction and reflection are properly simulated.
The last thing which needs to be provided is the generation of the particle. To do this, geant4 has several methods. The most primitive one is called *G4ParticleGun* which shoots one primary particle with given energy from a certain point into a certain direction. As one can see, this function has very limited functionality and is not suited for complex sources. Therefore geant4 provides the *G4GeneralParticleSource* method which allows defining different particles, energies, and spectra but also lets the user define an expanded shape of the source, direction, and opening angle of the primary direction of the injected particles.
Now that we have covered the structure of the simulation, we will take a closer look at the two different situations, which we simulated:

ANGULAR ACCEPTANCE IN WATER The first case covers a multi-PMT optical module in water. This is used to evaluate the angular acceptance of a given configuration. This paragraph focuses on the calculation of the angular acceptance for a single PMT. For details of the multi-PMT module see section 3.2. This situation has been done in other simulations by calculating an effective detector area of a plane wavefront. The effective area is hereby defined as the number of detected photons relative to the number of emitted photons of a disc with a constant density profile, single energy, and a direction given by the angles θ and φ and multiplied by the area of this disc. This approach can be used as the spherical emitted Cherenkov photons can be approximated

as a plane wavefront at large distances from the emission point. Details on the Cherenkov effect are outlined in Section 2.1.2. This approach has some drawbacks. Namely, that a separate simulation needs to be started for each direction as the geometry of the source needs to be redefined.
An alternative approach to counteract these disadvantages is to define a spherical source with the optical module in the center of it. The photons are emitted homogenously towards the center of the sphere with a maximum opening angle defined by the diameter of the sphere which is 432 mm. The emittersphere itself has a radius of 50 m. This results in an error due to the non-vanishing opening angle of less than 0.1 %. Therefore, this implementation is a reasonable approximation of a plane wavefront. Lastly, the simulation uses monoenergetic photons with a wavelength of 450 nm. This wavelength was chosen because the dominant part of detected photons are in the blue band (folding of the Cherenkov emission profile with the attenuation length of seawater) and the STRAW experiment, one of the pathfinder missions for P-ONE, uses a LED of this wavelength for attenuation measurements [35].
The approach assures that all emitted photons will hit the optical module. As a result, the angular acceptance or detection efficiency as a function of the angle of incidence can be defined by

$$\eta_{det}(\theta, \varphi) = \frac{N_{det}(\theta, \varphi)}{N_{emit,avg}} \tag{3.1.1}$$

$N_{det}(\theta, \varphi)$ is calculated as a two-dimensional histogram over the initial directions of the detected photons. Special care needs to be taken for the bin widths in theta to ensure equal-sized bins because the surface area element of a sphere is scaled by $\sin(\theta)$. This is achieved by scaling equal-sized bins x with $\arccos(x)$.

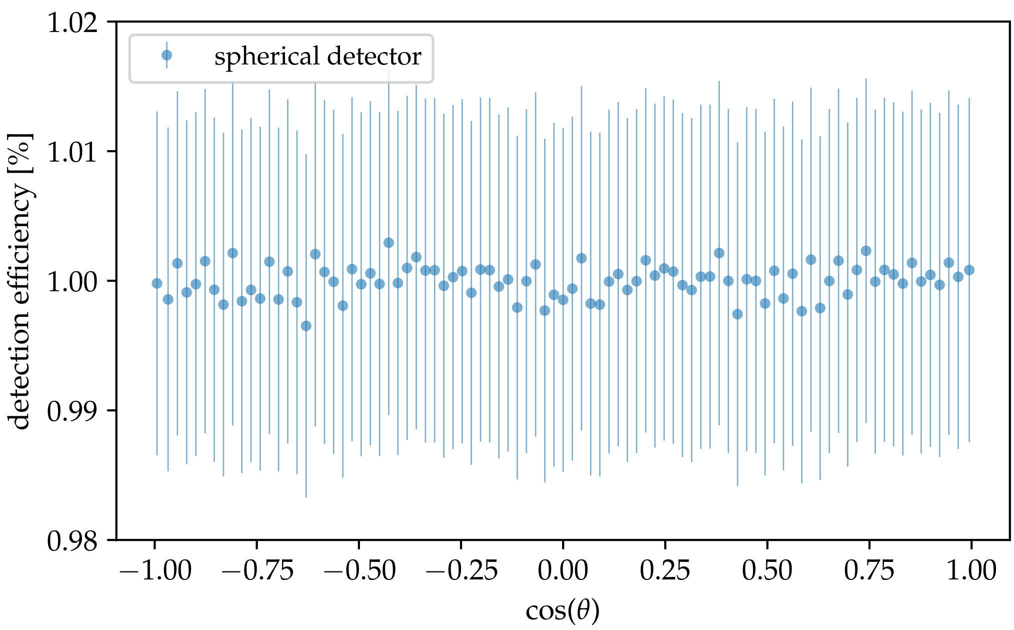

Figure 3.5: Detection efficiency for 2.1×10^9 emitted photons for a spherical emitter with homogeneous emission and non-linear bins in theta.

Figure 3.5 shows the result using these non-linear bins. The input for the histogram is all emitted photons from a spherical emitter as it is used in this simulation. The result is constant within fluctuations caused by the randomness of the emitted photons. The average number of emitted photons per solid angle bin is defined by

$$N_{emit,avg} = \frac{N_{emit,tot}}{(n_\theta - 1) \cdot (n_\varphi - 1)} \tag{3.1.2}$$

where $N_{emit,tot}$ is the total amount of emitted photons per run and n_θ, n_φ defines the number of bins for the given angle which are used in the histogram. This effectively adjusts how fine the grid is on which the data is evaluated. At the same time, it changes also the number of emitted photons per bin and thus decreases the statistic, resulting in a trade-off between finer sampling and less statistic. The most significant advantage of this is, that it can be performed during offline analysis. In that case, the time and computational power-intensive simulation in geant4 needs to be performed only once for a given hardware configuration.

SENSITIVITY IN THE DARKBOX A dark box was used to validate the performance of a given PMT with and without a gel pad in a controlled lab environment. Such a calibration station for pending PMT candidates was developed in parallel to this work in the group, the setup will briefly be described in Chapter 5.

For this setup some alterations needed to be made to the detector geometry, namely the material of the world was changed to air, the pressure vessel was removed, and depending on the setup also the gel pad. The geometry of the particle source is still spherical. The rotation of a collimated beam is identical to the rotation of the PMT around the rotational center of the photocathode. This means that there is a maximum angle θ_{max} between the axis of rotation and the direction of the laser beam with which the PMT still detects light. Therefore, the spherical source was limited to a spherical cap defined by an angle in the range of θ_{max}. This results in a denser photon emission as the same number of photons are distributed on a smaller surface, allowing for a finer binning. In addition, the wavelength spectrum of the emitted photons was changed to a gaussian with a mean of 405 nm and a FWHM of 5 nm corresponding to the specifications of the laser used in the calibration station [60].

3.2 RESULTS

Now that the implementation details of the simulation in geant4 is covered, the following will focus on the results of the simulation. Due to the early stages of the development of the optical module, many parameters are still preliminary and open for optimization. Hence some of the parameters needed to be fixed like the geometry of the PMT, as well as the number and position of individual PMTs in the optical module to perform the simulation. This simulation covers the performance of a transparent reflector compared to a solid one in a multi-PMT configuration with varying opening angles of a conical reflector. The results of a single PMT in the optical module will be discussed and followed by the simulation results of the multi-PMT module.

3.2.1 REFLECTOR ANGLE STUDY OF A SINGLE PMT

Before simulating a complete module, the impact of the opening angle of the reflective component was investigated. The opening angle is defined as the angle between the cone of the reflective component and the axis of rotation. The shape of the reflective side was not subject to change, although different shapes apart from a standard cone like an ellipsoid or a Winston cone are possible. Other shapes were not considered mainly for two reasons: It would have increased the already large parameter space. And this was investigated in a similar work for the LOM, a new development of the optical module for the IceCube upgrade, and the results showed no significant difference for an ellipsoidal reflector compared to a conical [61].
The setup for the simulation as described in the section 3.1 consists of one PMT in a glass sphere facing upwards. Depending on the setup, a reflective material around the gel pad or only the gel pad is simulated. To get a reasonable high statistic for each bin, 2.1×10^9 photons were emitted over the whole sphere, resulting in approx. 1.3×10^5 emitted photons per integration bin. This leads to a relative statistical error of maximum 5 % in the upper hemisphere. However, due to the inherently very low detection efficiency in the lower hemisphere, the overall relative error reaches up to 20 % depending on the opening angle. Since this region is not of interest for this simulation, we did not consider further increasing the number of simulated photons as this substantially increases computation time and complexity.
Figure 3.6 outlines the relative error for a transparent reflector with an opening angle of 40°. For this analysis, we used 180 bins for azimuthal and zenith angles respectively. The coarser binning in azimuth is due to the rotational symmetry of the simulated system, hence we expected that differences in this direction are only dependent on the inherent randomness of the emitted photons.

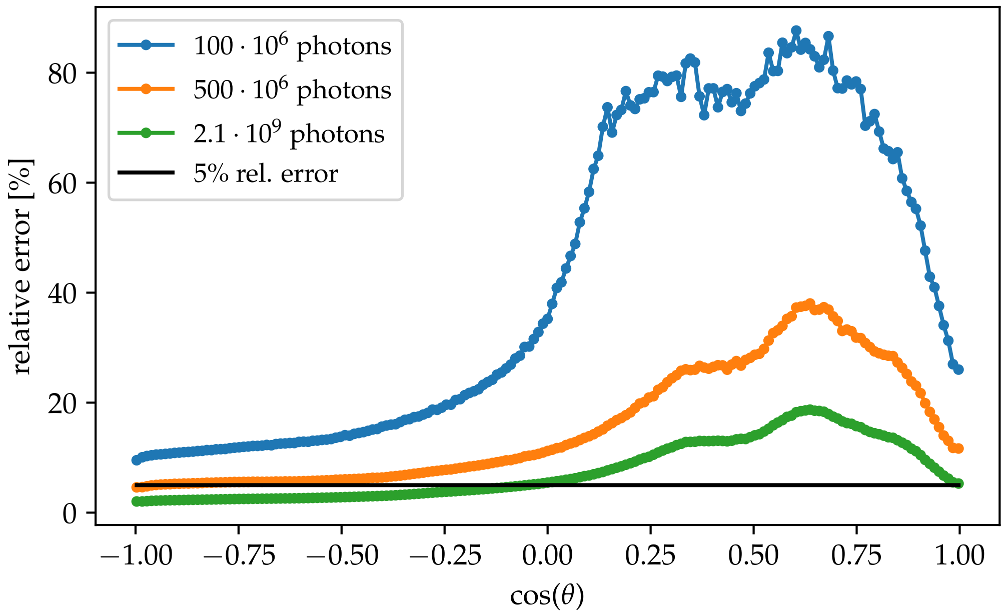

Figure 3.6: The relative statistical uncertainty of the detection efficiency resulting from $\sqrt{N}$ uncertainties for a different number of injected photons assuming a Poissonian distribution when averaging over the azimuth angle. The result was derived from a transparent reflector with an opening angle of 40°.

Figure 3.7a and 3.7b presents results for the detection efficiencies of different incidence and opening angles for a solid reflector and a transparent reflector. The result for the solid reflector has its maximum detection efficiency for photons arriving perpendicular to the entrance window at an opening angle of 50°. With a steep decline for larger and smaller opening angles. Albeit similar, the gel pad yields a maximum detection efficiency for an opening angle of 40°, also for photons perpendicular to the entrance window. A detailed plot of the result is shown in Figure 3.8.
Although these angles result in the overall maximum of the detection efficiency for their respective configurations, they don't necessarily correspond to the angles that optimize the detection efficiency for an optical module in the deep sea. This has several reasons:

1. These values only correspond to photons with an angle of incidence of 0°. As it can be seen in the Figure 3.7a and 3.7b, the detection efficiency is declining with increased angle of incidence but non-zero until a maximum angle. This angle is lower for the solid reflector as it additionally blocks photons which could still be detected with a transparent reflector. Large angles of incidence result in a substantial path inside the optical module and should be disregarded as this region will be filled with hardware blocking these paths. But since the geometry of this hardware is still undefined and therefore no maximum angle of incidence can be specified, this effect is not considered.

2. These values only yield a result for a single PMT. Having multiple PMTs inside the optical module might very well change this result. Effects of this are discussed in Section 3.2.2.

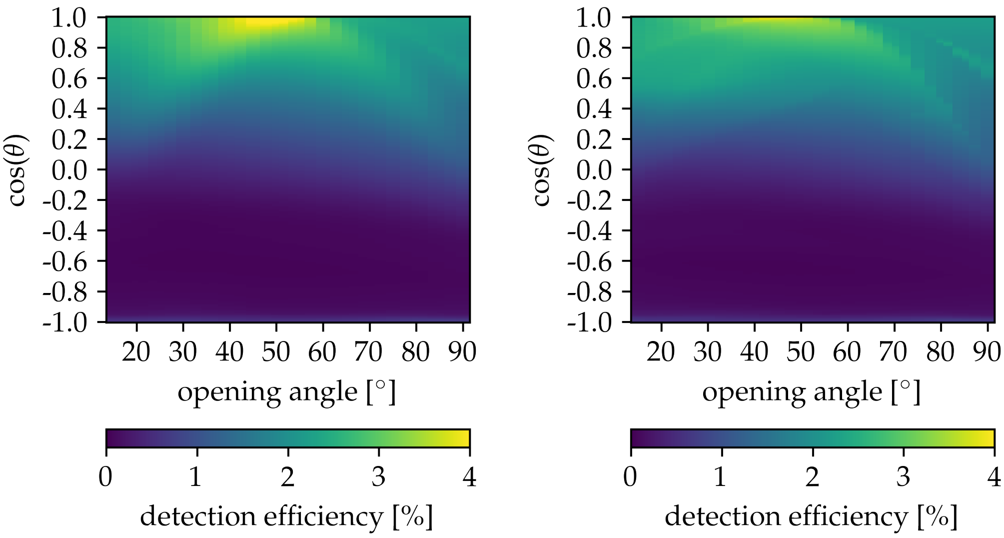

(a) solid reflector

(b) transparent reflector

Figure 3.7: Angular acceptance as a function of the angle of incidence and the opening angle for a solid and a transparent reflector. For a detailed discussion refer to the text.

The shape of the detection efficiency in respect to the incidence angle changes for different opening angles of the cone, e. g. the maximum non-zero value increases for larger opening angles towards larger incidences angles.
For larger opening angles, the maximum detection efficiency shifts towards larger angles of incidences for the gel pad. This shift is because the condition for total internal reflection at the gel pad - air boundary is not anymore fulfilled for a photon with a small angle of incidence.
Lastly, for very large angles of incidence (160° and more), the detection efficiency rises again. This is due to some photons fulfilling the internal reflection condition at the glass sphere - air and glass sphere - water boundary. Therefore they traverse inside the glass sphere to the upper hemisphere where the PMT can detect them.

Figure 3.8 shows the detection efficiency for photons arriving perpendicular to the entrance window of the PMT for a transparent and a solid reflector. As discussed before, the detection efficiency for a solid reflector shows a well-defined peak for an opening angle of 50°.
This is compatible to results from KM3NeT and IceCube. KM3NeT ultimately decided for an opening angle of 45° [62, p. 4] and studies for IceCube on the mDOM and LOM found values of 51° [51, p. 186] and 50° [61, p. 38]. Differences to these values can be attributed to different PMTs and models of the PMTs in geant4. KM3NeT used the XP53B20 from Photonis, which was later discontinued, the mDOM study used the R12199-02 by Hamamatsu, and the

LOM study modeled a 4 " PMT.
In contrast, the transparent reflector shows a much broader peak with its maximum at 45° and with a quick decline afterward as the condition for the total internal reflection for vertical photons is not fulfilled anymore. The rising slope for small opening angles is similar in both cases. Comparing this to the study of the LOM [61], we find some differences. Most notably, the peak is significantly shifted. The simulation of the gel pad for the LOM yielded a maximum opening angle of 60°. The discrepancy might be attributed to the differences in the geometry of the optical module. As the LOM is smaller and elongated compared to the spherical pressure vessel P-ONE will use.
The third prominent feature is the difference in detection efficiency. Although the values are very similar until roughly 35°, values for the transparent reflector quickly decline, resulting in the peak for the solid reflector being ≈ 10 % higher compared to the transparent reflector.

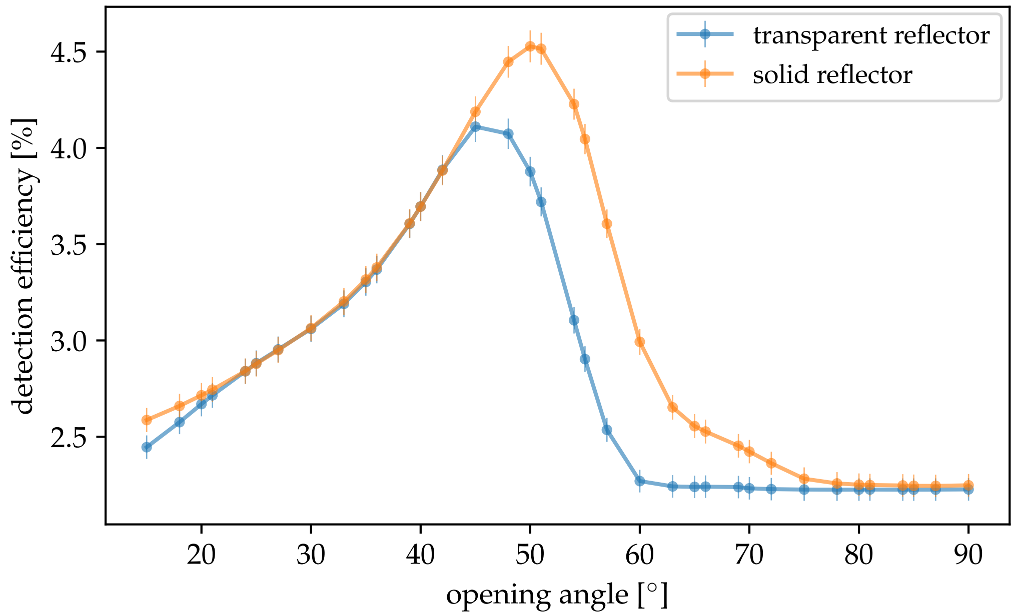

Figure 3.8: Detection efficiency for photons with an angle of incidence of 0°. Errors indicate statistical 1σ uncertainties. 2.1×10^9 were simulated.

Lastly, we simulated the mean detection efficiency over all directions. Figure 3.9 shows the simulation result for this case. The result for the transparent reflector did not show any significant dependency on the opening angle, whereas the result for a solid reflector drops for low opening angles. The largest mean detection efficiency is 1.01(3) % for an opening angle of 35° for a gel pad and 1.03(3) % for an opening angle of 33° for a solid reflector. The comparably large uncertainties for the mean value can mainly be attributed to the increase of the error for very low detection efficiencies, as they contribute a significant amount to the mean value.

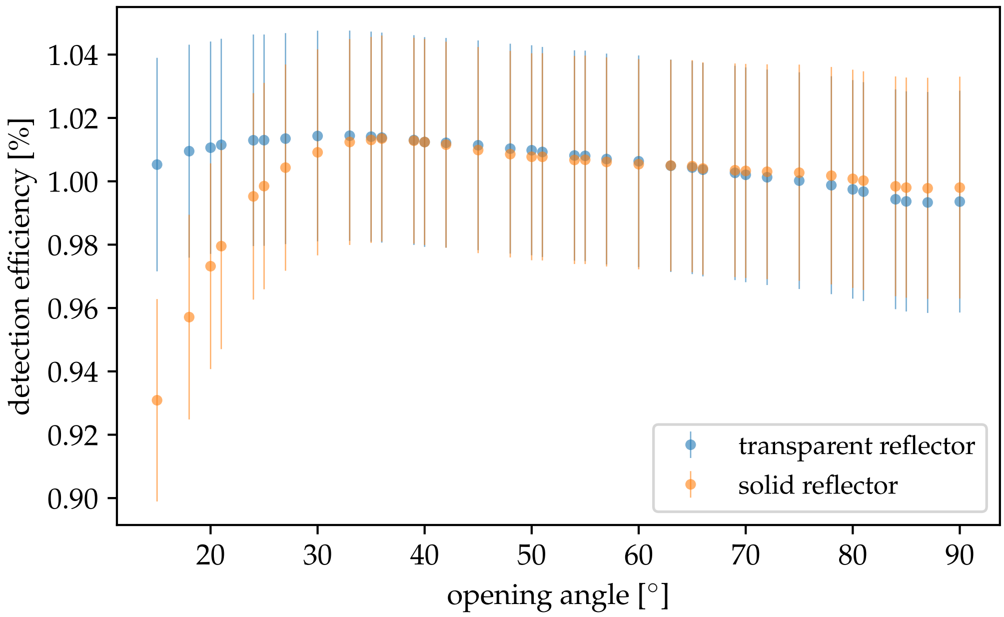

Figure 3.9: Mean detection efficiency for a solid and a transparent reflector. Errors indicate statistical uncertainties.

3.2.2 SIMULATION OF THE MULTI-PMT MODULE

In the previous section, we discussed the effects of different reflective components for a single PMT. This section will focus on the results for a multi-PMT module as it is described in section 3.1.4. Due to the inherently large background of around 10 kHz in the deep sea, one of the fundamental approaches to reduce it are coincidence hits. To account for this, we defined the figure of merit as "the average required minimum number of photons from an arbitrary direction which are needed for the optical module to have at least two PMTs detecting one or more photons with a probability of 95 %".
Mathematically speaking, this is equal to the following procedure:

1. Drawing random numbers from a multinomial distribution. Which is a generalization of the binomial distribution.
   In this case $n = n_{ph}$ is the number of photons and $p = [p_1, p_2, ..., p_{14}]$ are the detection probabilities of the 14 PMTs in the optical module for a given direction.

2. This is repeated for $m = 1000$ times to increase statistics and for every directional bin. Only trials, where one or more photons are recorded by at least two times, are counted. The result is normalized by m, resulting in a coincidence hit probability for a given number of photons.

3. This calculation is performed for different n_{ph} in the range of $\{30..80\}$. No smaller or larger values were calculated with this approach, therefore the range is sufficient. Afterward, the minimum number of photons for which the coincidence hit probability is at least $\geqslant 95\,\%$ is retrieved.

Errors were conservatively estimated by performing the calculations three times for all the following values. One time with the detection probabilities as an input and two times with their $\pm 1\sigma$ uncertainties. From the two additional results, always the largest difference to the mean result has been chosen as an error. As this is a conservative approach, it is prone to overestimate the errors, which should be kept in mind when interpreting the results.
We did not consider the uncertainties on the direction of the individual PMTs for this error estimation as it would further increase computation time. Sampling from a normal distribution for each direction and multiplying the resulting value with the direction would be an approach to simulate the errors.
While all opening angles were in principle allowed and therefore simulated for a single PMT, an optical module housing multiple PMTs puts more constraints on the geometry. One of them is that the reflective component of the simulated PMT must be small enough that it does not overlap with the reflector of adjacent PMTs in a given configuration. The overlapping would lead to complex structures of the reflector, which are challenging to model and even more difficult to manufacture. The current module configuration has no reflector overlay for opening angles smaller than $60°$.
Thus the result of the simulated upwards facing PMT can be rotated to get the detection efficiencies of the remaining PMTs. Figure 3.10a shows the two dimensional detection efficiencies from a PMT with a transparent reflector and an opening angle of $40°$ as simulated in geant4, Figure 3.10c shows the result after rotating the PMT by $\varphi = 60°$ and $\theta = 60°$ corresponding to the direction of one of the remaining PMTs in the optical module. Figure 3.10d shows the result of a geant4 simulation with a rotated PMT in the same direction. The maximum difference between these two results is less than $0.5\,\%$ and the mean difference is less than 1×10^{-5}.

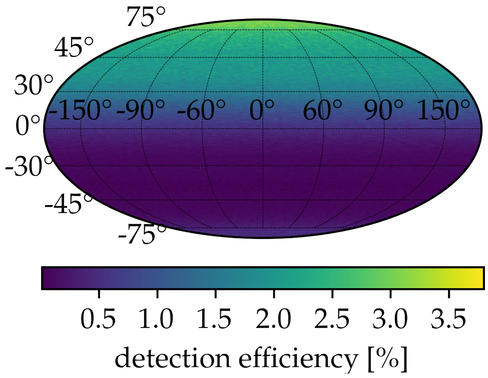

(a) Upwards facing PMT

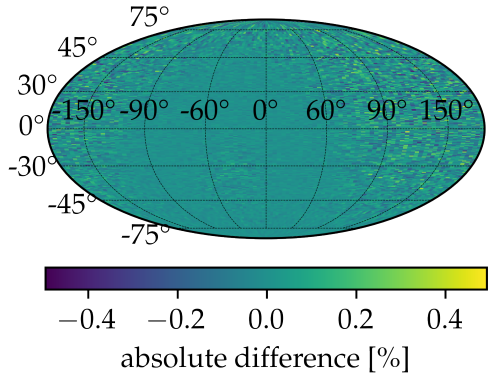

(b) Absolute difference between simulated rotated PMT and rotated upwards facing PMTs

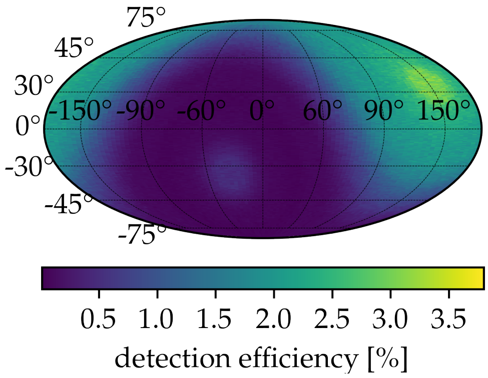

(c) Result from rotation of the simulated upwards facing PMT.

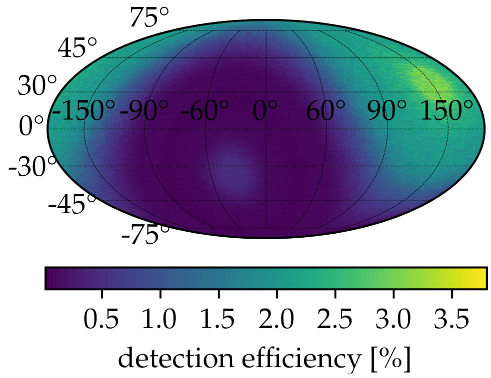

(d) Result for a simulated rotated PMT.

Figure 3.10: Detection efficiencies of a single PMT with a transparent reflector and an opening angle of 40°. (a) shows the result for the upward facing PMT which is used as a baseline for the rotated response, (b) the difference between the rotation of a upwards facing PMT and a simulated rotated PMT, (c) shows the result from a rotation of a upwards facing PMT and (d) shows the result of the simulation of a rotated PMT.

SOLID ANGLE HOMOGENEITY A homogeneous coverage of the total solid angle will be a crucial parameter for optimizing the final module configuration. A various number of parameters influences this homogeneity. Since most of them are assumed to be fixed (e. g. the multi PMT configuration), this paragraph will only focus on the influence of the opening angle. We evaluated the inhomogeneity by calculating the standard deviation of the minimum number of photons' overall directions for a given configuration. This is defined as:

$$\sigma_{\overline{n}} = \sqrt{\frac{1}{N}\left(\sum_{i=1}^{N}(n_i - \overline{n})^2\right)} \tag{3.2.1}$$

$$\overline{n} = \frac{1}{N}\sum_{i=1}^{N} n_i \tag{3.2.2}$$

$$\sigma_{\overline{n},\mathrm{rel}} = \frac{\sigma_{\overline{n}}}{\overline{n}} \tag{3.2.3}$$

Whereas n_i is the minimum number of photons for a given direction, $\overline{n}$ the average minimum number of photons over the total solid angle, and $N = n_{zen} \cdot n_{az}$ the combined number of bins.
The largest values were found for an opening angle of 40° for a transparent cone with an inhomogeneity of 8.6(30) %. The solid reflector has its maximum at 42° with an inhomogeneity not greater than 10.4(30) %. The reflector angles of the maximum are in line with the result for a single PMT, where the detection efficiency dropped fastest for an increased angle of incidence. Therefore the overlap of high angular acceptances of different PMTs is smaller compared to the result for higher or lower opening angles. Figure 3.11 shows the result for different reflector angles and the two configurations. Due to the conservative error estimate, the relative error is as large as 39 %. A less conservative estimate and more simulated photons in geant4 would improve the errors.

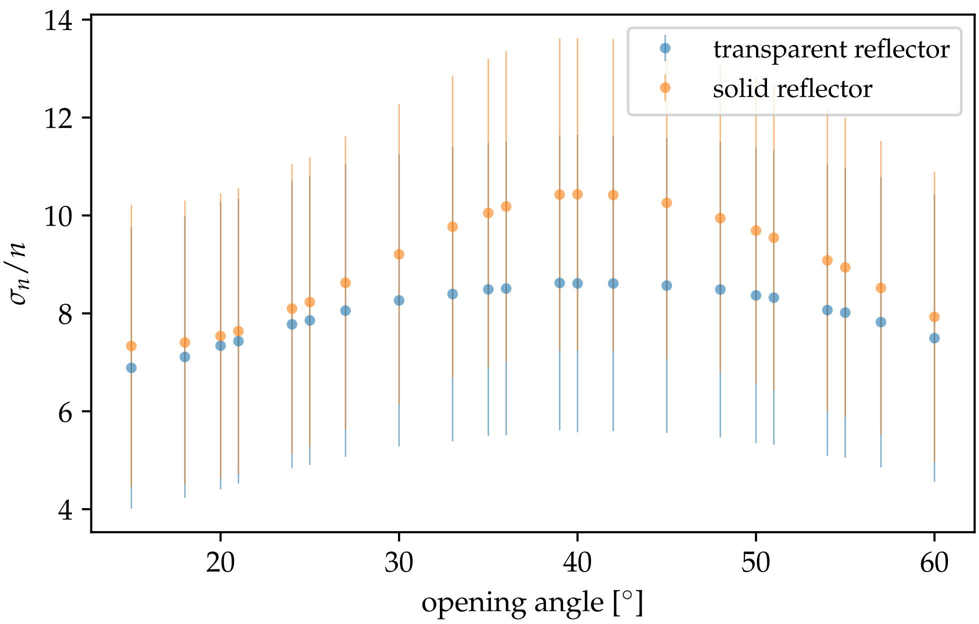

Figure 3.11: The standard deviation of the minimum number of required photons averaged over all directions.

The difference in the standard deviations showed a greater variation for the solid reflector compared to the transparent one.
The plots in Figure 3.12 show the minimum number of photons for every direction for a transparent reflector with an opening angle of 40° together

with the result when the uncertainties are applied to the detection efficiencies and the error. Varying the angular acceptance does not change the overall shape, as shown in figure 3.12b. The relative error has, within its statistical fluctuation, no angular dependence.

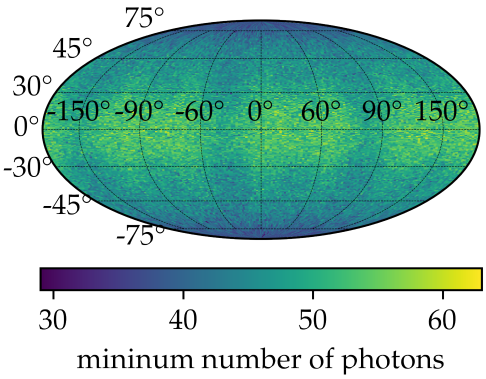

(a) Minimum number of photons derived from the angular acceptances of a 14 PMT configuration.

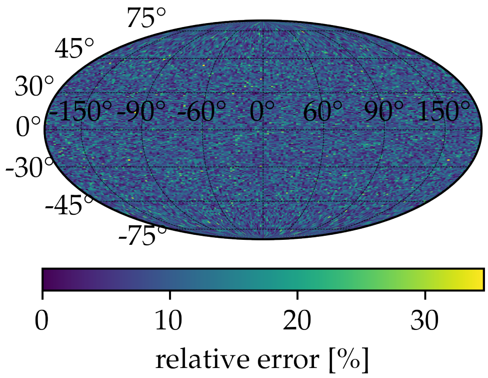

(b) Relative error derived from the error calculation.

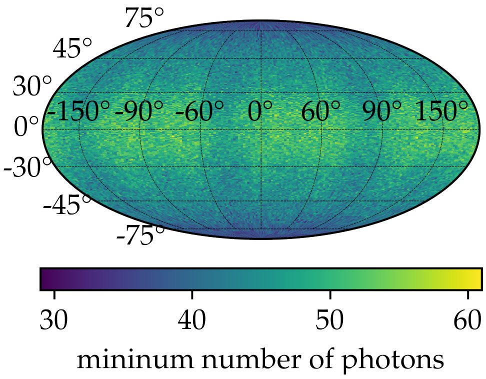

(c) Minimum number of photons derived from the angular acceptances of a 14 PMT configuration plus one standard deviation.

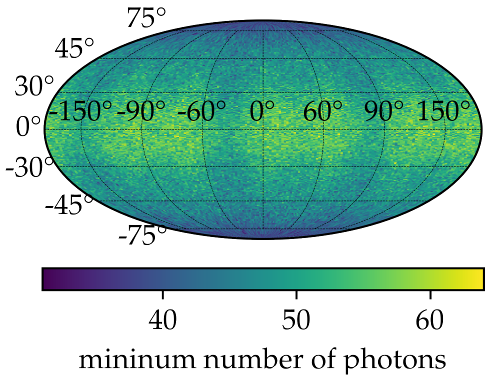

(d) Minimum number of photons derived from the angular acceptances of a 14 PMT configuration minus one standard deviation.

Figure 3.12: The required minimum number of photons, which are needed for the optical module to have at least two PMTs detecting one or more photons with a probability of 95 %. (a) shows the result for the calculated angular acceptances, (b) the relative error calculated from this configuration, and (c) and (d) the result with $\pm 1\sigma$ uncertainties.

MEAN RATIO Is a second method to assess the performance of different opening angles. The result was averaged over all directions and normalized on the result for an opening angle of 40° for a transparent reflector and 50° for a solid one. We chose these angles as they gave the best result for a single PMT with photons arriving perpendicular.

Figure 3.13 shows the result for both types of reflectors. We observed only small dependencies on the opening angle for both reflector types. For a transparent reflector, the lowest ratio (i. e. the best mean performance relative to the baseline) was an opening angle of 20° with a value of 0.98. In the case of the solid reflector, the lowest ratio is found for an opening angle of 27° with a value of 0.97. However, the errors are an order of magnitude larger than the differences to the baseline result for both reflectors. Two reasons for this might be the conservative approach on the errors and the missing statistics of the angular acceptance in the lower hemisphere.

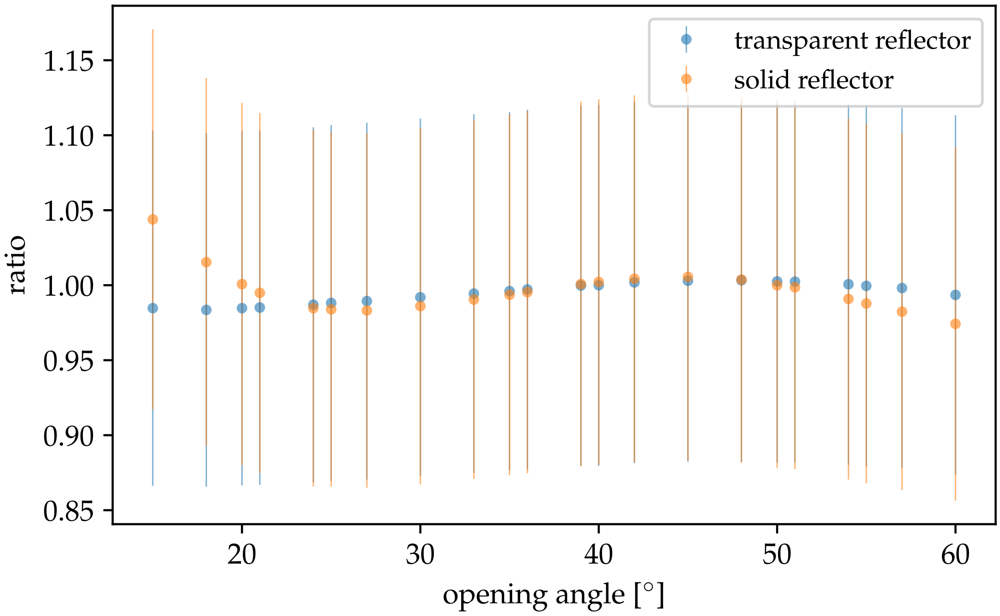

Figure 3.13: The ratio of the mean minimum number of photons. Baseline for the transparent reflector is 40° and for the solid reflector 50°. Errors are derived from the $\pm 1\sigma$ uncertainties of the angular acceptances.

AVERAGE OVER THE AZIMUTH ANGLE When calculating the overall inhomogeneity and the ratio of the mean, all directional information is inherently lost. To counteract this disadvantage, averaging only over one of the two angles preserves the information partially. In this paragraph, we present the average over the azimuth angle. Figure 3.14a and 3.14b presents the result of this calculation. Due to the symmetric orientations of the PMTs, the minimum number of photons were symmetric when averaging over the azimuth angle. The best performance for both types of reflectors were for photons arriving from above and below the module ($\theta \approx 0°$ or $\theta \approx 180°$). The reason for this lies in the denser packing of PMTs towards the top and the bottom. For these directions, no dependency on the opening angle was found. An opening angle of $\approx 45°$ for a solid reflector yielded the worst performance for photons arriving horizontally.
Similar observations were made for the transparent reflector. However, the gel pads yielded an overall 3 % better result over all opening angles with a smaller variability throughout the zenith angle. The results are consistent with the result of the maximum inhomogeneity study.

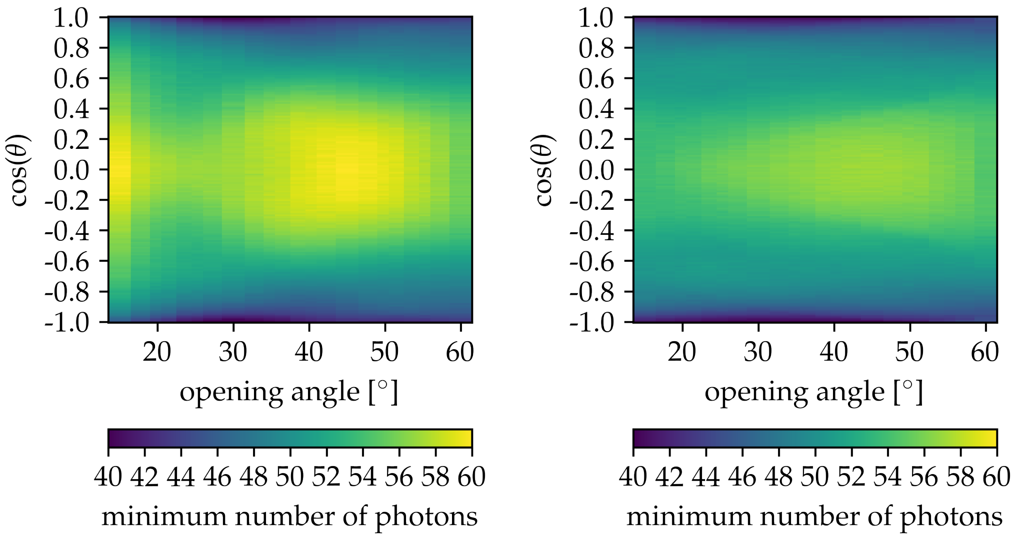

(a) Solid reflector (b) Transparent reflector

Figure 3.14: The minimum number of photons for different opening angles averaged over the azimuth angle. The y-axis shows the cosine of the zenith angle.

AVERAGE OVER THE ZENITH ANGLE The presented multi-PMT configuration has an inherent 3-fold axis of rotation symmetry. Therefore it is expected to see a repeating pattern when averaging over the zenith angle. This is confirmed as Figure 3.15a and 3.15b are showing.

The areas with a low minimum number of photons indicate the direction of the inclined PMTs, as there the detection efficiencies are larger compared to the remaining directions. The solid reflector exhibited a more significant variability for very small and large opening angles and a very uniform result for opening angles in the range of 40° to 50°. This contrasts with the result for the average over the azimuth angle as shown in figure 3.14a. However, the overall variability is also much smaller than the previous one. Therefore its contribution is less significant, and the variability in the zenith direction dominates the overall mean inhomogeneity.

A similar argumentation can be applied to the result of the transparent reflector. Additionally, differences are similar to the result from averaging over the azimuth angle. The gel pads perform according to the simulation overall 3 % better and the variability throughout the azimuth angles is lower compared to the solid reflector.

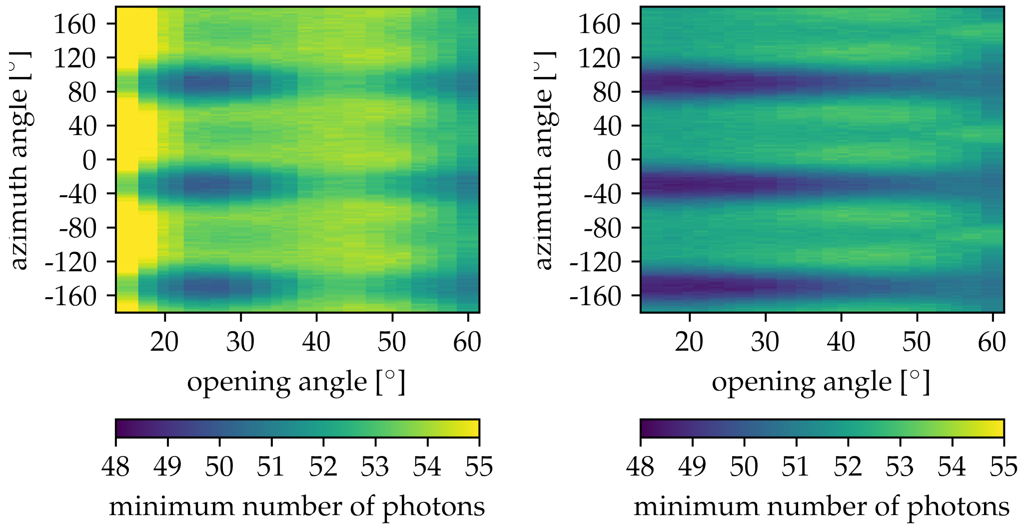

(a) Solid reflector (b) Transparent reflector

Figure 3.15: The minimum number of photons for different opening angles averaged over the zenith angle. Results are discussed in the text.

3.3 CONCLUSION

This chapter focused on evaluating two types of reflective components: A solid and a transparent reflector. The geometry of the PMT has been modeled with a novel and more realistic approach than previous similar studies.
At first, the performance of a single PMT in an optical module has been investigated. The results were evaluated by calculating the detection efficiencies for every solid angle bin. The highest detection efficiency was found for photons arriving perpendicular to the entrance window with an opening angle of 50° for a solid reflector and 45° for the gel pads with a 10 % larger value for the solid reflector. Additionally, we found that the overall mean detection efficiency of the gel pads had no significant dependency on the opening angle with its maximum at 35°. The solid reflector showed a drop in detection efficiency for very small opening angles and a uniform behavior, similar to the result for the gel pad for larger opening angles. The maximum is at 33°.
In a second step, we analyzed the results for a multi-PMT module. To compare different configurations, we used the "average required minimum number of photons from an arbitrary direction, which is needed for the optical module to have at least two PMTs detecting one or more photons with a probability of 95 %" as a figure of merit. It simulates coincidence hits which will be vital in reducing the apparent background in the deep pacific ocean. We constructed the multi-PMT module by rotating the result of a single PMT, which leads to a mean difference of the detection efficiencies of less than 1×10^{-5} when compared to a rotated PMT in geant4. Presumably caused by statistical fluctuations.

We found that the relative inhomogeneity over the whole sphere was not greater than 9 % for the transparent reflector and 10 % for the solid one. Due to the conservative error approach, the relative error on the inhomogeneity is as large as 39 %. Secondly, we calculated the mean minimum number of photons and normalized on the result of 40° for a gel pad and 50° for a solid reflector. With the lowest ratio of 0.97, we did not find a significant dependency on the opening angle.
Finally, we performed an average of only one of the two-directional angles. On average the gel pads performed 3 % better than the solid one. The best performance for photons coming from above or below (for both reflector types) was observed when averaging over the azimuth angle, which is explained by the increased density of PMTs in these regions. The average over the zenith angle showed a repeating pattern for both types of reflectors because of the 3-fold rotational symmetry. Additionally, the overall variation is much smaller compared to the average over the azimuth angle; hence these result plays a subdominant role in the overall homogeneity. Results for all studies are shown in Table 3.2 and Table 3.3.

	SOLID	TRANSPARENT
opening angle (perpendicular)	45°	50°
maximum detection efficiency	4.53(8) %	4.11(8) %
opening angle (mean)	35°	33°
mean detection efficiency	1.01(4) %	1.01(3) %

Table 3.2: Summary of important results of the study of a single PMT.

	SOLID	TRANSPARENT
minimum inhomogeneity	7(3) %	7(3) %
min. inhomogeneity (opening angle)	15°	15°
maximum inhomogeneity	10(3) %	9(3) %
max. inhomogeneity (opening angle)	42°	40°
lowest ratio (opening angle)	27°	20°
mean detection efficiency	0.97(10) %	0.98(10) %

Table 3.3: Summary of important results of the study of a multi-PMT module

Both studies exhibited large uncertainties on all calculated figures. Due to the low variability in the ratio and the inhomogeneity no clear optimal opening angle could be assessed in this work. Further simulations are needed to decrease the error and account for additional effects such as the uncertainties on the direction of the PMTs. As the transparent reflector has a lower inhomogeneity and a 3 % increased performance, it is the preferred solution for P-ONE.

4 PROTOTYPE-PRODUCTION

The previous chapter concluded that transparent reflectors, i. e. gel pads, perform at least comparable to the established solid reflectors when a single PMT is simulated.
This led to further investigating the possibility of gel pads as a reflective medium. Thus, a feasibility study was conducted to produce prototype gel pads compliant with the simulation model. Setting up decent production techniques is challenging, the optical properties of the gel pads like transmission, refractive index, verification of the simulated model could not be tested.
In this work, we investigated two different strategies. We started with the production of standalone gel pads, i. e. casting the gel in a separate mold, curing it, removing the gel pad from the mold, and assembling it with the PMT in the module. The second method is the so-called 'in-situ-pouring' in which the gel is poured into a mold assembled with the PMT and placed in its final position in the pressure vessel. After curing, the mold is removed, and the PMT is connected to the holding structure. No separate gel pad is created in this process. This procedure has some advantages: several steps are removed in the production, reducing complexity, and can decrease overall error-proneness. However, exchanging a failed PMT is significantly harder as another gel pad needs to be cured inside the otherwise already fully assembled module for every exchange. Hybrid approaches like casting the gel in a mold in the optical module and later inserting the PMT are also possible but have not been investigated in this work.

4.1 GELS

The established solution to optical couple the PMT to the pressure vessel is to use a transparent silicone-based optical gel with a refractive index similar to glass. In general, gels, which are considered for this task, belong to the category of two-part room-temperature-vulcanizing silicones (RTV-2) as called by Wacker[63] one of the major manufacturers for such silicon gels. As the name suggests, these silicone rubbers consist of two components: liquid as long as separated and cured when mixed. The curing time depends considerably on the temperature. For room temperature it is in the order of 24 h which decreases to several minutes for higher temperatures (15 min at 100 °C in case of SilGel 612[54]).
These gels are commonly used for a vast field of applications, including household applications, sealing of electronic components, photovoltaics, and optoelectronics[63] with significant differences in their physical properties. For an

optical gel to be considered, it must fulfill some requirements: Excellent transmittance in the optical range and a refractive index similar to borosilicate glass. Additionally, when cured, the gel pad's surface must be tack-free so the gel pad can be separated from the mold without being damaged. Lastly, the hardness of the gel pad has an important role. Too hard results in the gel pad no longer adapting well to unevennesses in the glass and the PMT surfaces. If the hardness is too low, the gel pad will hardly release well from the mold and form waves on the surface. For many gels, the hardness is dependent on the mixing ratio of the two components of the gel. Increasing the ratio towards the crosslinker, one of the two components of the gel increases the hardness of the gel and subsequently reduces the tackiness of the surface. In this work, four different gels have been tested:

WACKER SILGEL 612: This gel is used in the optical modules of KM3NeT, and it was used in the modules of STRAW and STRAW-b experiments developed by this group. Due to the experiences gathered in the development of the latter two experiments, we started the production of the gel pad prototypes with this gel. After mixing the two components, it has a medium viscosity of 1000 mPa · s and it vulcanizes to a very soft, sticky silicone gel[54]. The inherent tackiness and very soft nature of the cured gels surface were why we increased the mixing ratio of component A to component B to 1.5:1 (default is 1:1). This is the maximum Wacker recommends. The expected increase in hardness and reduced tackiness was observed. However, the effect was not significant enough. As a consequence, we decided to test different surface coatings to reduce the tackiness further (for details, see Section 4.3) and other gels with different nominal levels of hardness.

WACKER ELASTOSIL RT 601: Addition-curing two-part silicone rubber from Wacker. It features a very transparent appearance similar to Silgel 612 but with a lower viscosity of 3500 mPa · s when the two components are mixed. In contrast to the Silgel 612, it cures into a stiffer gel with a designated Shore A hardness of 45. Curing time is similar to Silgel 612 with 24 h for room temperature and 10 min for 100 °C[64]. In particular attractive for use was that Wacker recommended this gel as a coating for the Silgel 612 to achieve tack-free surfaces.

WACKER ELASTOSIL RT 604: This gel is, according to the datasheet, very similar to the Elastosil RT 601 where the most prominent differences are the higher viscosity of 800 mPa · s and the lower Shore A hardness of 25. It was mainly considered due to its hardness between the hard Elastosil RT 601 and the very soft Silgel 612.

DOW SYLGARD 184: A collaborating University of Alberta recommended this gel. They produced similar gel pads for a different experiment with this gel. It features comparable physical and optical properties as the gels mentioned above. Its hardness is comparable to the Elastosil RT 601 with a Shore A hardness of 43. Hence it belongs to the harder gels tested in this experiment. Additionally, its curing time is significantly increased to 48 h at room temperature and up to 35 min at 100 °C. Due to the longer curing time, this gel was only tested with accelerated heat curing.

4.2 MOLDS

The mold is the hollow container in which the gel is poured. It is formed as a negative of the volume between the glass sphere, the PMT, and the reflector cone and features two threaded G1/4 holes on the side of the cone. Two appropriate fittings with attached tubes are screwed into the threads acting as an inlet for the gel and an outlet for the air. In the first version of the mold, the placement of the molds was relatively close. In some cases, this resulted in trapped air bubbles in the gel pads. An image of a produced gel pad with such a trapped air bubble is depicted in Figure 4.4b. Consequently, in the second version of the molds, the placement of the inlets was changed to opposing sides, guaranteeing that the gel inlet is always at the lowest and the air outlet at the highest point. Figure 4.2a illustrates the working principle of the second mold.

FIRST VERSION OF THE MOLD The first version consisted of two parts. The *upper* part is shaped to resemble the outer glass sphere, and the *lower* part is designed to match the shape of the PMT and the reflective cone. The opening angle of the cone was not finalized at the time of the production of the molds. Therefore a preliminary angle of 50° was chosen as it fits is in the range of those used in KM3NeT, the mDOM, and the LOM. As the focus of this feasibility study was on the mechanical difficulties, the exact opening angle is not decisive. An additional mold can be produced with the final opening angle for an in-depth characterization of the optical properties and the simulation.
The two parts were sealed with an O-Ring between them and held in place by eight M3 screws distributed evenly on an outer ring. Image in Figure 4.1a show the manufactured parts and Figure 4.1b the assembled molds filled with optical gel. As stated, the inherent tackiness of the Wacker Silgel 612 was one of our primary concerns when performing the first round of tests. Therefore we wanted to test whether or not different materials of the molds affect the separation process of the gel pad from the mold. Thus we produced one mold from aluminum and one from polyoxymethylene (POM). Both materials can be manufactured with a very smooth surface, which was expected to improve the separation. The two G1/4 threads were drilled perpendicular to the cone surface in which matching fittings were screwed in with tubes attached for pouring in the gel and releasing the air. For the first version, no particular position was chosen for the in- and outlet, resulting in them being close to each other.

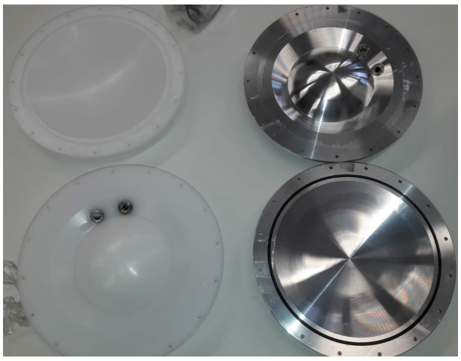

(a) Image of the manufactured parts of the first version of the mold. The left mold is the POM version and the right one is made out of aluminium.

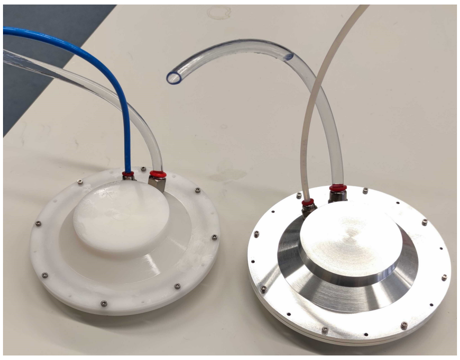

(b) The same molds but closed and filled with optical gel during the curing process.

Figure 4.1: Images of the manufactured first version of the molds.

SECOND VERSION OF THE MOLD The second version of the mold included some changes in contrast to the first version. Most prominently, we changed the closing mechanism of the mold. In the first version, the two parts were screwed together with eight screws. However, the (dis-)assembly process is quite time-consuming. Thus the second version consisted of three individual pieces. The *base* (middle one in Figure 4.2b) is the negative of the PMT surface and the cone. It featured redesigned connectors for the gel and the air. The connectors had a 90° angle between the thread and the opening to the cavity. This allowed an independent design of the connectors at the opening. Eventually, the cross-section of the in- and outlet at the cavity shrunk compared to the cross-section of the G1/4 threads. The latter is needed for the fittings and led directly into the cavity in the first iteration of the molds. This reduced cross-section is beneficial as the inlets naturally produce small bulges in the gel pad which cannot be eliminated (see images of cured gel pads in Section 4.4.2 and Section 4.5.2).

The *top* parts inner side is shaped to resemble the glass sphere. It houses the O-Ring, which seals the mold when assembled, and four additional M3 through holes. The remaining part is the *cap*, featuring a thread on the inner sides. Its purpose is to produce a tight seal when the base and the top are combined. Assembling and disassembling works as follows:

The top part is inserted into the base creating the cavity, which will later be filled with the optical gel. After that, the cap is screwed onto the sides, holding the top in place, creating a tight seal. When disassembling, the cap is unscrewed, and four matching screws are screwed in the top to lift it out from the base. It was found that the cured gel pad always sticks to the base because the base features very sharp and convex edges where the cone and the PMT shape are meeting, thus creating much more friction compared to the inherently uniform and only slightly curved surface of the top part. Eventually, the cured gel pad is carefully peeled off the base.

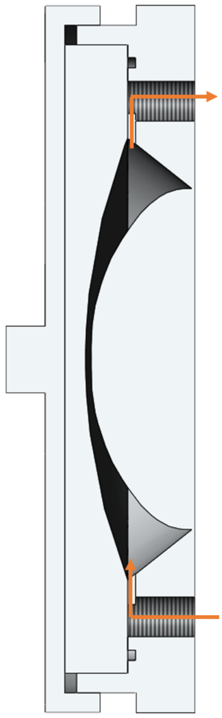

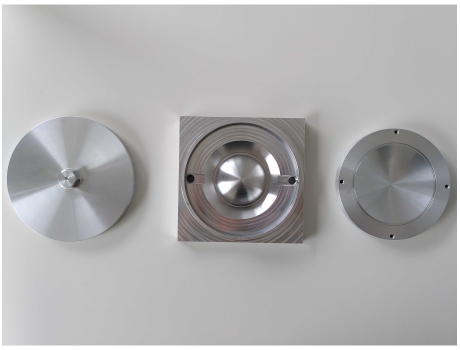

(b) The individual parts of the mold

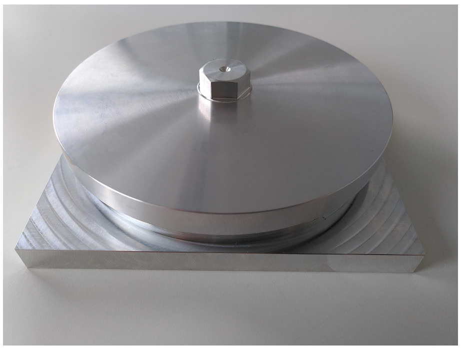

(a) Illustration of the working principle

(c) Image of the assembled mold

Figure 4.2: Illustration of the working principle and images of the parts of the second version of the mold

The surfaces of the cavity were, in addition, mechanically polished. It naturally leads to a more polished cone on the gel pad, improving reflectivity. This decreases the friction allowing for easier separation of the gel pad from the mold.

IN-SITU POURING MOLD In contrast to the previous two molds used for the standalone gel pads, this mold was created for in-situ pouring. The mold consisted of only one piece as this procedure uses the surfaces of the PMT and the pressure vessel directly to create a sealed cavity which is achieved by pressing the mold firmly against the glass sphere and holding the inserted PMT in place via two o-rings and a 3D printed spacer, that connects the PMT to the holding frame (details are illustrated in Figure 4.3). The pouring procedure is described in more detail in Section 4.5.1.
As in the second version of the standalone mold, the inlets are placed on opposite sides and perpendicular to the upper surface. The upper ports are G1/4 threads for the fittings, which tapers towards its end to reduce the cross-section.

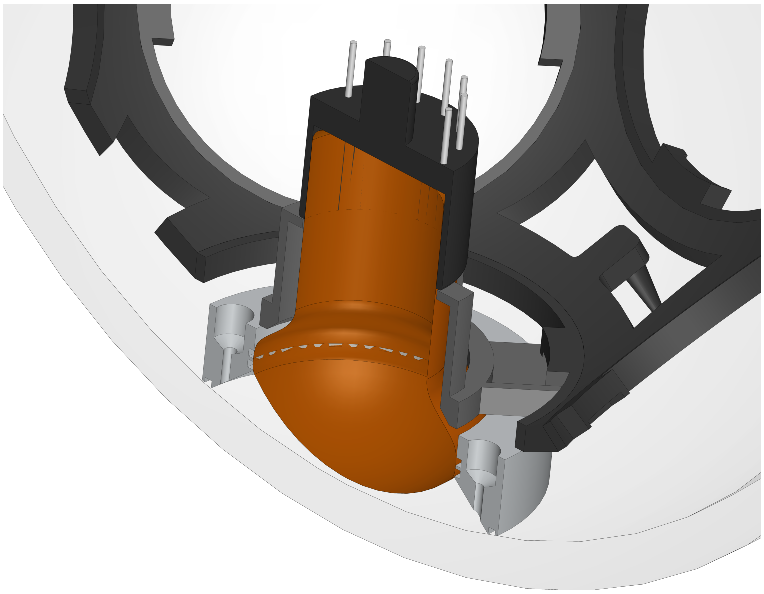

Figure 4.3: Sectional view of the mold assembled with the PMT and the holding frame in SolidWorks. The mold is colored light grey the mold, the 3d printed spacer in grey, and the holding frame in dark grey. The PMT is colored orange. The necessary O-rings and fittings are not depicted.

4.3 COATINGS

The tackiness of the SilGel 612 candidate was one critical problem during the thesis. Out of this, we tested the effect of different coatings on the removability if the gel pad after curing. The coating materials were applied by carefully coating the inner surface of the base and the top parts evenly. By this, a thin layer formed.
We conducted the first round of tests with a variety of materials such as *WD40*, a widely used lubricant, a mix of standard liquid *soap* and tap water and *silicon grease*. Additionally, we increased the ratio of component A vs. B of the optical gel beyond its maximum ratio of $1.5 : 1$ up to $2 : 1$. However, the manufacturer of the gels could not guarantee the long-term stability of the optical properties of the gel, which is an essential requirement for optical modules of P-ONE. Albeit then they recommended the Elastosil RT 601 as a coating for the Sigel 612 for tack-free surfaces.

4.4 STANDALONE GEL PADS

In this approach, the goal was to produce separate gel pads by pouring silicone gel into a mold, letting it cure, and removing it from the mold. Afterward, the gel pad is inserted into the glass sphere and the PMT in the gel pad. The PMT is eventually secured by the holding frame. Here, some problems needed to be tackled:
The SilGel 612 cures into a soft, tacky mixture. Hence we tested different

coatings to reduce the tackiness. Additionally, trapped air bubbles were the most dominant source of setbacks for us. They appeared in two different steps of the procedure: When pouring the gel in the mold and when integrating the gel pad in the module.

4.4.1 PROCEDURE

All tests were performed according to the following procedure to guarantee comparability between the trials. Disposable Nitrile gloves were worn in every step to prevent contamination of the materials:

1. All mold parts were thoroughly cleaned with isopropanol of residues from previous trials.

2. The two components were poured into a plastic cup one after another by weight using a precise scale, e. g. for a ratio of 1.5 : 1 150 g of component A and 100 g of component B were poured. The silicone gel was then mixed with a spatula for at least 2 min to ensure optimal homogeneity. After mixing, a vacuum chamber degassed the gel mixture to a pressure of 200 mbar until air bubbles were not forming anymore. This took no longer than 5 min to 10 min. If the trial includes a coating with another gel, these steps are repeated for the coating gel.

3. Next, the mold was assembled and sealed. If foreseen, we evenly applied a thin layer of coating on the inner surfaces of the pieces. We tested different application strategies like brushes, the aforementioned spatula, cotton swabs, but we found that applying by hand yielded the best and most consistent results. Additionally, tubes were connected to the fittings, which were in turn screwed into the G1/4 threads of the mold.

4. After finishing the assembly, the gel was poured into a large syringe (>200 ml), which was connected to one end of the tubes. The gel was gently pushed into the mold until it started to appear in the air outlet tube.

5. The syringe was then disconnected from the tube, and special care needed to be taken that the gel did not overflow. If this test included heat curing, the mold was placed in a preheated oven for the desired amount of time; else, it was left at room temperature for at least 24 h to allow for complete curing.

6. In the last step, the mold was disassembled. In the first iteration of the mold, this included unscrewing the eight M3 screws and lifting the *upper* piece of. Due to the higher friction, the gel pad always stuck to the *lower* part, from which the gel pad was gently peeled of.
   For the second version, the *cap* was unscrewed and four M6 screws screwed into the threads of the *top* piece, providing the necessary force to lift it from the *bottom* part. Afterward, the gel pad is separated from

the *bottom* by peeling it slowly of, and great care needed to be taken not to touch any part except the edge to avoid contamination.

4.4.2 CONDUCTED TESTS AND RESULTS

FIRST VERSION OF THE MOLDS We started the trials with the SilGel 612 in a mixing ratio of 1.5:1 as some of this gel from the pathfinder experiments were still available. With this, we produced a reference gel pad with no treatment applied to the molds. As expected, we had significant difficulties when we tried to separate the two parts of the mold due to the anticipated stickiness of the gel pad. We were forced to use screwdrivers to produce enough leverage to separate the two molds. To ease this process in the upcoming tests, we installed four additional M6 threads on the outer ring of one of the parts so we could exert enough force on the other piece of the mold to separate them. Figure 4.4a gives impressions of this process and Figure 4.1b shows an image of the two molds in the curing stage.

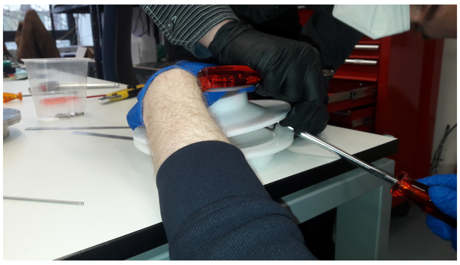

(a) Opening the mold of the gel pad with untreated surfaces using screwdrivers

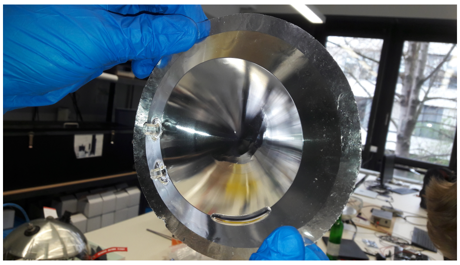

(b) Gel pad with a dominant airbubble.

Figure 4.4: Images of the production of the reference gel pad.

After this, we tested different interface treatments as discussed in Section 4.3. Overall all three coatings gave similar results with no significant improvement in removing the gel pad from the mold compared to the other coatings. Slight advantages were observed for the treatment with WD40, making it the best of all three treatments. The soap-water mixture was particularly noticeable. Not because the corresponding gel pad was easy or difficult to remove from the mold, but because it formed residues on the surfaces of the cured gel pad. This is likely caused by tap water as a dilutant of the soap. The vacuum grease was the only coating that failed. We were forced to rip the gel pad apart to separate the two parts of the molds. See Figure 4.5b for impressions of this failed gel pad. Noteworthy is that this only happened for the aluminum mold and not the POM mold. The separation from the POM mold was comparable to the previous coatings.
Additionally to the different coatings, we tested how an increased ratio beyond the recommended maximum of the two components affected the separation procedure.

COATING / RATIO	RESULT (POM)	RESULT (ALUMINIUM)
WD40 (1.5:1)	easier	easier
Soap-water mixture (1.5:1)	residues on surfaces	residues on surfaces
vacuum grease (1.5:1)	comparable	FAILED
ratio 2:1 (no coating)	best to remove	best to remove

Table 4.1: Results from the trials with different surface coatings. RESULT denotes how easy the separation of the gel pad from the mold was relative to the reference gel pad with no treatment and a mixing ratio of 1.5:1 or if any special occurrences happened.

Table 4.1 summarizes the results from this first round of tests. No coating significantly improved the separation process. Only the WD40 gave slightly increased results. However, the increased ratio yielded the best result from all tests with a noticeably harder gel pad, which was the easiest to remove from the mold. We also did not observe differences between the POM and the aluminum mold (apart from the destroyed gel pad from the vacuum grease coating).

(a) Image of the removal of a gel pad from the POM mold.

(b) Image of the separation attempt of the failed gel pad with a coating of vacuum grease in the aluminium mold

Figure 4.5: Images of the separation of different gel pads with different treatments. Refer to the text for additional information.

However, we did notice the little patterns on the surfaces of the gel pad induced by the unevenness of the aluminum and POM surfaces. And although we did not test it at this stage, it is evident that a smoother surface at the cone side of the gel pad increases the reflectivity, which can be achieved by polishing the surface of the mold. Which, in return, is much easier for an aluminum mold than for a POM mold. This advantage and the similarity in the results of the tests were the main arguments for opting only for an aluminum mold in the second round of tests.
During these tests, we observed two main regions where air bubbles formed. Either they formed at the in- and outlets which are caused by the fittings sticking into the mold and therefore preventing some air from escaping, or

they formed in some cases at the edge between the PMT and the cone side (see Figure 4.4b for one such case) which is caused by a wrong placement of the mold in the pouring stage.

SECOND VERSION THE MOLD In the second round, we used the improved version of the mold described in Section 4.2 and we refrained from performing additional tests with the already tested coating materials as we did not expect a different result with the new mold. Instead, we decided to test other optical gels both as a replacement for the SilGel 612 and as a coating, as the latter was the recommendation from Wacker after consulting them.
We started with the DOW Sylgard 184 with the recommended mixing ratio of 10:1 and no additional coating applied to the mold and heat-cured it for $\approx 1\,\mathrm{h}$ at $100\,°\mathrm{C}$. This is roughly two times the recommendation of DOW, which is needed to account for the warm-up phase of the aluminum mold. The resulting gel pad did not exhibit tack and was overall the easiest to remove. However, its hardness exceeded the one of the SilGel 612 with the increased mixing ratio to a point where we felt that the gel pad was too hard to work with it. Which results in the gel pad not being able to adapt to slight variations in the geometry of e. g. the PMTs.
Next, we tested the Elastosil RT 604 from Wacker without an additional coating. We did not observe any peculiarities compared to the other tests. The resulting gel pad was harder than the reference gel pad but more challenging to remove than other configurations. Following, we tested the combination of the SilGel 612 as the primary optical gel and the Elastosil RT 601 as a coating. This combination yielded by far the best results of all trials, combining the advantages of both gels. On one side, the gel pad is comparably soft (due to the ratio of 1.5:1) and can therefore adapt to changes in the geometry. On the other side, it has a tack-free surface due to the coating with the Elastosil RT 601, resulting in an uncomplicated separation procedure. The refined version of the mold also eliminated the problem with trapped air bubbles. We performed multiple tests with this combination, resulting in good reproducibility. In one instance, the gel pad tore at the PMT-cone edge since the angle at this edge has a very sharp angle; this can be seen in Figure 4.6a.
Best results were observed when the gel was heat-cured at $100\,°\mathrm{C}$ for $\approx 30\,\mathrm{min}$ which is again a factor two larger than the recommended curing time at this temperature. Shorter curing times resulted in a not fully cured gel pad, and significantly longer times ($\approx 100\,\mathrm{min}$) resulted in a gel pad that lost its transparency and appeared instead brownish, suggesting that the gel pad got damaged due to long heat exposure.

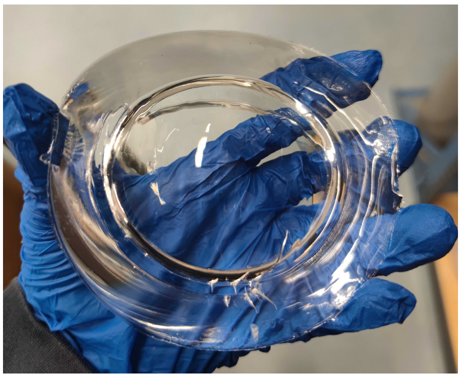

(a) A gelpad that is torn in a few places.

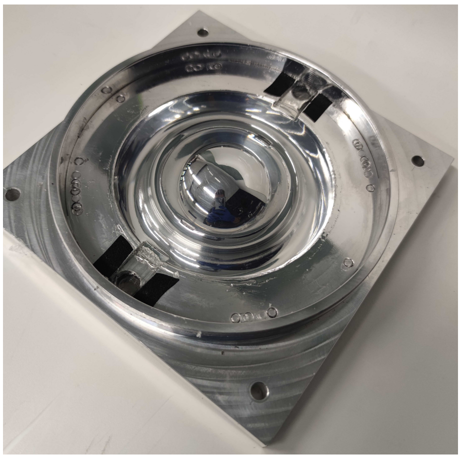

(b) A flawless gel pad which is not removed from the the base part.

Figure 4.6: Images of gel pads produced with the SilGel 612 and the Elastosil RT 601 as a coating.

Table 4.2 summarizes the results from the second round of tests. From the tests, we concluded that a combination of SilGel 612 (with a mixing ratio of 1.5:1) and a coating with Elastosil RT 601 (with the default ratio of 9:1) yielded the best results and is, therefore, the best candidate for the optical modules.

COATING / RATIO	RESULT	NOTABLE
DOW Sylgard 184	easy	too hard for use
Elastosil RT 604	comparable	nothing
SilGel 612 + Elastosil RT 601	easiest	recommendation

Table 4.2: Results from the second round of trials with different optical gels and coatings. RESULT denotes how easy the separation of the gel pad from the mold was relative to the reference gel pad with no treatment and a mixing ratio of 1.5:1.

4.4.3 INTEGRATION INTO THE MODULE

After the aforementioned tests, gel pads that are easy to remove and free from air bubbles could be reliably produced. The following tests focused on integrating these gel pads in the optical module. There are two major obstacles in this process: First, the interfaces between the gel pad and the glass sphere, and respectively the gel pad and the PMT must be free of air bubbles. Second, the positioning of the PMT and the gel pad in the glass sphere must be reliable and precise. However as this depends on the final configuration of the instruments, the focus was on the reduction of air bubbles at the interface. Nonetheless, another aspect was the streamlining of procedures to reduce the susceptibility to errors, also in regard to the production of several modules.

The easiest approach to the assembly is to place the unmodified gel pad in the glass sphere and stick the PMT into the gel pad. But due to the inherent geometric uncertainty of the PMT and the unevenness of the surface of the gel pad and the glass sphere, this naturally yields to trapped air in virtually any test we performed. Example images for this approach are provided in the following figure.

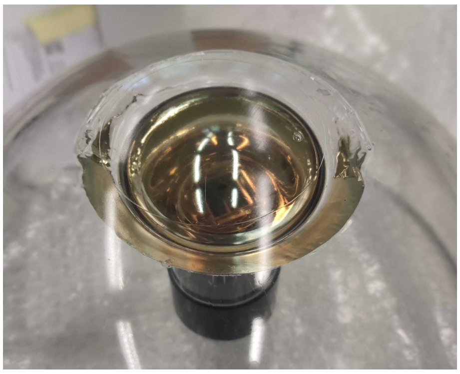

(a) Nearly free of air bubbles. Impurities on the left and right side of the reflective cone are due to a test, where additional gel was applied on the outer cone in an attempt to smooth out the surface.

(b) Some airbubbles visible on the right side. Dominant unevenness on the upper part of the gel pad because the curing time was to short and some gel did not fully cure at this region.

Figure 4.7: Gel pads in a glass sphere with a PMT inserted. No coatings were applied on the *glass sphere - gel pad* and *gel pad - PMT* interfaces. On the cone side facing towards the camera the total internal reflection can be seen (brownish/orange color due to reflection of photons from the photocathode)

In the next attempt, we tested if coating the interfaces with different materials can improve the results. We tested the SilGel 612, the Elastosil RT 601, and optical grease in this course. All gel pads were produced using the previous chapter's recommendation. Different techniques for applying the coatings were investigated, which can be divided into two categories:

'BLOB' TECHNIQUE The first was to apply a small 'blob' of optical gel in the middle of the hollow formed by the glass sphere or the side of the gel pad where the PMT is attached. Then the gel pad is pressed on this blob (and the PMT on the blob in the gel pad), and the gel is pushed outwards. With this approach, we observed some drawbacks. Most importantly, the amount of gel was in all situations too much and therefore leaked out. However, reducing the amount of coating gel would result in parts of the interface not covered with gel. Figure 4.8a shows an image of an assembled gel pad using this method. The leaked gel is visible on the edges of the gel pads interfaces. This excess gel made accurate positioning much more complicated and eliminated much of the total internal reflection at the cone side of the PMT. Therefore this approach was disregarded, and we focused on the second technique.

THIN COATING This aims to apply an even and thin coat layer on the gel pad. The application process was tested with the spatulas used for mixing the optical gel, by hand and cotton swabs. Similar to the coating application on the mold, the tight-fitting gloves yielded the most consistent result. We tested optical grease, SilGel 612, and Elastosil RT 601/604 as a coating material.

eventually, we tested if degassing the entire structure helped to eliminate the remaining air bubbles. To do this, we assembled everything such that the PMT was in the Center of the hemisphere and pointed upwards. The hemisphere was placed on an aluminum plate with a rubber mat and the PMT on a small platform connected to the aluminum plate via springs to exert the necessary force to keep the gel pad and PMT in place. Finally, a tube attached to a fitting screwed in the aluminum plate was connected to the pump.

(a) Assembly using the blob-method as a coating. Overflowing gel is visible on the glass sphere and the reflector side of the gel pad.

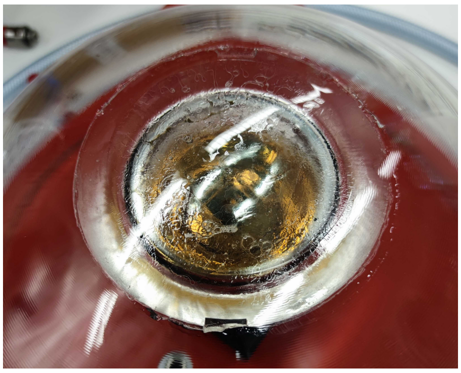

(b) Assembly using optical grease as a thin layer of coat. Many bubbles are present, due to the very low viscosity of the optical grease which does not allow trapped air to escape during degassing.

Figure 4.8: Images of assembled gel pads using the 'blob' technique and optical grease as thin layered coating.

Figure 4.8b shows a representative image of the result when using optical grease as the coating material. The most significant problem was the extremely low viscosity of the grease, which prevented trapped air bubbles from escaping during the degassing process and yielded the worst result.
All the optical gels yielded comparable results in processability and amount of air bubbles, with slight advantages for the SilGel 612. In contrast to inserting the PMT perpendicular, inserting the gel pad successively from one side to the other decreased the amount of trapped air. Performing multiple cycles of degassing did not decrease the number of air bubbles. Images in Figure 4.9 show an assembly using a thin layer of SilGel 612 as a coating. Except for one large air bubble on the left side no trapped air remains. The PMT is

perfectly coupled to the glass (see Figure 4.9a) and total internal reflection works exceptionally well (see Figure 4.9b).

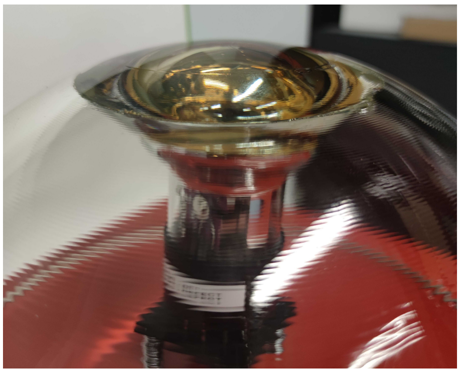

(a) Side view of an assembly using a thin layer of SilGel 612 as a coating. No air bubbles visible.

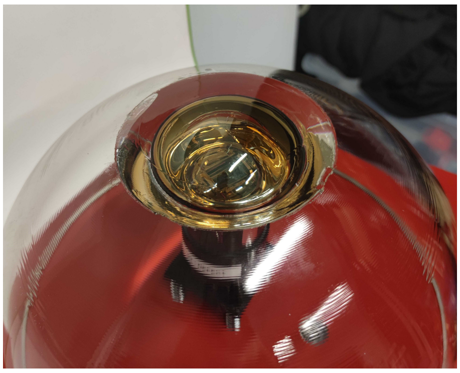

(b) Same gel pad as in c). Perfect total internal reflection visible. One air bubble on the left side is visible.

Figure 4.9: Images of assembled gel pads using SilGel 612 as a coating.

In summary coating, the interface with an evenly thin layer yielded better results. All tested optical gels yielded similar results. Attaching the pad from one side successively to the other decreased the amount of trapped air compared to inserting it perpendicular and applying force to push out the air. Degassing the whole hemisphere further decreased the amount of trapped air. Performing multiple cycles of degassing did not yield additional improvements.

Although we could produce a gel pad and integrate it into an optical module without trapping air with this procedure, some concerns and uncertainties remain. Most notably, this procedure involves many steps, each increasing the likelihood of errors and ultimately reducing the overall reliability of the process. Although this work is still in very early development phases, these issues are generally valid for all tested approaches. Therefore it raises the question of how well it can be improved and scaled to fulfill the qualitative standards of a neutrino telescope.

4.5 IN-SITU POURING

Due to the concerns presented at the end of the last chapter, we decided to test a substantially different approach called 'in-situ pouring'. This approach promises to address these difficulties mainly because it has inherently fewer steps compared to the production of standalone gel pads. Although this approach seems promising, only a small feasibility study was conducted in the scope of this thesis due to time constraints. Therefore the procedure and results presented in the following are merely the first steps and are not yet conclusive.

4.5.1 PROCEDURE

This method revolves around the idea of entirely skipping the process of producing separate gel pads by instead pouring the optical gel directly into the cavity between the glass sphere and the PMT. Hence, we designed a third mold which is described in more detail in the last paragraph of Section 4.2. In this process, the conical side of the mold is coated with a thin layer of Elastosil RT 601 (analogous to the preparation of the molds for the standalone gel pads) and inserted through the holding frame at the appropriate position on the glass hemisphere. In the next step, the PMT is inserted into the mold. To keep the PMT in place, the base of the PMT rests on a 3D printed plastic piece which in turn rests on the mold and is connected to the holding frame(highlighted in grey in Figure 4.3). Due to the connection to the holding frame, this ensures proper positioning of the mold and the PMT.
Next, two tubes are connected to the mold via fittings screwed in the mold. One tube leads to the reservoir containing the liquid optical gel. Since the combination of SilGel 612 and Elastosil RT 601 has proven successful, we continued using it. The other tube leads into an overflow container. This container is airtightly sealed, and a smaller reservoir is placed inside it to which the tube is connected. Its purpose is to collect excess gel. The overflow container leads a third tube out, which is connected to a vacuum pump. The overflow container ensures that no excess gel gets into the pump.
The system gets degassed until some gel exits the mold, indicating that the mold is filled with gel. Figure 4.10 shows a sketch of the working principle.

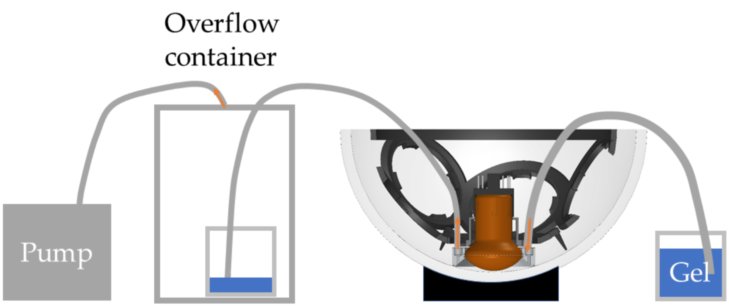

Figure 4.10: Sketch of the procedure of the in situ pouring. The gel is drawn into the assembled mold and exits through an outlet into a reservoir in an overflow container. This container is connected to an air pump generating the vacuum.

4.5.2 RESULTS AND OUTLOOK

In the performed tests, we found that the general principle of this test setup works reliably. The assembly with the 3D printed plastic piece connecting the PMT and the mold to the holding frame and keeping them in place works well. Nevertheless, the plastic piece needs to be improved, as its arms were prone to breaking when pulled over the thicker PMT base. We created a vacuum of $\approx 500\,\mathrm{mbar}$ in the degassing phase, which was enough to draw the gel in at a steady pace. The main issue we encountered was that the O-ring, which seals the edge between the glass sphere and the mold was leaking, most likely at the glued joint. This results in air drawn in from this point, subsequently preventing the mold from filling with optical gel. This will be addressed in further tests. Figure 4.11 presents a gel pad resulting from these tests. The huge air bubble, resulting from the leakage, is visible on the left side of the gel pad.

Figure 4.11: Image of a gel pad produced with the in-situ pouring. A large air bubble resulting from a leaking joint in an O-ring is visible on the left side.

In the next steps, we will investigate the O-ring leaking and improve the assembly process to make it easier overall. Additionally, the last open problem of this procedure that needs to be solved is how to shut off the gel once the mold is filled.

4.6 LONG-TERM DELAMINATION TEST

In the current design of the optical module, the holding structure will exert force on the PMT and the gel pad (e. g. in a spring-loaded configuration) to keep them in place and account for different thermal expansion of the materials. At lower pressure and temperatures, the constant force can pose the risk of delamination of the gel pad. To investigate this process, we performed a long-term test. We assembled a gel pad with a PMT in a glass hemisphere in this test. We did not use any coating in the assembling process to not distort the result. The mold was designed for a 13" sphere, which was eventually used. As with the other tests, this does not impact the result since the difference for this work lies only in the slightly changed curvature of the sphere. To emulate the force, we 3D printed a holding frame placed on the PMT, vertically aligned it throughout the test, and placed a 2.5 kg copper cylinder in this frame. The resulting force is at least an order of magnitude larger than the expected force exerted from a spring-loaded configuration. Figure 4.12a depicts a sectional view from SolidWorks of this setup.

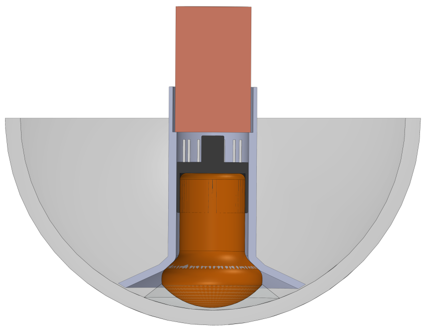

(a) Sectional view of the test setup as designed in SolidWorks.

(b) Image of the test setup after six month. No delamination visible.

Figure 4.12: Sectional sketch (left) and result after six month (right) of the long-term delamination test

After six months, we did not observe any sign of delamination of the gel pad in the test setup (shown in Figure 4.12b). Should the in-situ pouring be identified as the preferred production technique, this test could be repeated as it differs significantly from the standalone gel pad production.

4.7 CONCLUSION

This chapter presented two techniques to produce a transparent reflective component. In the first method, the standalone gel pad production, we produced individual gel pads by pouring optical gel in a mold and assembled the gel pad with a PMT in the glass hemisphere. In this course, we tested different optical gels and different materials as a coating for the mold to decrease adhesiveness. We found that SilGel 612 in a mixing ratio of 1.5:1 with a coating of Elastosil RT 601 (both produced by Wacker) yielded the best results. We consistently produced gel pads free of trapped air with the presented method. A thin layer of optical gel on the gel pad decreased the trapped air in the integration process. Degassing the whole hemisphere further improved the result. Nevertheless, due to the many steps involved in this process, it is questionable if this approach is scalable to mass production required for a neutrino telescope while maintaining a consistently good result.
Hence, we tested the technique of in-situ pouring the optical gel into the assembled module. This method draws the optical gel in the degassed cavity formed by the PMT, mold, and glass sphere. Some issues still need to be solved: Namely, we discovered that the O-ring, sealing the mold, was leaking at the glued joint; hence the gel could not fill the mold. Additionally, the molds positioning and the PMT need to be improved to work more reliably. The method itself needs to be refined to maintain equilibrium when the mold is filled so the gel can cure. The issues can be accounted to the very early stages of the development of this stage. Still, this process seems promising and further tests will be conducted to solve these issues.
Finally, we tested if delamination poses an issue. This can occur due to the force exerted on the gel pad. After a long-term test of six months, we did not observe any delamination.

5 CALIBRATION STATION

A remotely controllable and automated test bench, the calibration station, was developed in parallel to this work to characterize different PMT candidates and select a suitable candidate for P-ONE. This automatization reduces the effort of the characterization process for the expected volume of $\mathcal{O}(100)$ PMTs. Additionally, automatizing the process increases the reproducibility of the individual measurements and ensures quality standards.

To perform the measurements, the output of a pulsed laser is attenuated to the level of single photons, which are guided with optical fibers to the PMT. The PMT is fixed on a rotation stage, allowing for a rotation of it relative to the direction of the light.

Some of the key characteristics of a PMT, which are the dark rate, transit time spread (TTS), and voltage-dependent gain of the PMTs, have been measured in this calibration station. The dark rate is defined as the rate at which the PMT produces a signal without being exposed to a light source. This is mainly induced by the thermal electron emission of the cathode and the radioactive decay of ^{40}K in the borosilicate glass of the entrance window. The transit time denotes the time interval between the emission of the photoelectron and the appearance of the output pulse. Statistical fluctuations of the transit time arise when the photocathode is struck with several identical pulses. The width (either the FWHM or the standard deviation of a gaussian distribution) of the probability distribution of these fluctuations are called transit time spread[65, p. 51][66, p. 19]. The gain is a measure for the amplification of the single photoelectron through the dynode stages in the PMT, which depends on the voltage applied to the PMT. Additionally, two-dimensional scans of the photocathode area can be used to assess its uniformity. The following section will go into more detail about the individual components used in this setup.

5.1 COMPONENTS

The calibration station consists of the following components, also depicted in Figure 5.1:

DARK BOX The measurements are performed in a dark box that blocks efficiently surrounding light sources. As PMTs are very sensitive to single photons, ambient light would alter measurements and potentially damage the PMT.

LASER We use the PiL040-FC from NKT Photonics [67]. It consists of the laser and the laser control unit and can generate light pulses with a wavelength of 405(15) nm and a pulse width of less than 45 ps with a maximum rate of 40 MHz. The light is coupled into an optical fiber connected to an attenuator to substantially decrease the number of photons per pulse. After the attenuation, the optical fibers are split into two instances. One fiber is connected to a Powermeter to monitor the laser's output. The other fiber is split additionally. One is directed on the PMT, and the other can be connected to a reference photodiode.

PICOSCOPE To measure the output from the PMT, we used a PicoScope 6424E from pico Technology [68], which is a fast four-channel oscilloscope with a maximum resolution of 12 Bit and can be remotely controlled. The laser trigger is fed into the Picoscope to trigger the signal received from the PMT.

PICOAMPEREMETER/PHOTODIODE The second fiber in the dark box can be guided to the photodiode for reference measurement. A picoamperemeter reads out the signal.

CENTRAL COMPUTER The computer is the interface to the supplementary electronics and reads out the signals of the remotely controllable measurement devices.

ROTATION STAGE The contribution to the calibration station from this work was the rotation stage. It is described in more detail in the following section. But its general purpose is to reliably rotate the PMT about its two axes such that every point of the photocathode can be illuminated with the collimated laser light.

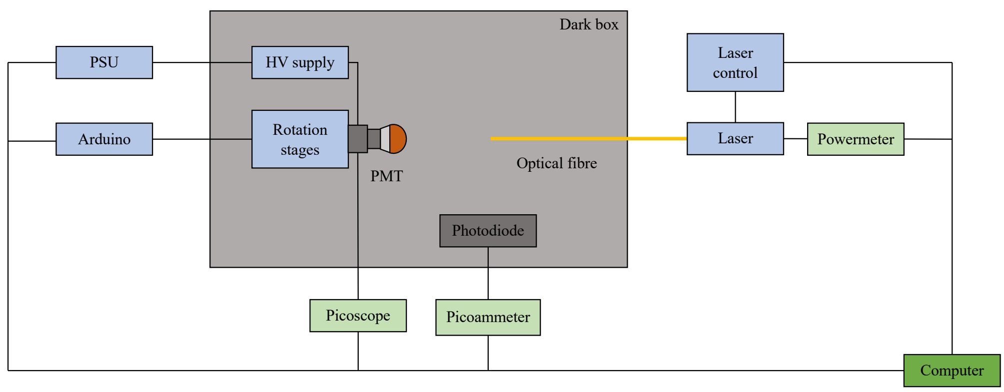

Figure 5.1: Sketch of the structure of the calibration station. The individual components are explained in the text. Courtesy of L. Winter

5.2 THE ROTATION STAGE

The photons are guided through an optical fiber and leave through the exposed FC/PC connector resulting in a collimated laser beam with a diameter of ≈ 3 mm on the surface of the photocathode of the PMT. However, the uniformity of the PMT over the whole photocathode is a parameter for comparison. Despite, potential influences of the geometry on the TTS require that all parts of the photocathode can be illuminated. To achieve this, two approaches are possible.: Either the laser is rotated (e. g. by mirrors), or the PMT is rotated. We decided on the latter approach in this test setup.
The rotation stage is driven by two stepper motors (RSA1 from Kurokesu [69]). Each of them rotates the PMT around one of its rotational axes. The stepper has an initial step angle of 1.8° per step, which was further reduced to 0.07° through microstepping. Additionally, the rotational speed can be adjusted between 12 RPM and 1 RPM with a standard speed of 0.67 RPM. Setting a larger speed introduces oscillations due to the system's acceleration, which reduces the positional accuracy of the system.
A primary concern was that the inherent magnetic field of the steppers might influence the response of the PMT as they are very sensitive to magnetic fields. Out of this, we put the motors as far away as possible in the design process. In the final design, both steppers were 20 cm away from the PMT. In this configuration, the magnetic field at the position of the PMT was comparable to the earth's magnetic field. We separated the lower stepper motor and the gear to achieve the distance and connected the two parts with a timing belt. The motor and the gear are connected to the optical table with two custom holding frames made from aluminum. The one for the gear features two slotted holes to fine-tune the timing belt length. A 3D printed spacer connects the first gear with the aluminum plate, to which the second stepper is connected. The cylindrical brackets are mounted to the gear of the second stepper in which the PMT is plugged.
Finally, we removed the Hall sensors, which were initially used for homing the steppers, as they introduced magnetic fields. We replaced them with infrared positioning sensors. These sensors host both the IR emitter and receiver and trigger when the detected light of the receiving diode exceeds a given threshold. This is achieved by an object (e. g. the aluminum plate or the vertical stepper) passing the sensor in short (order of a few centimeters, depending on the strength of the light emission) distances. The cylindrical holding brackets for the PMT have a small gap between them. The opening can be widened, a PMT inserted and fixed in position. The PMT is inserted such that the center of the radius defining the curvature of the photocathode is in the center of the horizontal rotation axis.

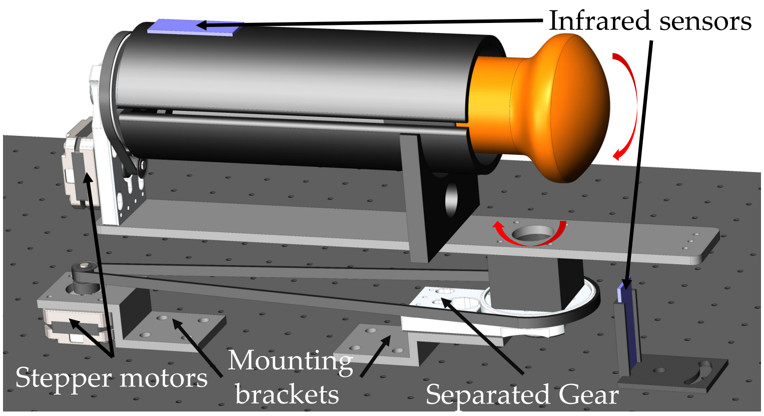

Figure 5.2: Drawing of the rotation stage in SolidWorks. A detailed description of the individual components is provided in the text.

5.3 SIMULATION OF GEL PADS IN THE CALIBRATION STATION

A primary purpose of the calibration station is to perform measurements of the standalone gel pads. Since the dark box is large enough to fit in a 17" hemisphere, also the in-situ pouring can be evaluated. These tests are critical to cross-check the geant4 simulation. However, the tests will be conducted in air instead of (sea) water. Out of this, the simulation needs to be altered:

First, we changed the world medium to air, and the glass sphere has been removed. Next, we changed the emitting sphere, such that the maximum theta angle of the emitted photons was 60°. The geometry changes imply that emitted photons cannot reach the gel pad or the PMT from larger angles. This has the additional benefit that the photon density on the emitting sphere is increased, resulting in a lower error with the same binning compared to the results in Chapter 3. Finally, we altered the center's position of the emitting sphere. Previously it has been in the center of the optical module. Now, it is at the center of the curvature defining the photocathode. As a result, we can simulate all possible directions of the PMT required for a full scan of the photocathode area in one single simulation. Consequently, we also changed the allowed opening angle of the emitted photons. In the previous simulation, it was defined such that all photons hit the optical module. For this simulation, we changed it to 0.001°. With this, the opening angle reflects the angle of the open end of the optical fiber.
In contrast to the previous simulation, where the absolute detection probability was required, it is now sufficient to specify the relative detection probability. We decided to normalize on the photons injected perpendicular to the entrance window.
In this simulation, we simulated a PMT with a gel pad and one without as reference. The gel pad had an opening angle of 50° to be compatible with the

angle of the produced gel pads. Figure 5.3 shows the result of this simulation. In this simulation, we took advantage of the rotational symmetry of the system and averaged over the azimuth angle.

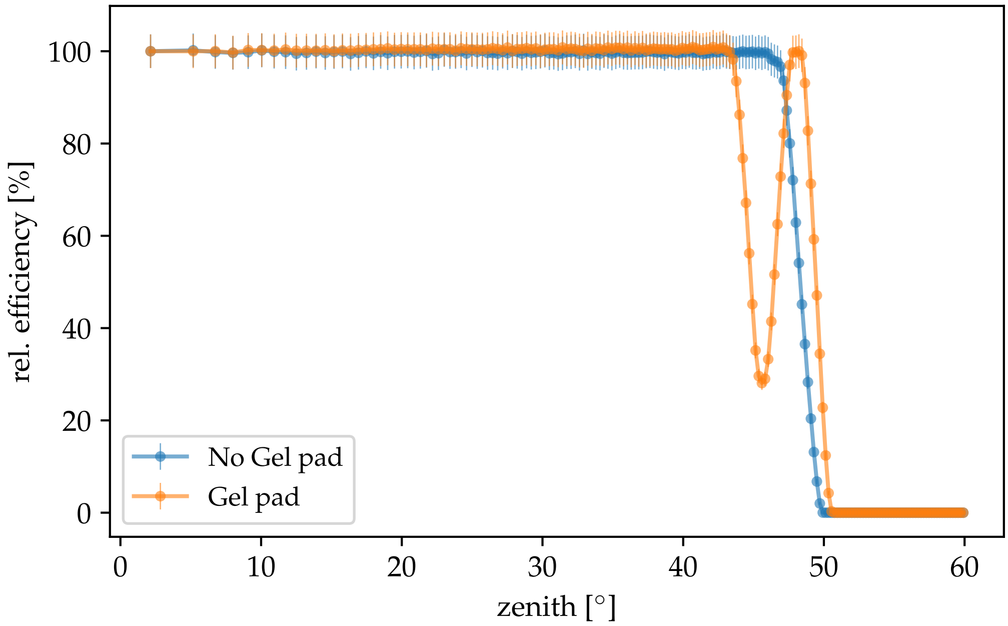

Figure 5.3: Relative detection efficiency from a simulated PMT with a gel pad with an opening angle of 50° and a bare PMT without a reflective component. 5×10^8 photons were simulated.

The detection efficiency stays approximately constant until an incidence angle of 43° for the gel pad and 47° for the simulation with the bare PMT. In the configuration without a gel pad, the relative detection efficiency drops rapidly to zero after this angle. This drop off happens because photons with a large angle of incidence do not reach the photocathode anymore, and no physical process like refraction can change their direction in this simulation.
The relative efficiency of a PMT with the gel pad dips sharply after the constant detection efficiency with its minimum at approximately 48° according to the simulation. After this minimum, the efficiency rises back to the reference value before dropping to zero due to the photons not hitting the photocathode anymore.
This dip can be explained by the following: Photons with a sufficient incidence angle are reflected on the conical side of the reflector. The angle relative to the normal of the conical side of the photons is large; hence also the angle of reflection. However, the point of refraction is so close to the PMT that the refracted photons hit only the glass and the housing of the PMT and not the photocathode since the photocathode is inside the glass housing. Figure 5.5 shows a sketch of this process.

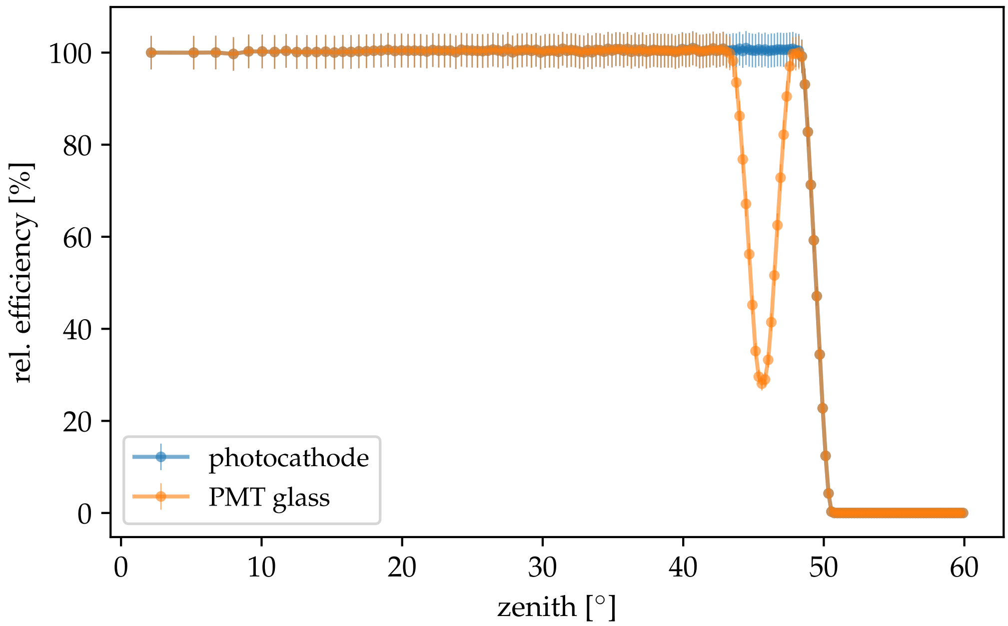

Figure 5.4: Result from a simulated PMT with a gel pad with 50°. With the photocathode as the sensitive volume and the glass housing as the sensitive area. 5×10^8 photons were simulated. Details are provided in the text.

When we changed the sensitive volume of the simulation from the photocathode to the PMT glass, this effect is gone, and the PMT shows a constant detection efficiency until a drop off (see Figure 5.4 for the result of this comparison). This drop-off appears for slightly larger angles of incidence than for a PMT without a gel pad. This effect can be attributed to the gel pad.

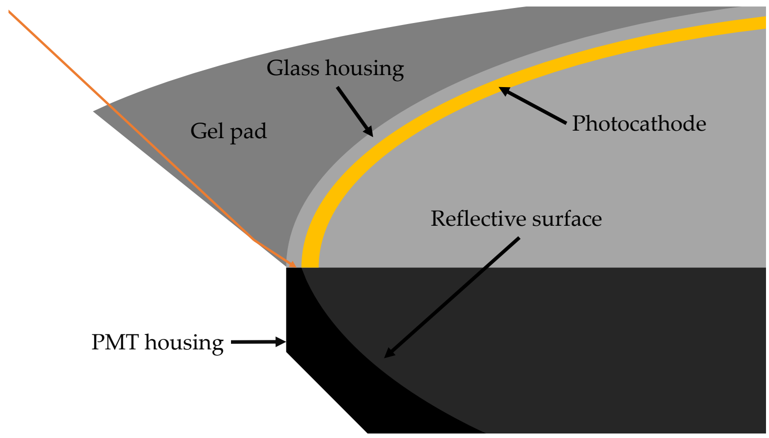

Figure 5.5: Sketch depicting the process causing the drop when simulating with the photocathode as the sensitive volume.

The next steps will be the mentioned tests in the calibration station to compare the results to the simulation. It remains to be tested if the dip we observed was due to inaccurate modeling of the PMT and if the simplified version describes the PMT results in a more accurate description.

Part III

THE SECOND PATHFINDER OF P-ONE: THE LIDAR

This part focuses on the LiDAR. An instrument designed to measure the attenuation and back-scattering length of the deep seawater at the Cascadia Basin site. It will consist of an introduce the LiDAR, a discussion of the laser direction scan, the simulation, and results of the first measurements. In the end, i will give an outlook on the next steps.

6 LIDAR

The last chapter will focus on the LiDAR. The LiDAR is one of five specialized instruments developed for the STRAW-b experiment, the second pathfinder mission to characterize the Cascadia Basin site west of Vancouver Island in Canada for the future neutrino detector P-ONE. STRAW-b consists of ten modules distributed on a 450 m long mooring line. The modules can be divided into two categories: *Standard modules* which deliver internal sensor data and otherwise are used to validate the deployment strategy and the mechanical design of the experiment and *specialized modules* which in addition host dedicated instruments to perform characterizations of the deployment site. The experiment has been successfully deployed in late 2020.
All modules consist of a 13 " spherical pressure vessel comparable to the candidates for the optical modules of P-ONE. The lower hemisphere houses the base electronics for power supply, data processing, communication, and the internal sensors. These sensors provide pressure, temperature, humidity, magnetic field, and acceleration data. The electronic components were optimized to occupy a minimal volume to provide enough room for the specialized instruments. From the ten modules deployed, four are standard modules. The remaining six modules consist of five modules equipped with specialized instruments and one additional module developed by a collaborating group:

PMT SPECTROMETER This instrument aims to measure the intensity and spectrum of the bioluminescence of deep-sea organisms. Eleven of the twelve PMTs are equipped with a different wavelength filter each. Lenses will focus the incoming light on the PMTs. They are mounted on a 3D printed frame aligning them to the same FoV by correcting for the refraction of the glass sphere. In addition, a camera is placed in the center of the PMTs and is switched on, when the PMTs detect a nearby bioluminescence flash.

MINI SPECTROMETER This instrument complements the PMT spectrometer's measurement of the bioluminescence spectrum. It uses five commercially available small factor spectrometers from Hamamatsu. Similar to the PMT spectrometer it hosts a camera that can be activated when a signal is measured.

MUON TRACKER The muon tracker is designed to perform measurements on the muon rate at Cascadia Basin. It utilizes two detection arrays separated by a certain distance. Each array is divided into 4 plastic scintillation tiles where the deposited energy of the muon is read out by SiPMs. The plastic scintillators are enclosed in Teflon and high reflective foil to minimize losses. Approximate directional information can be obtained in the time differences of correlated events in the separated scintillation tiles.

WAVELENGTH SHIFTING MODULE (WOM) The WOM was designed and developed by the Johannes Gutenberg University of Mainz, Germany. In contrast to the other modules, it is not using the standard module as a housing. It is optimized to detect UV light. The cylindrical pressure vessel made from quartz hosts a smaller cylinder coated with wavelength shifting paint. The incident UV photons are absorbed and re-emitted in the visible spectrum. The emitted photons are then guided to two PMTs.

LIDAR The goal of the LiDAR is to provide complementary measurements of the attenuation from STRAW and measure the backscattering length. Here, a laser emits short light pulses into the medium. From the amount and time information of the backscattered the optical properties of the water can be extracted. The instrument and its working principle will be introduced in more detail in the following section.

The distribution of the individual modules can be found in Figure 6.1a. Two identical LiDARs have been deployed in different positions on the mooring line. Lidar1 is the third to lowest module while lidar2 is the highest module. With this, also the height-dependency of the attenuation and backscattering length can be checked.

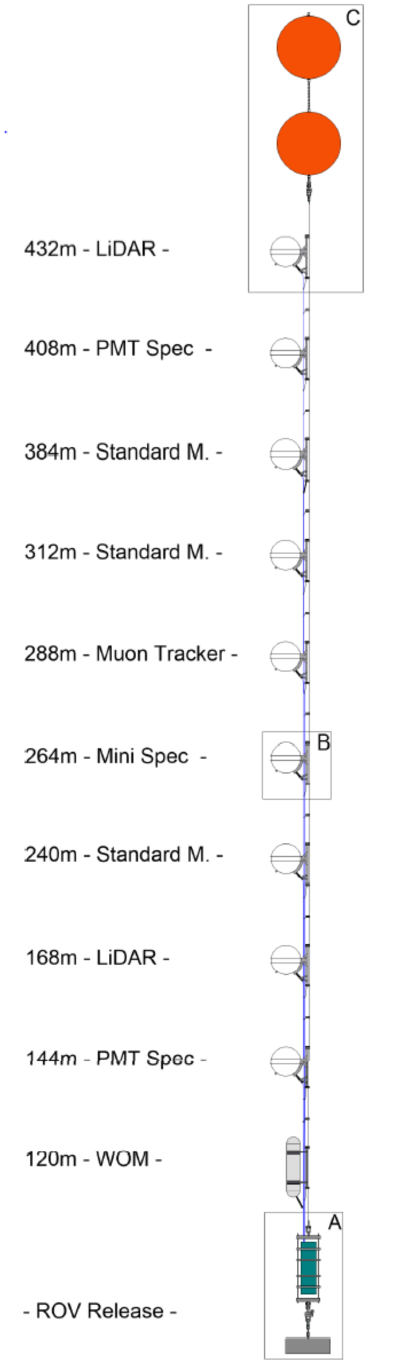

(a) Sketch of STRAW-b. Image courtesy of C. Spannfellner

(b) STRAW-b instrumented tray before loaded onto the deployment ship. Picture courtesy of ONC.

(c) Backdeck operations during deployment of the STRAW-b experiment. Picture courtesy of ONC.

(d) Submerging of one of the modules. Picture courtesy of ONC.

Figure 6.1: (a) Sketch of the STRAW-b experiment, (b) - (d) images of the deployment of STRAW-b.

6.1 INTRODUCTION

LiDAR is short for Light Detection And Ranging. Its functionality is similar to the RADAR system, with the difference that it uses light of the optical spectrum compared to radio waves. In general, a LiDAR consists of a pulsed light emitter (e. g. a laser) and a focusing optic with a light collecting device aligned with the light beam. This increases the collection efficiency of the backscattered light. The emitted photons are exposed to absorption and scattering processes. A portion of the light is backscattered to the LiDAR. The collected photons result in a rate $dN(t)/dt$. We can convert the rate to the number of detected photons per distance element $dN(r)/dr$ with $dr = c_w/2\,dt$ with c_w the speed of light in water when assuming that photons, on average, only scatter once, . Theoretically, this process is described in its most general form by the LiDAR equation:

$$\frac{dN(r)}{dr} = N_0 C G(r) \frac{A}{r^2} \beta(r) \exp\left(-2\int_0^r \alpha'(r)\,dr'\right) \tag{6.1.1}$$

The amount of detected light is dependent on the number of emitted photons N_0, an overall efficiency factor C, the overlap of the laser beam with the FoV of the PMT $G(r)$, the solid angle of the detector at the point of scattering A/r^2 and the backscattering coefficient $\beta(r)$. Most important, the photon rate is dominated by the attenuation defined by the distance-dependent exponential of the attenuation coefficient $\alpha(r)$. In this general case, the coefficients are assumed to be all distance-dependent to account for substantial changes of their values, e. g. when the medium changes. In our case, we assume that the physical properties of the seawater are constant in every direction. Hence the equation simplifies to:

$$\frac{dN(r)}{dr} = N_0 C G(r) \frac{A}{r^2} \beta \exp\left(-2\alpha r\right) \tag{6.1.2}$$

This equation has two dependencies of r and to further simplify, we introduce the so-called range-corrected-return:

$$S(r) = \frac{dN(r)}{dr} \cdot r^2 \tag{6.1.3}$$

In the LiDAR developed for STRAW-b, we decided on the THORLABS NPL45B as the emitter. A nanosecond pulsed laser emitting light with a wavelength of 450 nm. The focusing optics consists of a filter with a central wavelength of 450(10) nm to reduce potential background and a plano-convex 1" lens focusing the light on a μPMT (HAMAMATSU H12406) which operates in photon-counting mode. The system can be calibrated with a reference photodiode and a spectrometer. A reflective, partially transmitted foil prevents the photodiode from overexposure. It is aligned such that the reflected photons are directed to the spectrometer. A thin sheet of Teflon diffuses the light before the spectrometer to account for slight misalignments.

The emitter and receiver are mounted on a two-axis rotary stage to raster the upper hemisphere. The alignment of the laser and the receiver is of great importance. To adjust it, the laser mounting can be fine-tuned.The laser is fixed to the frame in one position, while two other points are, the laser was connected to small electrical motors via threaded cylindrical rods. The mounting points of the laser have an inner thread. The motors and their direction of rotation allow them to readjust the laser. Figure 6.2b shows a close-up image of the mounting of the laser. To prevent the rod from spinning, we attached two springs on each side of the laser mounting point.

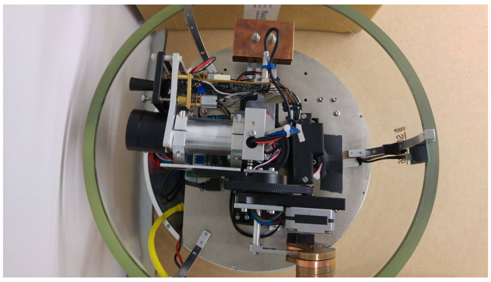

(a) Image of the assembled LiDAR.

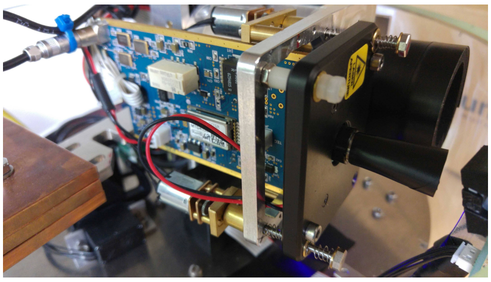

(b) Close-up image of the attachment of the laser to the focusing unit of the LiDAR.

Figure 6.2: Images of an assembled lidars in the 13" glass hemisphere.

6.2 LASER DIRECTION SCAN

The alignment of the FoV of the PMT can be ensured by performing a laser direction scan. good signal. To do this, we altered the direction of the laser and scanned different directions around the initial one. This scan can be performed in many different forms. We decided to move the laser in a discretized spiral around the initial direction. Each STEP is hereby defined as switching on the corresponding motor for 0.5 s. Mathematically, this can be described as three corners of a rectangle with length a and b in a three-dimensional cartesian space. The first corner, the fixed mounting point, is defined as the origin. The two adjacent corners with initial coordinates $[a, 0, 0]$ and $[0, b, 0]$ define the adjustable points. Where a is 51 mm and b is 38 mm.
A single step can be modeled as a linear displacement in the z-coordinate of the points. This linear displacement dz consists of the steepness of the thread, the RPM of the motor, and the time $\Delta t = 0.5\,\text{s}$ the motor is switched on. Except for Δt, some uncertainties need to be considered. In addition, we expect that the RPM of the motor differs from the nominal value in the short time frames. Hence we assumed an overall efficiency factor of 50 % on our estimates for the thread steepness and the RPM. This results in a linear displacement of $dz = 0.26\,\text{mm}$.
If we have m steps in a given direction, i. e. a motor is switched on m times, the resulting position of the corresponding mounting point is e. g. $[a, 0, m \cdot dz]$. This approximation holds as the total amount of steps is limited to 15 - 20 steps. The direction of the laser is calculated by computing the dot product of both vectors after the new step is calculated. The angles of the new direction are

retrieved by performing a coordinate transformation to spherical coordinates. After one step is performed, the LiDAR takes a short measurement of 2 s. If the laser direction is aligned with the FoV of the PMT, we expect a stronger signal than when it is not aligned. I. e. we expect a higher average number of detected photons per individual measurement.
As mentioned, we perform a discretized spiral starting from the initial laser direction and performing a step with either of the two motors. The maximum steps were 10 in each of the directions of the motors, resulting in 442 individual measurements. Although we measure in discrete directions, the result is interpolated to get a smooth contour plot.
The two plots of Figure 6.3 show the result of such a scan which the two LiDARs perform automatically once per day. The measurements were performed on the 15th of November, 2021. Both measurements show that the initial direction of the laser is not well aligned with the FoV. For the lower LiDAR (shown in Figure 6.3a) the region with the highest average number of detected photons is for a relative direction of $\theta \approx 2°$ and $\varphi \approx 135°$.

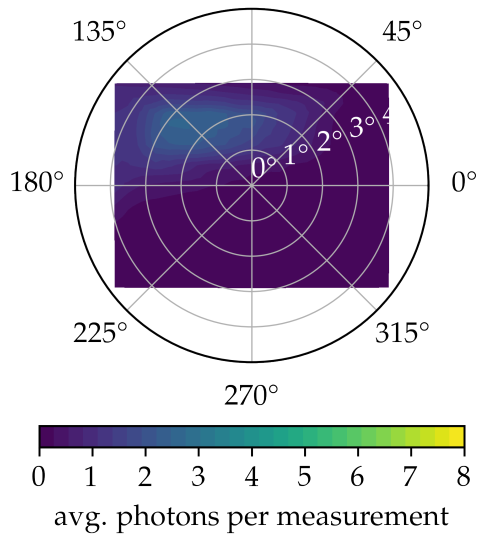

(a) Example of a scan of lidar1 (lower one) from the 15.11.2021. Maximum at 2.7 photons per measurement

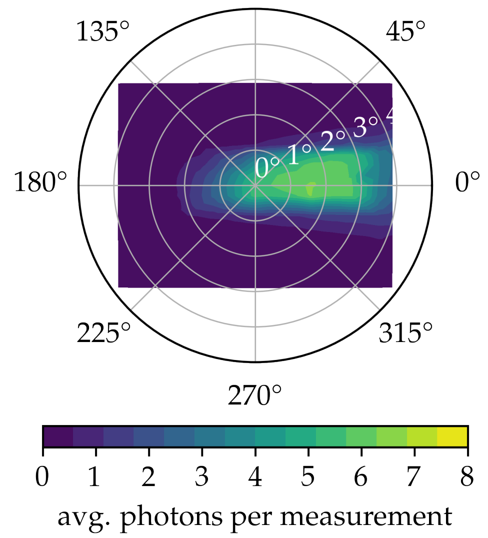

(b) Example of a scan of lidar2 (upper one) from the 15.11.2021. Maximum at 7.3 photons per measurement

Figure 6.3: Plots of the scan of lidar1 and lidar2. The angular coordinate is the azimuth and the radial coordinate is the inclination. The differences in the color scale are important to note, suggesting a significant difference in the light output of the two lasers although they are operating with the same settings.

The result for the upper LiDAR (Figure 6.3b) is similar. The initial direction returns an intermediate number of detected photons. This means that the laser either enters the FoV relatively late; hence, most photons have already been attenuated, and only a smaller fraction is scattered back. Or that the laser beam enters the FoV but leaves it at a finite distance, thus limiting the range in which the photons can scatter backward. This implies that some photons are always detected for increasing angles in this direction as the laser beam will always cross the FoV. For the first case, an increased angle would result in the

beam never crossing the FoV at one point. Thus reducing the detected photons to near zero as multiple scattering would be required to redirect a photon to the PMT, which is a suppressed process as the expected scattering length of the ambient water is significantly larger than the attenuation length (shown by the ANTARES collaboration[24]).
The result of Figure 6.3b indicates the first case for lidar2. The detected photons drop to zero for directions opposed to the region of high return ($\theta \approx 2°$ and $\varphi \approx 0°$) this effect is not visible at the other side. The directions above and below the high return region show a symmetric result. This suggests that increasing the laser direction to these regions corresponds to a shift of the laser direction to the left (or right) relative to the plane spanned by the optical axis of focusing optics and the laser axis. Such a shift corresponds to a case where the laser beam never enters the FoV of the PMT at some point.
However, due to the multitude of uncertainties, namely length and stability of a step dz, no absolute knowledge of the laser direction, and several possible steps for each electrical motor, one needs to be careful when interpreting the results of this task. E. g. measurements of the consecutive round are mapped to a wrong direction resulting in potentially unpredictable distortions of the result if the maximum possible motor steps are reached within the boundaries of the spiral. Additionally, this effect would lead to a shifted initial direction after the spiral was performed.

6.3 GEANT4 SIMULATION

During the development of the LiDAR, a Monte Carlo simulation based on a PDF derived from the LiDAR equation was performed. Deadtime and saturation of the PMT were accounted for with a simple noise model[70]. The result of this simulation is shown in Figure 6.4. The pile-up region in which the signal is dominated by saturation can be seen up to a distance of $\approx 30\,\text{m}$. Between the pile-up region and $\approx 100\,\text{m}$ the signal is dominated by the exponential dependency of the attenuation, after that by noise background.

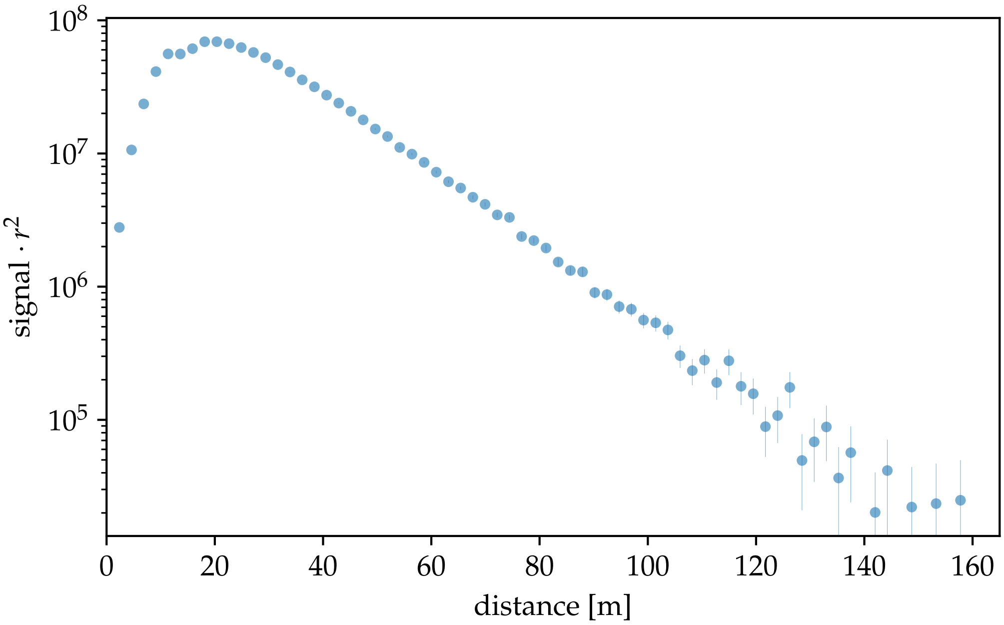

Figure 6.4: Result from the Monte Carlo simulation for the LiDAR , assuming an attenuation length of 26 m and a backscattering length of 90 m[70]. Errors result $\sqrt{N}$ uncertainties assuming a Poissonian distribution.

To further understand the data stream, a geant4 simulation for the LiDAR was developed in the scope of this thesis. The simulation of the gel pads was used as a baseline, where the geometry has been altered to resemble the LiDAR. In this simulation, the LiDAR is modeled with a cylinder with one open end and an inner diameter of 1 ". Similar to the PMT housing in the gel pad simulation, this cylinder is configured such that the photons terminate upon impact. The cylinder houses the 1 " plano-convex lens. We used BK7 as a material and a disk-like sensitive volume at the closed end of the cylinder.
The photons are injected from the surface of a small sphere in a give direction ($\theta = 6°$ and $\varphi = 0°$, direction taken from [70]) and with a small opening angle of 0.001°[70]. The center of the photocathode is located at $[0, 0, 50]$, the lens at $[0, 0, 110]$ and the laser at $[0, 44.5, 125.4]$. The values are in millimeters and relative to the center of the enclosing 13 " glass sphere and also taken from [70]. In addition to the changes in the geometry, we included attenuation and scattering processes alongside refraction. We chose the same attenuation and scattering length values as in the Monte-Carlo simulation. However, the working principle of the LiDAR is inherently very inefficient as the probability of backscattering is very low, and the signal is quickly attenuated. Consequently, the geant4 simulation is inefficient and was therefore not feasible to be computed on a PC. After several attempts to increase the efficiency, the only significant effect was to decrease the scattering length gradually to 20 m. Figure 6.5 shows the result of this simulation.

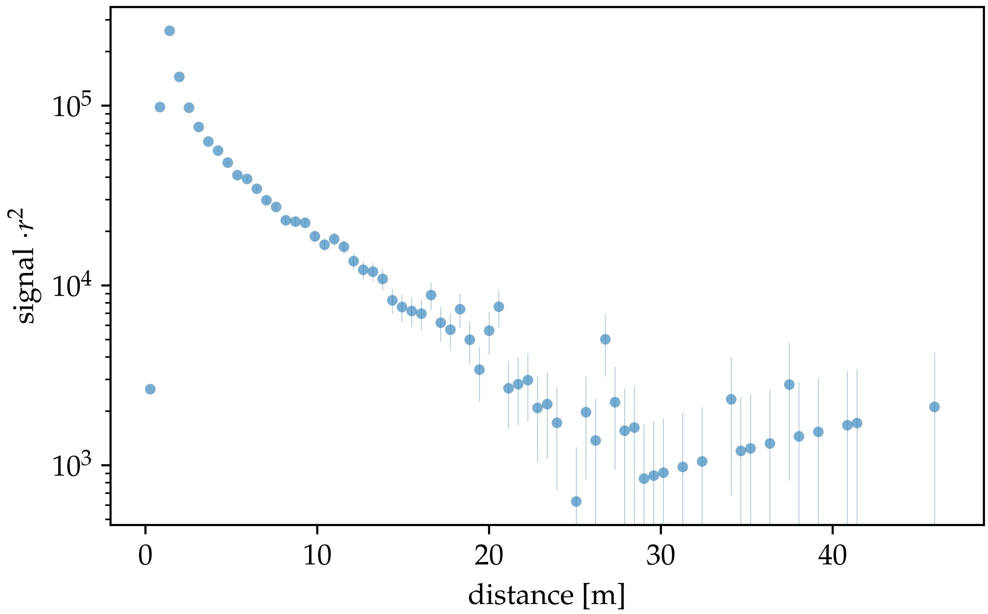

Figure 6.5: Result from the geant4 simulation with a reduced scattering length of 20 m. Bin width is 5 ns. Errors result $\sqrt{N}$ uncertainties assuming a poissonian distribution.

Compared to the result from the Monte-Carlo-Simulation, the geant4 simulation detected much less or no photons from longer distances (> 40 m), which was to be expected, because the scattering length was significantly reduced. Additionally, the pile-up for the shortest distances is not visible. In contrast, the signal exhibits a dominant peak in this region. This is because no limitations of the PMT, like saturation effects due to the pulse pair resolution, were included. These limitations would have reduced the number of photons even further. Nevertheless, the exponential dependency is visible. Also, noise models or effects like after pulses in the PMT are not included.
For a proper simulation of the LiDAR , the simulation needs to be computed on more performant hardware, like a cluster. Additionally, we need to include hardware effects, like the saturation, after pulsing, and noise of the hardware and simulate potential misalignments of the laser to improve our understanding of the system.

6.4 DATA

IN this section, the recorded signal of the deployed LiDARs will be considered. In a single measurement, the laser is switched on for 60 s and shoots light pulses with a nominal width of 5 ns with a rate of 10 kHz. The PMT is a photon-counting head. This means, that it outputs a 5 V signal for 10 ns (with a following deadtime of additional 10 ns[71]) every time a photon is recorded. As a result, no characterization regarding e. g. gain can be performed. A TDC (time-to-digital-converter) converts the photon's detection and the laser pulse's emission to a digital time saved in the data acquisition. A time-over-threshold

analysis measures the time between the rising edges of the trigger pulse from the emitted light pulse and the detected photons. The resulting time difference is the time-of-flight of the photons.
The LiDAR points in a fixed direction (elevation of 30° and azimuth of 60°). The individual measurements are performed once per day. Figure 6.6a shows the resulting signal of both LiDARs when the laser is well aligned with the FoV of the PMT. Some significant differences to the simulation are visible. The signal of the lower LiDAR (lidar1) has a peak at a distance of 100 m. After this peak, the signal declines exponentially until it is dominated by noise from distances longer than ≈ 180 m. The signal of the upper lidar (lidar2) is much stronger compared to the signal of lidar1, and the pile-up region is much longer (up to a distance of ≈ 100 m). Afterward, the signal decreases weaker. The signal does not reach the expected noise-dominated region below 400 m.

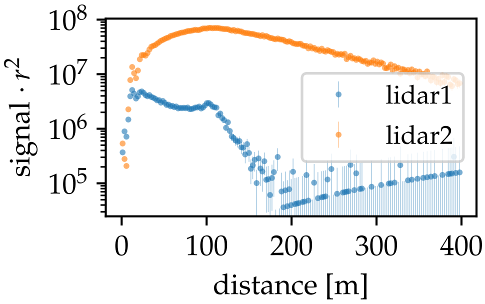

(a) Signal from single measurements of both LiDARs when the laser is well aligned.

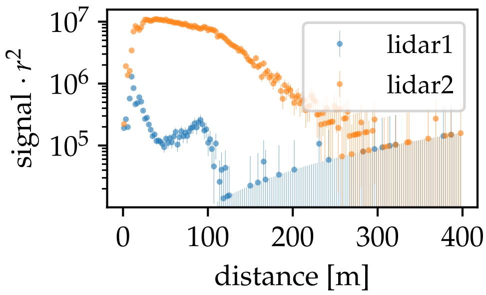

(b) Signal from single measurements of both LiDARs when the laser is not well aligned.

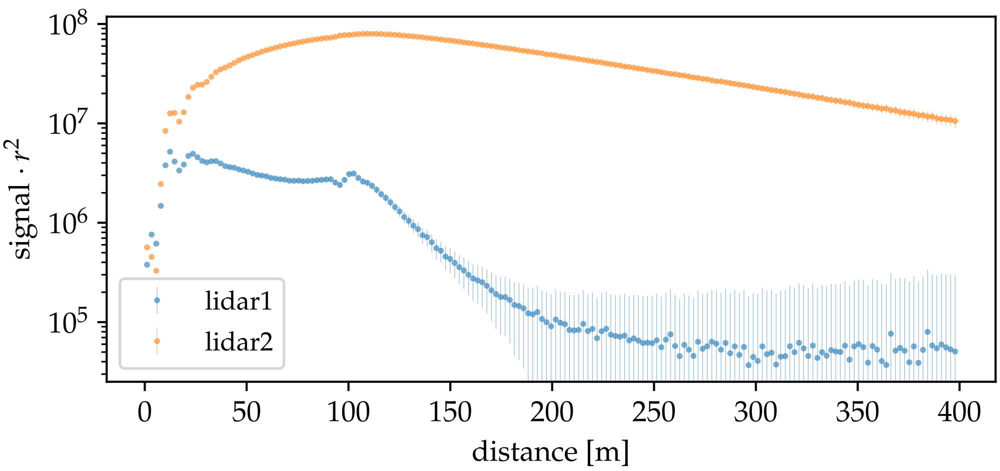

(c) Average over 200 individual measurements from both LiDARs.

Figure 6.6: Result of measurements from both LiDARs. (a) shows the result when the lasers are both in good alignment with the FoV, (b) shows in comparison the result when they are not well aligned, and (c) shows the result of an average of 200 individual measurements.

Figure 6.6b shows the result of individual measurements when the signal is not in good alignment with the FoV of the laser, i. e. the average number of detected photons per laser pulse is reduced, resulting in an overall weaker signal.

From the differences to the signal with a well-aligned laser (Figure 6.6a), one can draw qualitative conclusions. For once, the significant differences between the two kinds of signals show the importance of the laser alignment scan. In addition, the peak mentioned for the strong signal of lidar1 is still apparent, and compared to the overall signal, it is even more dominant. The signal's shape differs significantly from this feature, with a sharp decline before the peak. This indicates that the deviation compared to the simulation is caused by unknown systematics of the LiDAR and not by a physical property of the seawater.

The signal of the second LiDAR changed differently. Two slopes with different inclinations and a transition at about 100 m replace the very long pile-up region and flat slope. Since the slope of the signal is associated with the backscattering length and previous measurements suggest constant optical properties of seawater, it can be assumed that hardware effects cause this behavior.

Finally, we performed an average over 200 m individual measurements, which equals a time span of around 4 d. Figure 6.6c shows the result of this. Both signals are similar to the result of an individual measurement with a strong signal. This suggests that the characteristics that deviate from the simulation are constant in time and therefore strengthens the argument that the hardware of the LiDARs causes them.

Due to the peak in the signal of lidar1, we could not perform a proper fit for the attenuation length of the water because the peak is located in the middle of the fitting region. Additionally, the two divided regions are both not suitable for fitting. The peak quickly dominates the first one, and the second one is primarily noise-dominated.

6.5 Conclusion

In this chapter, we focused on the LiDAR, a specialized instrument developed for the second pathfinder mission of P-ONE. We presented advancements in the software development of the instrument, namely the laser direction scan. This scan adjusts the direction of the laser in a predefined pattern and performs short measurements after each step. The returned signal is a measure for the alignment of the laser with the FoV of the PMT relative to the initial direction of the laser. We plan to improve the laser direction scan by automatically adjusting the laser direction on a given condition, e. g. by pointing the laser in the direction of highest return to ensure a proper signal.

Additionally, we presented the first measurements of both LiDARs and showed that the signal is consistent over several measurements. However, the signal shows significant and time-independent deviations from the expected signal shape according to the simulation. Due to this, further studies and calibrations are ongoing or will be conducted soon with which we can finalize the measurements and retrieve a fit for the attenuation and backscattering length.

7 SUMMARY & OUTLOOK

In this work, we presented a geant4-based optimization study to find the best opening angle for a conical reflector. We compared the performance of a transparent reflector, i.e. a gel pad, to a solid one. We used a novel approach to assess the angular acceptance of the multi-PMT configuration, taking the importance of coincidence hits into account. The results of this simulation did not significantly favor one of the two types of reflectors over the other. Albeit the presented multi-PMT configuration is preliminary and subject to change, the transparent reflector performed on average 3 % better than the solid reflector. While the results are promising, further studies are needed to decrease the uncertainties of the simulation.

In the second phase of the thesis, we performed a feasibility study to produce gel pads. In this course, we investigated several optical gels. We found a combination to reliably produce standalone gel pads free of trapped air and successfully assembled it in the optical module. Furthermore, we performed first tests of a fully integrated production technique. In the upcoming weeks and months, tests of the integrated solution will be continued to solve the remaining issues. Depending on the final configuration, a single mooring line of P-ONE will host several hundred PMTs. Therefore, an important task will be to transfer the production of gel pads from small-scale trials to mass production.

In the third chapter, we presented a remotely controllable biaxial rotation stage developed for a calibration setup to test PMT candidates for the P-ONE neutrino telescope. With the rotation stage, two-dimensional scans of the photocathode can be performed to assess e.g. its uniformity. Apart from the characterization of the PMTs, the calibration station can be used to evaluate the produced gel pads. An important tool to cross-check the simulation results.

The final part of this thesis was centered around the LiDAR. We showed an algorithm to perform an automatized scan of the laser direction relative to the FoV of the LiDAR. This scan can be used to adjust the direction of the laser to ensure the desired signal strength. We concluded with the first data measured by the two LiDARs. While it looks promising, we encountered several significant deviations to the simulated signal shape which currently prevents an accurate analysis. Due to the restrictions of the Covid-19 pandemic, only limited characterization runs could be performed in air prior to the deployment. Hence, additional calibrations with a mirrored system have to be performed on-shore to better understand the occurring systematics. Ultimately, the optical properties of the seawater can be extracted from the signal and cross-checked with the data from STRAW, paving the way for the future neutrino telescope P-ONE.

BIBLIOGRAPHY

[1] B. P. Abbott et al. „Observation of Gravitational Waves from a Binary Black Hole Merger." In: *Physical Review Letters* 116.6 (2016). ISSN: 1079-7114. DOI: 10.1103/physrevlett.116.061102. URL: http://dx.doi.org/10.1103/PhysRevLett.116.061102.

[2] Victor F. Hess. „Über Beobachtungen der durchdringenden Strahlung bei sieben Freiballonfahrten." In: *Phys. Z.* 13 (1912), pp. 1084–1091.

[3] John Linsley. „Evidence for a Primary Cosmic-Ray Particle with Energy 10^{20} eV." In: *Phys. Rev. Lett.* 10 (4 Feb. 1963), pp. 146–148. DOI: 10.1103/PhysRevLett.10.146. URL: https://link.aps.org/doi/10.1103/PhysRevLett.10.146.

[4] Maurizio Spurio. *Particles and Astrophysics -A Multi-Messenger Approach*. Springer, 2015.

[5] Claus Grupen. *Astroparticle Physics*. Springer, 2020.

[6] Thomas K. Gaisser, Ralph Engel, and Elisa Resconi. *Cosmic Rays and Particle Physics*. 2nd ed. Cambridge University Press, 2016. DOI: 10.1017/CBO9781139192194.

[7] P. Abreu et al. „The exposure of the hybrid detector of the Pierre Auger Observatory." In: *Astroparticle Physics* 34.6 (Jan. 2011), pp. 368–381. ISSN: 0927-6505. DOI: 10.1016/j.astropartphys.2010.10.001. URL: http://dx.doi.org/10.1016/j.astropartphys.2010.10.001.

[8] Alessandro De Angelis and Mário Pimenta. *Introduction to Particle and Astroparticle Physics - Multimessenger Astronomy and its Particle Physics Foundations*. Springer, 2018.

[9] Tonia M. Venters et al. *Energetic Particles of Cosmic Accelerators I: Galactic Accelerators*. 2019. arXiv: 1903.04634 [astro-ph.HE].

[10] P. Padovani et al. „Active galactic nuclei: what's in a name?" In: *The Astronomy and Astrophysics Review* 25.1 (Aug. 2017). ISSN: 1432-0754. DOI: 10.1007/s00159-017-0102-9. URL: http://dx.doi.org/10.1007/s00159-017-0102-9.

[11] Paolo Padovani. „On the two main classes of active galactic nuclei." In: *Nature Astronomy* 1.8 (July 2017). ISSN: 2397-3366. DOI: 10.1038/s41550-017-0194. URL: http://dx.doi.org/10.1038/s41550-017-0194.

[12] *Offical website of the Fermi Gamma-ray Space Telescope*. URL: https://www.nasa.gov/content/goddard/fermi-spacecraft-and-instruments (visited on 01/31/2022).

[13] *Fermi LAT 10-year Source Catalog (4FGL-DR2)*. URL: https://fermi.gsfc.nasa.gov/ssc/data/access/lat/10yr_catalog/ (visited on 01/31/2022).

[14] *Offical website of the cherenkov telescope array*. URL: https://www.cta-observatory.org/ (visited on 01/31/2022).

[15] M. A. Markov. „On high energy neutrino physics." In: *10th International Conference on High Energy Physics*. 1960, pp. 578–581.

[16] „Evidence for High-Energy Extraterrestrial Neutrinos at the IceCube Detector." In: *Science* 342.6161 (Nov. 2013). ISSN: 1095-9203. DOI: 10.1126/science.1242856. URL: http://dx.doi.org/10.1126/science.1242856.

[17] Mark Aartsen et al. „Multimessenger observations of a flaring blazar coincident with high-energy neutrino IceCube-170922A." In: *Science* 361.6398 (July 2018). ISSN: 1095-9203. DOI: 10.1126/science.aat1378. URL: http://dx.doi.org/10.1126/science.aat1378.

[18] Tomoki Morokuma et al. „Follow-up observations for IceCube-170922A: Detection of rapid near-infrared variability and intensive monitoring of TXS 0506+056." In: *Publications of the Astronomical Society of Japan* 73.1 (Jan. 2021), pp. 25–43. ISSN: 2053-051X. DOI: 10.1093/pasj/psaa110. URL: http://dx.doi.org/10.1093/pasj/psaa110.

[19] Yoichiro Suzuki. „Super-Kamiokande Results on Neutrino Oscillations." In: *Physica Scripta* 2005 (Feb. 2006), p. 23. DOI: 10.1088/0031-8949/2005/T121/002.

[20] J. A. Formaggio and G. P. Zeller. „From eV to EeV: Neutrino cross sections across energy scales." In: *Reviews of Modern Physics* 84.3 (Sept. 2012), pp. 1307–1341. ISSN: 1539-0756. DOI: 10.1103/revmodphys.84.1307. URL: http://dx.doi.org/10.1103/RevModPhys.84.1307.

[21] I. Frank and Ig. Tamm. „Coherent Visible Radiation of Fast Electrons Passing Through Matter." In: *Selected Papers*. Ed. by Boris M. Bolotovskii, Victor Ya. Frenkel, and Rudolf Peierls. Berlin, Heidelberg: Springer Berlin Heidelberg, 1991, pp. 29–35. ISBN: 978-3-642-74626-0. DOI: 10.1007/978-3-642-74626-0_2. URL: https://doi.org/10.1007/978-3-642-74626-0_2.

[22] J.A. Aguilar et al. „Transmission of light in deep sea water at the site of the Antares neutrino telescope." In: *Astroparticle Physics* 23.1 (2005), pp. 131–155. ISSN: 0927-6505. DOI: https://doi.org/10.1016/j.astropartphys.2004.11.006. URL: https://www.sciencedirect.com/science/article/pii/S0927650504001902.

[23] M.G. Aartsen et al. „Measurement of South Pole ice transparency with the IceCube LED calibration system." In: *Nuclear Instruments and Methods in Physics Research Section A: Accelerators, Spectrometers, Detectors and Associated Equipment* 711 (May 2013), pp. 73–89. ISSN: 0168-9002. DOI: 10.1016/j.nima.2013.01.054. URL: http://dx.doi.org/10.1016/j.nima.2013.01.054.

[24] J.A. Aguilar et al. „Transmission of light in deep sea water at the site of the Antares neutrino telescope." In: *Astroparticle Physics* 23.1 (Feb. 2005), pp. 131–155. ISSN: 0927-6505. DOI: 10.1016/j.astropartphys.2004.11.006. URL: http://dx.doi.org/10.1016/j.astropartphys.2004.11.006.

[25] *IceCube-Masterclass. IceCube and Neutrinos*. URL: https://masterclass.icecube.wisc.edu/de/node/213 (visited on 02/02/2022).

[26] M. G. Aartsen et al. „All-sky Search for Time-integrated Neutrino Emission from Astrophysical Sources with 7 yr of IceCube Data." In: *The Astrophysical Journal* 835.2 (Jan. 2017), p. 151. DOI: 10.3847/1538-4357/835/2/151. URL: https://doi.org/10.3847/1538-4357/835/2/151.

[27] *Particle physics with ORCA*. URL: https://www.km3net.org/research/physics/particle-physics-with-orca/ (visited on 02/05/2022).

[28] M. G. Aartsen et al. „Development of a general analysis and unfolding scheme and its application to measure the energy spectrum of atmospheric neutrinos with IceCube." In: *The European Physical Journal C* 75.3 (Mar. 2015). ISSN: 1434-6052. DOI: 10.1140/epjc/s10052-015-3330-z. URL: http://dx.doi.org/10.1140/epjc/s10052-015-3330-z.

[29] A. Albert et al. „Measurement of the atmospheric neutrino and neutrino energy spectra with the ANTARES neutrino telescope." In: *Physics Letters B* 816 (May 2021), p. 136228. ISSN: 0370-2693. DOI: 10.1016/j.physletb.2021.136228. URL: http://dx.doi.org/10.1016/j.physletb.2021.136228.

[30] Dimitris Stavropoulos et al. „Atmospheric neutrinos from the first KM3NeT /ORCA data and prospects for measuring the atmospheric neutrino flux." In: *PoS* ICRC2021 (2021), p. 1125. DOI: 10.22323/1.395.1125.

[31] Lew Classen. „The mDOM – a multi-PMT digital optical module for the IceCube-Gen2 neutrino telescope." PhD thesis. Erlangen-Nürnberg: Friedrich-Alexander-University, Feb. 2017.

[32] C.G.S Costa. „The prompt lepton cookbook." In: *Astroparticle Physics* 16.2 (Nov. 2001), pp. 193–204. ISSN: 0927-6505. DOI: 10.1016/s0927-6505(01)00105-0. URL: http://dx.doi.org/10.1016/S0927-6505(01)00105-0.

[33] Dennis Soldin. „Atmospheric Muons Measured with IceCube." In: *EPJ Web of Conferences* 208 (2019). Ed. by B. Pattison et al., p. 08007. ISSN: 2100-014X. DOI: 10.1051/epjconf/201920808007. URL: http://dx.doi.org/10.1051/epjconf/201920808007.

[34] Paolo Fermani and Irene Palma. „Status and first results from the ARCA and ORCA lines of the KM3NeT experiment." In: *EPJ Web of Conferences* 209 (Jan. 2019), p. 01006. DOI: 10.1051/epjconf/201920901006.

[35] Nicolai Bailly et al. *Two-Year Optical Site Characterization for the Pacific Ocean Neutrino Experiment P-ONE in the Cascadia Basin*. 2021. arXiv: 2108.04961 [astro-ph.IM]. (Visited on 11/24/2021).

[36] M. I. Latz, T. M. Frank, and J. F. Case. „Spectral composition of bioluminescence of epipelagic organisms from the Sargasso Sea." In: *Marine Biology* 98.3 (June 1, 1988), pp. 441–446. ISSN: 1432-1793. DOI: 10.1007/BF00391120. URL: https://doi.org/10.1007/BF00391120.

[37] Stephan Meighen-Berger, Li Ruohan, and Golo Wimmer. *Bioluminescence modeling for deep sea experiments*. 2021. arXiv: 2103.03816 [q-bio.PE].

[38] Immacolata Carmen Rea et al. „P-ONE second pathfinder mission: STRAW-b.“ In: *PoS* ICRC2021 (2021), p. 1092. DOI: 10.22323/1.395.1092. (Visited on 11/24/2021).

[39] Christian Spannfellner. „Development of pathfi nder missions and instruments for the Pacifi c Ocean Neutrino Experiment.“ MA thesis. Technische Universität München, 2021.

[40] Albrecht Karle. „IceCube: Construction status and first results.“ In: *Nuclear Instruments and Methods in Physics Research Section A: Accelerators, Spectrometers, Detectors and Associated Equipment* 604.1-2 (June 2009), S46–S52. ISSN: 0168-9002. DOI: 10.1016/j.nima.2009.03.180. URL: http://dx.doi.org/10.1016/j.nima.2009.03.180.

[41] R. Abbasi et al. „IceTop: The surface component of IceCube.“ In: *Nuclear Instruments and Methods in Physics Research Section A: Accelerators, Spectrometers, Detectors and Associated Equipment* 700 (Feb. 2013), pp. 188–220. ISSN: 0168-9002. DOI: 10.1016/j.nima.2012.10.067. URL: http://dx.doi.org/10.1016/j.nima.2012.10.067.

[42] M. G. Aartsen et al. „First Observation of PeV-Energy Neutrinos with IceCube.“ In: *Physical Review Letters* 111.2 (July 2013). ISSN: 1079-7114. DOI: 10.1103/physrevlett.111.021103. URL: http://dx.doi.org/10.1103/PhysRevLett.111.021103.

[43] ANTARES Collaboration. *A Deep Sea Telescope for High Energy Neutrinos*. 1999. arXiv: astro-ph/9907432 [astro-ph].

[44] Mario Sedita and Rosanna Cocimano. „The NEMO project status.“ In: *Instrumentation ViewPoint, ISSN 1886-4864, N°. 8, 2009* (Jan. 2009).

[45] *Size comparison of the ARCA and ORCA detector*. URL: https://www.km3net.org/research/detector/km3net-arca-and-orca (visited on 02/05/2022).

[46] *Astroparticle physics with ARCA*. URL: https://www.km3net.org/research/physics/astronomy-with-arca/ (visited on 02/05/2022).

[47] Salvatore Viola et al. „Acoustic positioning system for KM3NeT.“ In: Aug. 2016, p. 1169. DOI: 10.22323/1.236.1169.

[48] Alexander Avrorin et al. „Baikal-GVD: first results and prospects.“ In: *EPJ Web of Conferences* 209 (Jan. 2019), p. 01015. DOI: 10.1051/epjconf/201920901015.

[49] *Geant4 website*. https://geant4.web.cern.ch/. (Visited on 11/16/2021).

[50] *VITROVEX® GLASS SPHERES Datasheet*. https://www.vitrovex.com/wp-content/uploads/2018/05/140101-VITROVEX-deep-sea-17-inch-spheres.pdf. (Visited on 11/16/2021).

[51] Lew Classen et al. „The mDOM - A multi-PMT digital optical module for the IceCube-Gen2 neutrino telescope.“ In: *PoS* ICRC2017 (2017), p. 1047. DOI: 10.22323/1.301.1047. (Visited on 11/16/2021).

[52] *Refractive Index borosilicate*. https://refractiveindex.info/?shelf=glass&book=SCHOTT-BK&page=N-BK7. (Visited on 11/16/2021).

[53] Eugene Hecht. *Optics, 4th Edition*. Pearson, 2002.

[54] *WACKER SilGel 612 Datasheet*. URL: https://www.wacker.com/h/de-de/medias/WACKER-SilGel-612-AB-en-2021.10.01-v2.pdf (visited on 12/14/2021).

[55] *Datasheet of the R14689 PMT by Hamamatsu*. https://www.hamamatsu.com/resources/pdf/etd/R14374_R14689_TPMH1381E.pdf. (Visited on 11/17/2021).

[56] E Leonora. „The Digital Optical Module of KM3NeT." In: *Journal of Physics: Conference Series* 1056 (July 2018), p. 012031. DOI: 10.1088/1742-6596/1056/1/012031. (Visited on 11/24/2021).

[57] Vedant Basu et al. „A next-generation optical sensor for IceCube-Gen2." In: *PoS* ICRC2021 (2021), p. 1062. DOI: 10.22323/1.395.1062. (Visited on 11/24/2021).

[58] *Report on the implementation of the online SN detection system of KM3NeT*. URL: https://www.km3net.org/wp-content/uploads/2020/02/D7.4-KM3NeT-online-physics-analysis.pdf (visited on 01/07/2022).

[59] *Optical Photon Processes in GEANT4*. URL: https://geant4.web.cern.ch/sites/default/files/geant4/collaboration/workshops/users2002/talks/lectures/OpticalPhoton.pdf (visited on 02/10/2022).

[60] *PILAS picosecond pulsed diode lasers - NKT Photonics*. LASERS & FIBERS. URL: https://www.nktphotonics.com/lasers-fibers/product/pilas-picosecond-pulsed-diode-lasers/ (visited on 11/24/2021).

[61] Daniel Suarez Garcıa. „Modeling of a multi-PMT optical sensor for IceCube-Gen2 in GEANT4 and Monte Carlo studies to optimize its sensitivity." MA thesis. Westfälische Wilhelms-Universität Münster, 2021.

[62] S.as Adrian-Martinez et al. „Expansion cone for the 3-inch PMTs of the KM3NeT optical modules." In: *Journal of Instrumentation* 8 (Jan. 2013).

[63] *Room-Temperature-Vulcanizing Silicone Rubber (RTV-1/RTV-2)*. URL: https://www.wacker.com/cms/en-de/products/product-groups/silicone-rubber/room-temperature-silicone-rubber.html (visited on 12/13/2021).

[64] *WACKER Elastosil RT 601 Datasheet*. URL: https://www.wacker.com/h/de-de/medias/ELASTOSIL-RT-601-AB-en-2020.07.01.pdf (visited on 12/14/2021).

[65] *PHOTOMULTIPLIER TUBES - Basics and Applications*. URL: https://www.hamamatsu.com/resources/pdf/etd/PMT_handbook_v3aE.pdf (visited on 01/11/2022).

[66] *Photomultiplier tubes basics*. URL: https://psec.uchicago.edu/library/photomultipliers/Photonis_PMT_basics.pdf (visited on 01/11/2022).

[67] *PIL040-FC Datasheet*. URL: https://contentnktphotonics.s3-eu-central-1.amazonaws.com/Datasheets/PILAS/ALS_Pilas_DX.pdf (visited on 01/11/2022).

[68] *PicoScope 6424E Datasheet*. URL: https://www.priggen.com/downloads/PicoScope%206000e%20Datenblatt.pdf (visited on 01/11/2022).

[69] *RSA1 by Kurokesu datasheet*. URL: https://psec.uchicago.edu/library/photomultipliers/Photonis_PMT_basics.pdf (visited on 01/12/2022).

[70] Christopher Fink. „Development of a LIDAR System for Characterizing the Optical Properties of Seawater at Cascadia Basin." BA thesis. Technische Universität München, 2019.

[71] *H12406 by Hamamatsu datasheet*. URL: https://www.hamamatsu.com/resources/pdf/etd/MicroPMT_TPMZ1019E.pdf (visited on 01/24/2022).